POLITECNICO
MILANO 1863

SCUOLA DI INGEGNERIA INDUSTRIALE
E DELL'INFORMAZIONE

An in-depth study of the photoluminescent properties of different variants of ultramarine blue pigment by time-resolved spectroscopy and micro-imaging

Tesi di Laurea Magistrale in
Physics Engineering - Ingegneria Fisica

Author: **Francesco Carta**

Student ID: 978281
Advisor: Prof. Daniela Comelli
Co-advisors: Dr. Alessia Di Benedetto
Academic Year: 2022-23

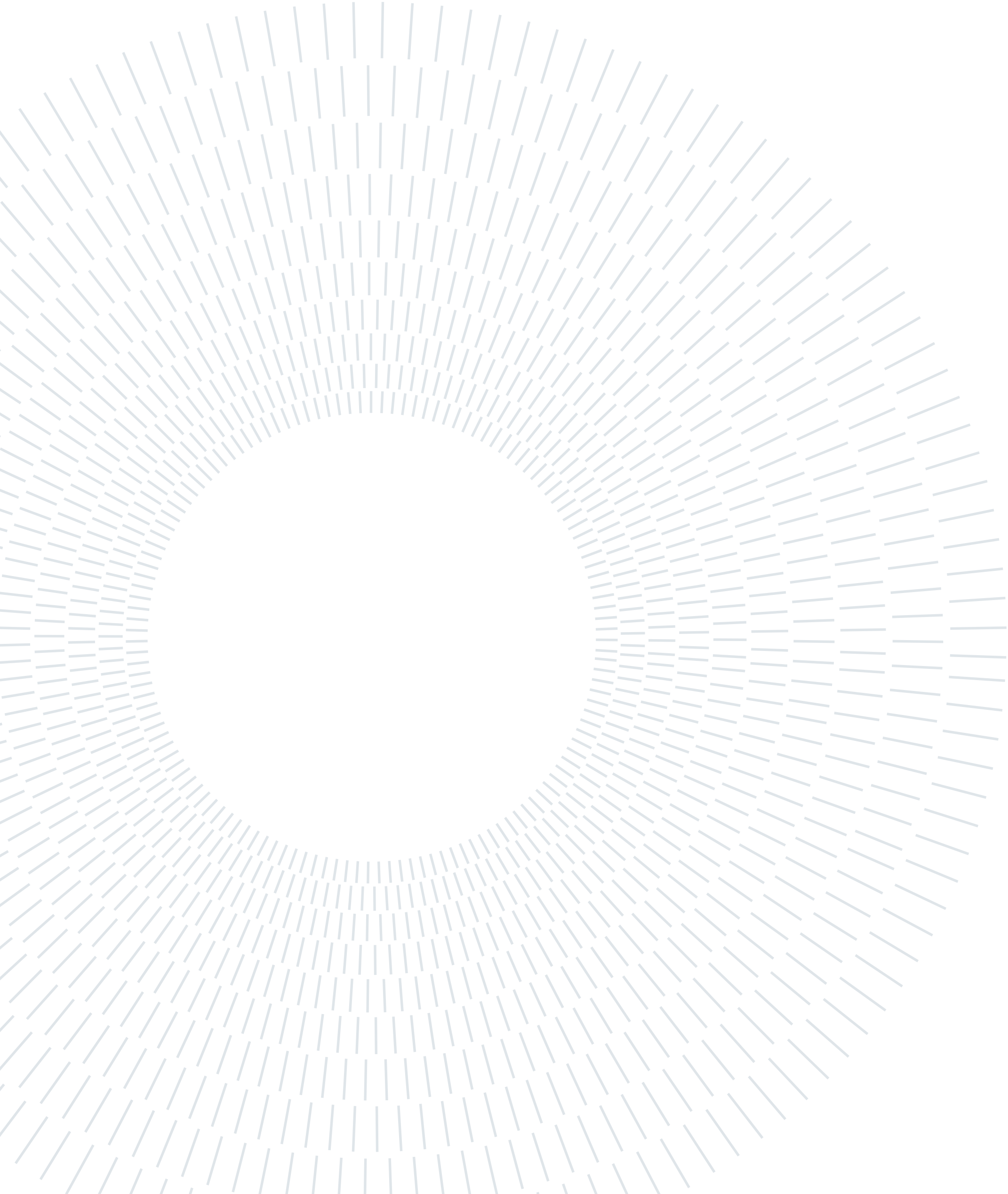

Abstract

Ultramarine blue is a blue pigment derived from lapis lazuli, a semi-precious stone that has been used as a decoration since the ancient Egyptians. This pigment entered European history from the port of Venice, in the 13th century, and immediately assumed great importance in medieval art due to its unparalleled and unusually stable bright color. Its geographical origin (probably the Badakshan region in present-day Afghanistan) and the laborious method of preparation meant that this pigment came at a price comparable to that of gold. Hence, it was a color that only appeared on the palettes of few renowned artists, and was dedicated to the most important figures in the religious iconography of the time: it could be found in the skies of religious scenes, or in the robes of Mary and Christ. The prohibitive price prompted artists to look for alternatives, so in 1828, the French Jean Baptiste Guimet discovered a method to produce artificial ultramarine blue at a tenth of the price of the natural one. His method is still used today.

In the field of art conservation, research on ultramarine blue revolves around three main questions: can we detect ultramarine blue on a painted surface? Is it possible to infer the geographical origin of the pigment without ruining the artifact under examination? And is it possible to distinguish the natural pigment (i.e. extracted in the traditional way) from the synthetic one? Researchers have used an arsenal of techniques (both destructive and not) and have managed to partially answer these questions. At the moment it is possible to consistently detect ultramarine blue, thanks to its characteristic Raman peak at 549 cm^{-1}, and to reliably distinguish between natural and synthetic ultramarine blue by looking at impurities still present in the pigment. The provenancing, however, is more problematic, given the variety of accessory minerals found in lapis lazuli from different regions.

This study is a part of a larger effort to determine whether ultramarine blue could be detected on a painting using photoluminescence spectroscopy. Here a full analysis of the photophysical characteristics of different variants of the pigment is presented.

We remark that there is little literature on the photoluminescence properties of ultramarine blue. Some studies have shown that, when exposed to ultraviolet light, this pigment does in fact emit a characteristic, but very faint fluorescence, which requires specialized equipment to be detected.

Indeed, the use of photoluminescence techniques to identify ultramarine blue is not as straightforward as with some other pigments characterized by a bright optical emission such as zinc white, titanium white and cadmium yellow and reds. Ultramarine blue's optical emission can be subtle and easily masked by other pigments or luminescent materials in a work of art, such as varnishes or binders.

Therefore, an in-depth research is needed to understand if and how photoluminescence can be employed to study one of, if not the most culturally relevant pigment of the last 1500 years.

Keywords: Ultramarine blue, pigment, lapis lazuli, photoluminescence, fluorescence, TRPL spectroscopy, FLIM, TG-HSI.

Abstract in lingua italiana

Il blu oltremare è un pigmento blu che deriva dalla lavorazione del lapislazzuli, una pietra semipreziosa che è stata usata come decorazione sin dagli antichi Egizi. Questo pigmento è entrato nella storia europea nel XIII secolo, dal porto di Venezia, e ha da subito assunto una grande importanza nell'arte medievale per via del suo colore acceso senza eguali e inusualmente stabile nel tempo. L'origine geografica (probabilmente la regione del Badakshan, nell'attuale Afghanistan) e il laborioso metodo di preparazione hanno fatto sí che questo pigmento assumesse un prezzo paragonabile a quello dell'oro. Perció è stato un colore che, sulle tavolozze di pochi illustri artisti, era dedicato alle figure piú importanti dell'iconografia religiosa del tempo e lo si ritrova nei cieli di scene religiose, o nei manti della Madonna o del Cristo. Il prezzo proibitivo ha spinto gli artisti alla ricerca di alternative, cosí, nel 1828, il francese Jean Baptiste Guimet scoprí un metodo per produrre il blu ultramarino artificiale a un decimo del prezzo di quello naturale. Il suo metodo è usato ancora oggi.

Nel campo della conservazione dell'arte, la ricerca sul blu oltremare ruota attorno a tre domande principali: è possibile individuare il blu oltremare su una superficie dipinta? È possibile dedurre l'origine geografica del pigmento senza rovinare il manufatto in esame? Ed è possibile distinguere il pigmento naturale (cioè estratto in modo tradizionale) da quello sintetico? I ricercatori hanno utilizzato un arsenale di tecniche (distruttive e non) e sono riusciti a rispondere parzialmente a queste domande. Al momento è possibile individuare il blu oltremare consistentemente, grazie al suo caratteristico picco Raman a 549 cm^{-1}, e distinguere con sufficiente affidabilitá il blu oltremare naturale da quello sintetico, osservando le impurità ancora presenti nel pigmento. L'attribuzione della provenienza, tuttavia, è più problematica, data la varietà di minerali accessori presenti nei lapislazzuli provenienti da diverse regioni.

Questo studio fa parte di uno sforzo più ampio per determinare se il blu oltremare possa essere rilevato su un dipinto utilizzando la spettroscopia di fotoluminescenza. Qui viene presentata un'analisi completa delle caratteristiche fotofisiche delle diverse varianti del pigmento.

Osserviamo che c'é poca letteratura sulle proprietà di fotoluminescenza del blu oltremare. Alcuni studi hanno dimostrato che questo pigmento, quando viene esposto alla luce ultravioletta, emette in effetti una fluorescenza caratteristica, ma molto debole e che richiede apparecchiature specializzate per essere rilevata.

In effetti, l'uso di tecniche di fotoluminescenza per identificare il blu oltremare non è così semplice come per altri pigmenti caratterizzati da un'emissione ottica intensa, come il bianco di zinco, il bianco di titanio e i gialli e rossi di cadmio. L'emissione ottica del blu oltremare può essere debole e facilmente offuscata da quella di altri pigmenti o materiali luminescenti presenti in un'opera d'arte, come vernici o leganti.

È quindi necessaria una ricerca approfondita per capire se e come la fotoluminescenza possa essere impiegata per studiare uno dei, se non il pigmento culturalmente più rilevante degli ultimi 1500 anni.

Parole chiave: Blu oltremare, pigmento, lapislazzuli, fotoluminescenza, fluorescenza, spettroscopia TRPL, FLIM, TG-HSI.

Contents

Abstract **i**

Abstract in lingua italiana **iii**

Contents **v**

1 Introduction **1**
1.1 Photoluminescence Theory 1
1.1.1 Introduction to photoluminescence 1
1.1.2 The Jablonski diagram 2
1.1.3 Meaningful rate equations 3
1.1.4 Photoluminescence in inorganic materials 4
1.2 The use of fluorescence spectroscopy and imaging in conservation science . 6

2 Overview of the Ultramarine Blue Pigment **9**
2.1 Lapis lazuli composition 9
2.2 Chemical structure of lazurite 10
2.3 Natural Ultramarine Blue 11
2.4 Artificial Ultramarine Blue 15
2.5 State of the art 17

3 Materials **21**
3.1 The samples 21

4 Methods **25**
4.1 Optical Microscopy 25
4.2 Time-Resolved Photoluminescence (TRPL) Spectroscopy 27
4.2.1 TRPL Setup 27
4.2.2 Measurement protocol 27
4.3 Fluorescence Lifetime Imaging (FLIM) 31

4.3.1 FLIM Setup 31
4.3.2 Measurement protocol 31
4.4 Time Gated Hyperspectral Imaging (TG-HSI) 35
4.4.1 TG-HSI Setup 35
4.4.2 Measurement protocol 35

5 Results **39**
5.1 Optical Microscopy 39
5.2 TRPL Spectroscopy 43
5.2.1 Nanoseconds emission 43
5.2.2 Microseconds emission 48
5.2.3 Tens of microseconds emission 53
5.3 Time-Gated methods: TG-HSI and FLIM 58
5.3.1 UB2 61
5.3.2 UB5 65
5.3.3 UB7 69

6 Discussion **73**

7 Conclusions and Future Developments **75**

Bibliography **77**

List of Figures **81**

List of Tables **85**

Acknowledgements **87**

1 | Introduction

1.1. Photoluminescence Theory

1.1.1. Introduction to photoluminescence

Photoluminescence [1], abbreviated with PL, is the emission of light from a substance as a result of absorption of electromagnetic radiation. In particular, the atoms or molecules can absorb energy and get in an excited state and then emit photons as they relax to the ground state. Depending on the nature of excited states, PL is called *fluorescence* or *phosphorescence*.

The emission process takes the name fluorescence if the excited state is a singlet state: the electron in the excited orbital is paired with the electron in the ground state, meaning they have opposite spin. In this case, the relaxation is a spin allowed transition and the average lifetime for fluorescence, i.e. the average time a molecule stays in the excited state, is in the order of $10^{-8}s$. Phosphorescence, on the other hand, is the emission from a triplet state, in which the electron has the same spin orientation of the one in the ground state (as shown in figure 1.1). The transitions back to the fundamental state are forbidden, the emission probability is therefore much lower and the lifetimes are in the range from milliseconds to seconds.

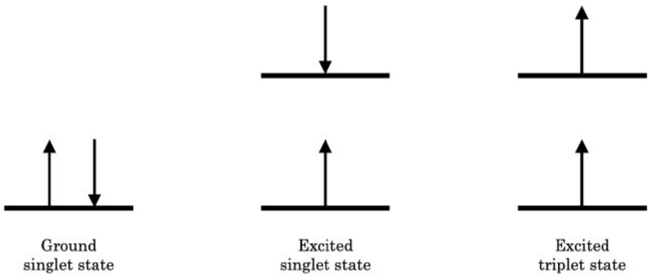

Figure 1.1: Difference between the excited singlet and excited triplet states.

1.1.2. The Jablonski diagram

Transitions between the ground and excited states in molecules are well summarized with Jablonski diagrams (figure 1.2). Molecules also possess vibrational states which increase the number of transitions that can take place during excitation or relaxation phenomena.

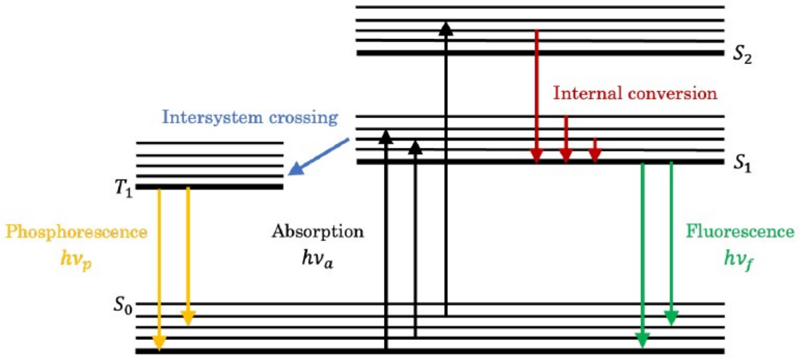

Figure 1.2: Example of Jablonski diagram. S0, S1 and S2 levels are respectively the electronic fundamental state, the first excited state and the second excited state, while T1 represent the first excited triplet state. For each of these states, the vibrational states are added.

In the figure, the S0, S1 and S2 levels are respectively the electronic fundamental state, the first excited state and the second excited state, while T1 represent the first excited triplet state.

Absorption implies a transition of an electron from ground to an excited vibronic state. These transitions are very fast and typically occur in times of the order of $10^{-15}s$. Usually **internal conversion** follows, which is a non-radiative, thermal relaxation process in which the electron relaxes to the lowest vibrational level of the excited state. The order of magnitude of the duration of this process is of $10^{-12}s$. It is several orders of magnitude faster than fluorescence and for this reason it is possible to assume that all the electrons undergo this process before fluorescence occurs. Finally we have **radiative relaxation** of the electron, i.e. the emission of a photon and the transition from the excited state to the ground state, which constitutes fluorescence (with a lifetime of about $10^{-8}s$). Excited electrons can also undergo **inter-system crossing**, which is relaxation into the triplet state. In this case relaxation to the ground state is forbidden by selection rules on the spin, thus the emission rate is lower and the lifetime is longer (as mentioned before, of around $10^{-3} - 1s$) and we get phosphorescence.

Notably, since absorption can occur from the ground state to any vibrational excited state, and emission from the excited state to any vibrational ground state, the absorption and emission spectra of a substance are generally mirrored. Moreover, due to the internal conversion of the excited state, emission typically occurs at lower energies, that is to say higher wavelengths, with respect to absorption: this shift between the two spectra is called **Stokes shift**.

1.1.3. Meaningful rate equations

Relaxation can occur as both radiative and non-radiative transition, meaning with or without photon emission.

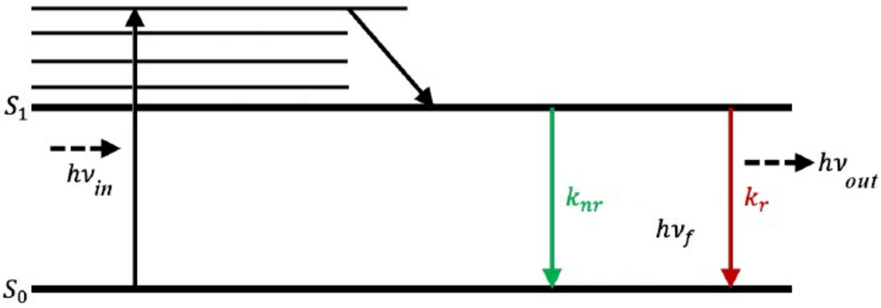

Figure 1.3: Jablonski diagram of a relaxation process that can occur as both a non-radiative (in green) and radiative (in red) transition.

These processes are characterized by a probability of decay per unit time, which is represented in terms of recombination rate k measured in s^{-1}. The total recombination rate is calculated as the sum of the recombination rates of both radiative (k_R) and non-radiative (k_{NR}) processes:

$$k = k_{NR} + k_R \tag{1.1}$$

The inverse of the recombination rate gives the recombination lifetime,which is the average time that the molecule spends in the excited state, before the relaxing into the fundamental state:

$$\tau = \frac{1}{k} = \frac{1}{k_{NR} + k_R} \tag{1.2}$$

Notably the presence of non-radiative relaxation paths shortens the fluorescence lifetime. In case of non-radiative decay negligible with respect to the radiative one, the lifetime of the molecule is called intrinsic.

Another important quantity that provides information about the optical emission is the quantum efficiency, also called quantum yield. It is given by the ratio between the radiative recombination rate and the total recombination rate.

$$\Phi = \frac{k_R}{k_{NR} + k_R} \tag{1.3}$$

A quantum yield equaling 100% means that the only de-excitation path followed by the molecule is the radiative one.

It is now possible to retrieve the rate equation that describes the de-population of the excited state and, starting from there, the intensity of the fluorescence signal as a function of time. Let's first consider a two-level system as in figure 1.3. Since absorption process is way faster than fluorescence, it is possible to consider that the population of the excited level occurs instantaneously. The rate equation describes the variation in time of the population N_1, which is the population in the excited level. Considering first-order kinetics:

$$\frac{dN_1(t)}{dt} = -(k_{NR} + k_R)N_1(t) \tag{1.4}$$

By integrating we observe that the population follows an exponential decay, with fluorescence lifetime as decay constant:

$$N_1(t) = N_1(t_0)e^{-\frac{t}{\tau}} \tag{1.5}$$

The fluorescence intensity is directly proportional to the population of the excited state N_1:

$$I(t) = I(t_0)e^{-\frac{t}{\tau}} \tag{1.6}$$

1.1.4. Photoluminescence in inorganic materials

Semiconductors are materials with core electrons, located in the atomic orbitals, and valence electrons, delocalized in molecular orbitals. The molecular orbitals form two separate bands: the valence band (VB), that is the highest band in which the electrons are normally present at $0K$,and the conduction band (CB), which is the next lowest empty band. The difference in energy between these two bands is called energy gap E_g, which depends on lattice spacing, temperature and pressure and it basically defines the properties of the material. In a perfect crystal lattice there are no energy levels within the band gap, but imperfections in the lattice introduce new states within the gap that electrons can occupy. An imperfection is:

- a vacancy, when an atom is missing in the appropriate lattice site;
- interstitial, if an intrinsic or foreign atom in between lattice sites (in the first case

it is called "self-interstitial");

- substitutional, where a foreign atom substitutes one of the host atoms;
- an antisite defect (for compounds only) where host atom B occupied a site that should have been for host atom A.

These defects can produce new localized energy states within the energy gap. These states are called "traps", since they are able to capture the de-exciting electrons. It is possible to distinguish these traps into ‘shallow’ or ‘deep’ based on their position within the band gap: shallow traps refer to levels close to the valence and conduction band edges, whereas deep traps refer to levels deep within the energy gap*.

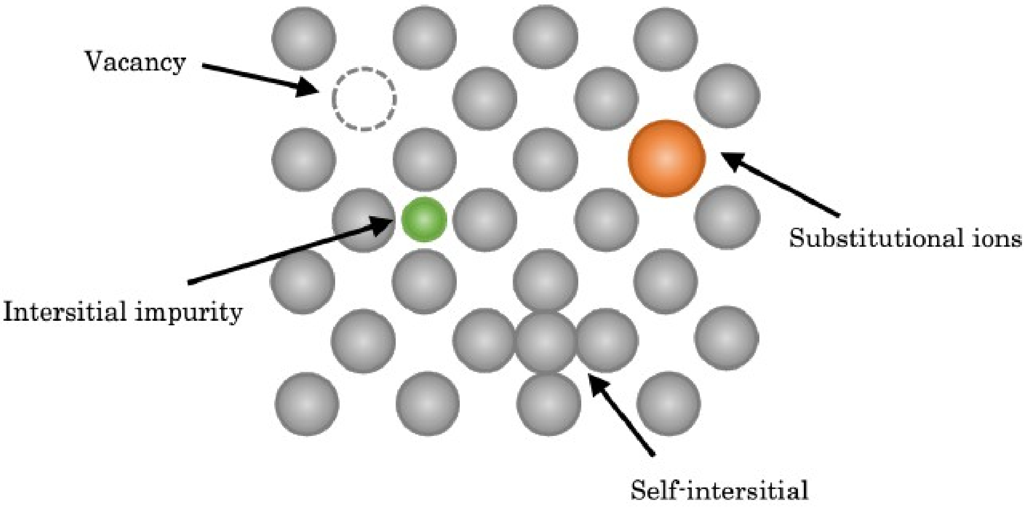

Figure 1.4: Examples of defects in the structure of a semiconductor.

Once trapped in shallow levels just below the conduction band, electrons can easily be thermally excited into it. Deep traps, instead, create energy levels within the band gap far from the conduction or valence bands. In this type of defects, the energy required to remove an electron or a hole from the trap is much larger than the thermal energy $k_B T$ and they behave as recombination centres for charges.

There are two ways in which semiconductor can exhibit photoluminescence: intrinsic luminescence, which would be typical of a perfect semiconductor, with a crystalline structure void of imperfections, and extrinsic luminescence, which is due to the presence of

---

[*] Although this was the way in which the distinction between deep traps and shallow traps was first formulated, nowadays a more correct distinction involves the use of Effective Mass Theory, whose presentation is outside the scope of this work.

defects or impurities. The intrinsic luminescence refers to the emission resulting from the recombination of an excited electron in the conduction band with a hole in the valence band. On the other hand, the extrinsic luminescence is the emission derived from the recombination from or to a trap state.

1.2. The use of fluorescence spectroscopy and imaging in conservation science

Most pigments used from antiquity to relatively modern times have been inorganic compounds, either naturally occurring as colored minerals or carefully synthesized.

In the field of art conservation and analysis, it is necessary to develop non-invasive techniques to examine artworks and gain valuable insights into their composition, condition, and authenticity, while preserving their integrity. As a result, the excitation of fluorescence has emerged as a non-destructive method to analyze painted surfaces and has been used by conservators and researchers alike since the 1920s, when UV lamps were invented.

Fluorescence has proved to be a very useful phenomenon, because by looking at a painting under UV light, one can instantly discover signs of manipulation. Usually, an old, well conserved painting, exhibits a greenish glow when exposed to UV light and any dark spots constitute most probably signs of retouching (as in figure 1.5). The reasons for this phenomenon have been discovered by E. René de la Rie, who conducted the first quantitative studies on the fluorescence of pictorial materials in the 1980s [2–4]. He discovered that the source of fluorescence was the varnish used to protect the painted layer, rather than the pigments themselves (though some do fluoresce [2]). Typically either linseed oil or natural resins have been used as varnish and, when freshly applied, they appear transparent and do not exhibit any fluorescence. However, as time passes and they degrade, they visibly yellow (a phenomenon called "discoloration"), which is directly linked to their development of fluorescence [3]. Furthermore he discovered that not all pigments fluoresce, but they do impact the fluorescence properties of the linseed oil when used as binder, either accelerating the degradation, slowing it down or not affecting it at all [4].

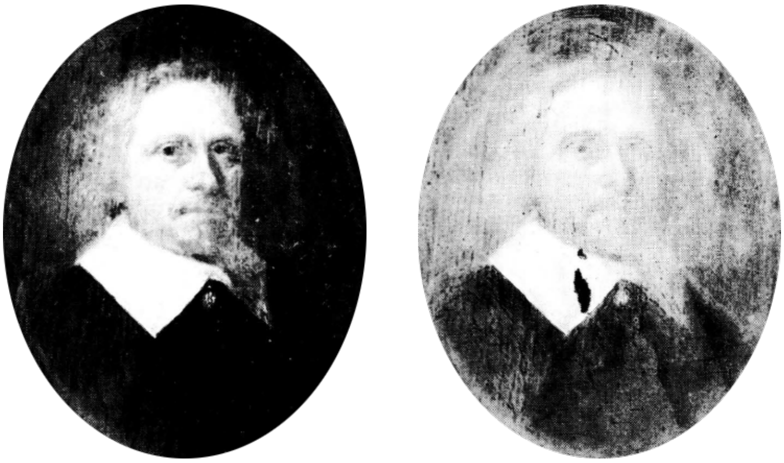

(a) (b)

Figure 1.5: Section of the Portrait of Casper Barlaeus. Probably 17th century. Oil paint on panel. Oil painting in normal light (a) and in ultraviolet light (b) (Adapted from [3]). The strong fluorescence of the varnish layer is clearly visible. In the robe area the portrait was seemingly cleaned, resulting in a less strong, though still present, emission. The strong fluorescence of lead white oil paint (present in the collar, hair and face) appears through the varnish layer. The dark spots in the collar are unmistakable signs of retouching. They are evidently visible under UV light because they were either not covered with a varnish or because they were covered with newer and therefore less degraded and fluorescent varnish. Notably, the technique of identifying retouching by the different fluorescent areas in a painting doesn't work when the retouching is very old: the fluorescence of the varnish applied may not stand out with respect to the rest of the painting, so other methods are required for its identification.

A critical limitation of the study of the emission spectra of pigments in paintings is that using a UV lamp as the excitation source and a steady-state spectrometer, it is impossible to separate the emission of inorganic pigments from the much more intense emission of the varnish or the binder. Therefore the resulting spectra are combinations of all.

A natural evolution of the analysis with steady state UV lamps are time-gated methods that use laser sources, like Time-Resolved Photoluminescence (TRPL) spectroscopy and Fluorescence Lifetime Imaging (FLIM), which have both been employed in this work and are described in detail in chapter 4. These methods use a pulsed laser source and a time-gated detector to distinguish luminescent materials based on their emission lifetimes, which, depending on the emitter and on the emission decay path, can vary from picoseconds to milliseconds. Luckily, organic materials, like organic pigments, varnishes and binding media have fluorescent lifetimes in the order of 1 to 10 ns, whereas inorganic pigments can be characterized by fluorescent lifetimes in the order of the microseconds [5]. A typical setup for these techniques consists of (1) a pulsed laser source, (2) suitable optics for the delivery of the laser radiation to the sample, (3) a system of lenses for the collection of emitted photons, (4) a time resolved detector (usually a time-gated intensified camera [6]) coupled with a spectrometer, a microscope or a camera lens. The time gated approach involves sending a laser pulse to the sample, which excites the fluorescent response, then waiting a set amount of time, depending on the specific decay kinetics of the sample, and finally opening a gate, allowing the emitted photons to be captured by the detector (either a spectrometer or a CCD camera). As shown in figure 1.6 the method allows the separation between the emission of nanosecond lifetime emitters (such as binders, colorants and varnishes) and that of micro- and millisecond lifetime emitters, which could be the defect-related emission ascribable to inorganic and semiconductor-based pigments and is typically at least one order of magnitude lower in intensity than the first one.

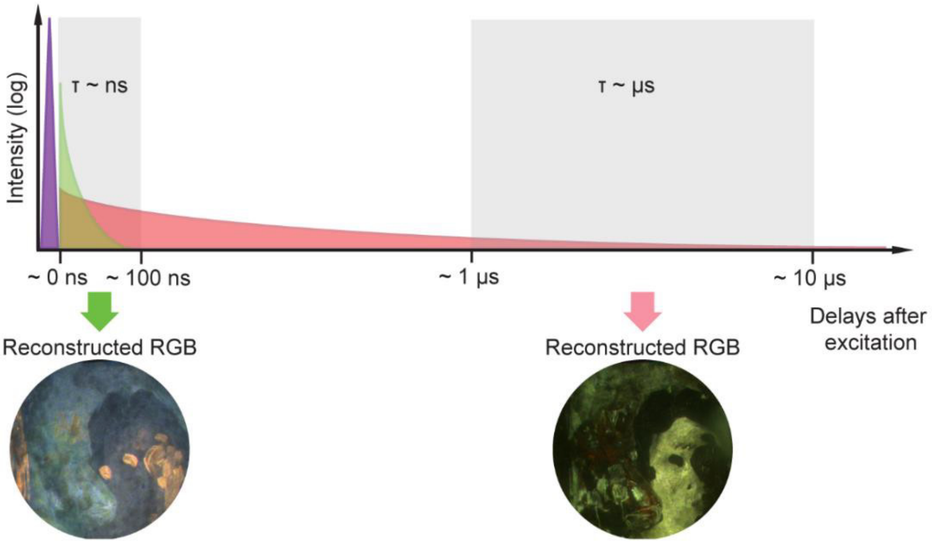

Figure 1.6: Example of time gated imaging. The two pictures are colorized according to the detected spectra. Notice how the fluorescent emission changes with time. Taken from [7].

2 | Overview of the Ultramarine Blue Pigment

2.1. Lapis lazuli composition

Ultramarine blue is the pigment extracted from the lapis lazuli stone. Lapis lazuli is a complex mineral which owes its distinctive blue color to one of its main components: lazurite. Lazurite is far from being the only component: traces of many impurities and accessory phases have been found when studying lapis lazuli: haüyne, sodalite*, diopside, dolomite, wollastonite, calcite, pyrite, sanidine, albite, apatite, nepheline phlogopite [8–11].

The greater the fraction of lazurite with respect to other minerals, the greater the quality of the lapis lazuli and the deeper its color. remarkably, the most appreciated lapis lazuli stones present visible pyrite inclusions.

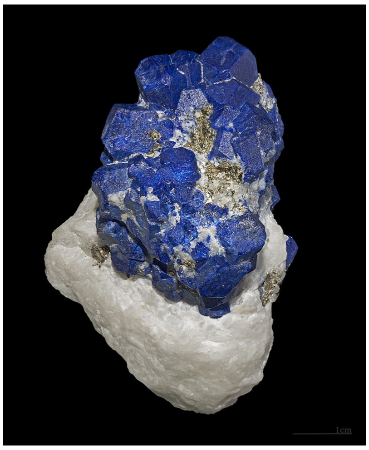

Figure 2.1: Lapis lazuli stone with pyrite inclusion in calcite matrix. Taken from Wikipedia.

---

*Both haüyne and sodalite, which belong to the same mineral group as lazurite, can also occur in a blue form, as well as a variety of other colors [8].

2.2. Chemical structure of lazurite

Lazurite is the main responsible for the distinctive blue color of the lapis lazuli mineral. It is an aluminosilicate, tectosilicate mineral belonging to the sodalite group. It contains sulfate, sulphur and chloride and its general chemical formula is $(Na, Ca)_8[(S, Cl, SO_4, OH)_2 (AlSiO_4)_6]$.

All silicates have as basic structural unit the SiO_4 tetrahedron, which consists of a silicon ion in the middle and an oxygen ion at each apex. In aluminosilicates, aluminum ions substitute some silicon ions, forming the AlO_4 tetrahedra. In tectosilicates (framework silicates) each oxygen ion is shared between two tetrahedra, linking all the tetrahedra together to form a framework. In lazurite the Al and Si in the tetrahedral framework are fully ordered and form the sodalite cages [12].

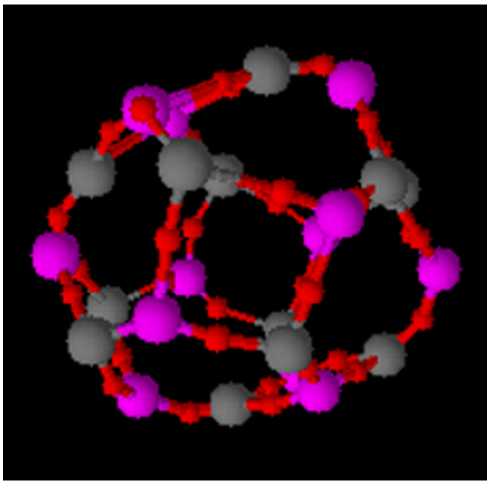

Figure 2.2: A single sodalite cage. Aluminum (pink) and silicon (grey) atoms are linked by shared oxygen atoms (red). This forms a framework around cavities capable of housing ions and small molecules. Taken from [12].

This framework is colorless and is capable of encapsulating small ions and molecules, which can act as color centers. The lazurite chromophores are polysulfide radicals S_3^- (blue) and S_2^- (yellow), which are inserted in the sodalite cages in the form of NaS_3 and NaS_2 salts. The hue of the pigment extracted from the mineral is related to the relative, rather than absolute, concentration of these chromophores [13]. Although the polysulfide radicals are very unstable, the sodalite cage structure protects them from external agents, which explains the great durability of the ultramarine pigment[†].

[†] During the years some occurrences of discoloration have been noted: some once vibrant areas on painted surfaces have become grayish or yellowish. This phenomenon is known as "ultramarine sickness".

2.3. Natural Ultramarine Blue

Lapis lazuli has been used as a semi-precious stone and decorative building stone by the Egyptians, the Greeks and the Romans [8]. In fact, the mineral is described in ancient manuscripts as *De Lapidibus* by Theophrastus (4th century BC) and *Naturalis Historia* by Pliny the Elder (1st century AD). However, so far, no evidence of these people using lapis lazuli as pigment has surfaced. The dominant blue pigment of those times was actually Egyptian blue, a synthetic copper silicate pigment whose method of production was lost in late Roman times. A method to produce Egyptian Blue was fully recovered only in the 19th century following efforts of Chaptal [15] and Davy [16].

The earliest occurrence of lapis lazuli being used as a pigment was in 6th and 7th century AD wall-paintings in the cave temples at Bamiyan, Afghanistan (figure 2.3). Bamiyan, located approximately 530 km southwest of Badakshan, Afghanistan, is renowned for being the region where the lapis lazuli was firstly mined. The mines are notably documented in Marco Polo's travelogue, the "Million" [17].

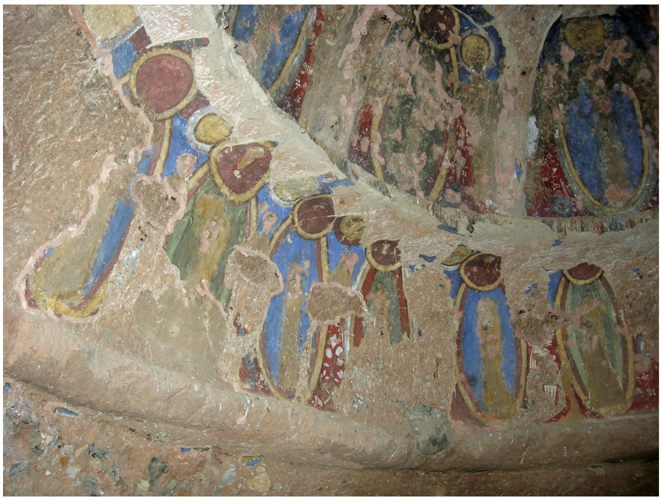

Figure 2.3: Wall paintings in the cave temples of Bamiyan, Afghanistan, ca. 507-554 AD. Artist unknown. Wikimedia Commons.

It was also found in Persian miniatures of the 13th or 14th century, in Chinese paintings of the 10th or 11th century and Indian mural paintings of the 11th, 12th and 17th centuries [8], indicating that the trade of the pigment flourished in central Asia. It was so important in fact that a "lapis lazuli road" could be hypothesized [17]. In the Middle Ages it came to Europe through the harbor of Venice and it was mainly employed in Italy between

---

Although the name suggests that the pigment might not be that durable after all, the discoloration can be primarily attributed to the degradation of the binding medium rather than the pigment itself [14].

the 14th and 16th centuries and used extensively in miniatures, frescoes and in tempera and oil paintings. There it took the name *ultramarine blue*, meaning “from overseas”, to distinguish it from another variety of blue pigment, azurite coming from Germany, which was also known as *citramarine blue* meaning “on this side of the sea” [17].

This pigment was extremely difficult to procure because of its geographical origin and of the laborious method of extraction, which reflected on its price, comparable to that of gold. Just like gold leaf, ultramarine blue was provided to the painter by the patron who commissioned the artwork, who was usually repaid by showing off their wealth through the artwork (just look at the splendid *Cappella degli Scrovegni* decorated by Giotto, shown in figure 2.4). Of course, the fame of the painter also played a role in accessing the pigment: only recognized masters were granted the use of the pigment, whereas less famous painters would settle for the much cheaper azurite [8].

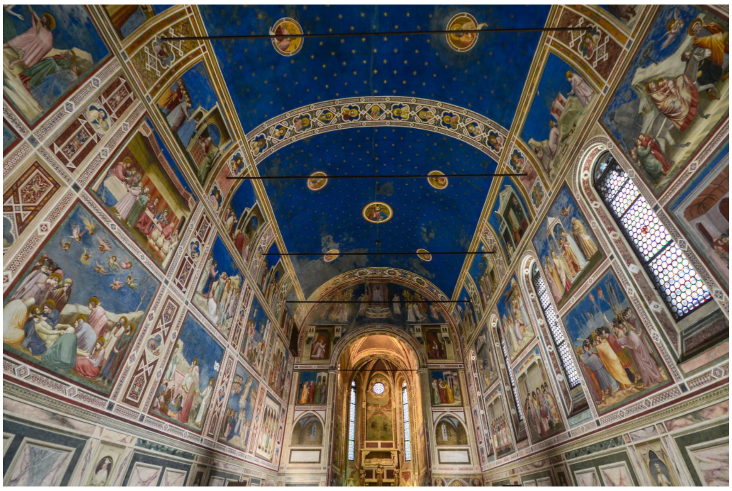

Figure 2.4: Vault of the Cappella degli Scrovegni, Padua, Italy. Frescos by Giotto, ca. 1305 AD. Author: Luca Argalia , Source: Flickr, License: CC BY NC SA 2.0.

Because of its high cost, the pigment was used as a solid layer of color only in religious contexts (figure 2.5) and only on the most significant iconographic subjects, such as for the robes of Christ and the Virgin (figure 2.6). Elsewhere it was generally mixed with or thinly glazed over an azurite foundation [8]. It was also usually mixed with white lead to get a lighter color, or with a red lake to obtain a purple [8].

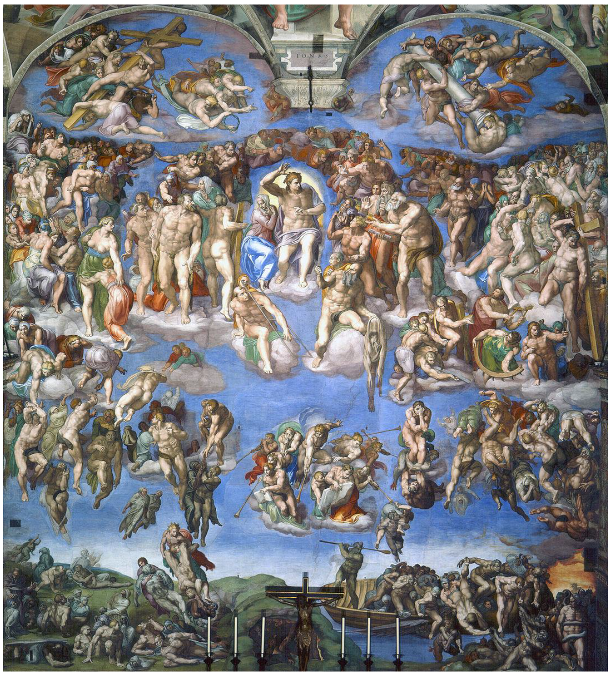

Figure 2.5: Michelangelo, The Last judgement. Sistine Chapel, the Vatican. 1536-1541. Fresco. Wikimedia commons.

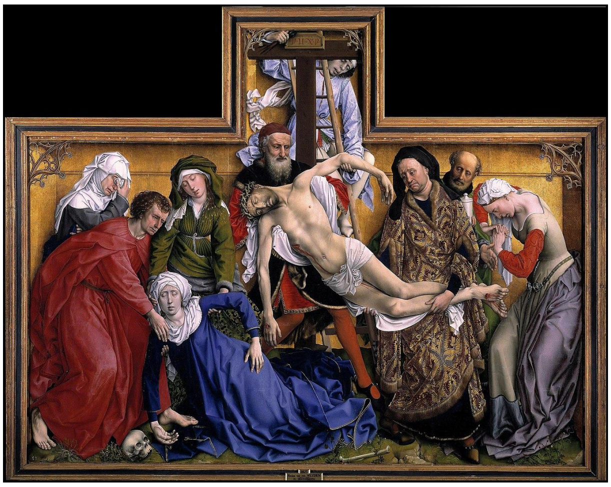

Figure 2.6: Rogier van der Weyden, Deposition (Descent from the Cross). Museo del Prado, Madrid, Spain. Ca. 1435. Oil on panel. Wikimedia Commons. It is clear which among the mourning figures represents Mary.

The appearance of the mineral can vary from an intense blue to a grayer shade, depending on quality. The lazurite is the source of the blue color, but the presence of other impurities such as calcite, pyrite or other silicates reduced the quality of the mineral. Indeed, due to the presence of these impurities, simple grinding of the material to dust wasn't enough to extract a vibrant pigment. So in the 13th century a new extraction method was devised. The most detailed account of said method is the *Libro dell'arte* by the 15th century Tuscan painter Cennino d'Andrea Cennini [18]. The method, still used today, involves several steps. First, the lapis lazuli should be ground to a powder. Then it should be incorporated into a dough made out of bees' wax, pine resin, mastic and oils. This dough should be kneaded and then left to dry for several days. To extract the pigment, the dry dough should be reheated with warm water and once malleable, submerged in a solution of water and lye (potassium carbonate). While continuing to knead the dough, the blue particles will start migrating into the solution, coloring it, and precipitating at the bottom, where they can be recovered, while the other impurities will remain trapped in the dough. By repeating the kneading process with the same dough in another vessel with a clean solution of water and lye one can extract pigments of progressively decreasing quality.

2.4. Artificial Ultramarine Blue

The history of artificial ultramarine starts with a passage in Goethe's *Italienische Reise* (in English: Italian journey), published in 1817, where he reports his travels across thirty years earlier. In 1787, near Palermo, Sicily, he noticed blue deposits on the walls of some lime kilns. He mentions that the crystal blue masses were cut and utilized locally as a replacement for lapis lazuli in ornamental work, but he does not mention whether someone had thought of grinding the material into a pigment. The same blue mass was rediscovered in 1814 in soda kilns in a glass factory in France and subsequent analyses showed a surprising similarity of the material to the natural ultramarine blue extracted from lapis lazuli. Thus in 1824 the *Societé d'Éncouragement pour l'Industrie Nationale*, located in Paris, issued a prize of 6000 francs for the development of a practical industrial procedure that would allow synthetic ultramarine to be produced at a cost of no more than 300 francs per kilogram [19]. The prize was awarded four years later, in February of 1828, to Jean Baptiste Guimet, who started selling his pigment at roughly one tenth of the price of natural ultramarine. Notably, a slightly different method was independently discovered by the German Christian Gmelin, who published his process just one month after Guimet.

The process devised by Guimet and Gmelin has remained largely unchanged till today. It consists of heating a mixture of metakaolin (which is a type of kaolin clay), anhydrous sodium carbonate (Na_2CO_3), sulfur and charcoal (according to the recipe explained in [20]). These reagents are mixed in the desired proportions, finely ground together and tightly packed in a crucible. The mixture is then calcined in furnaces (heated to temperatures between 600°C and 800 °C) under controlled atmosphere. The first firing is done under reducing condition (with a lid), then, another firing is done under oxidizing conditions (removing the lid). After several hours of firing, which may range from 3 to 48 hours, depending on the desired quality and yield, the mixture will present some vibrant blue parts. To extract the pigment these colored parts must be separated from the rest, washed, dried and ground.

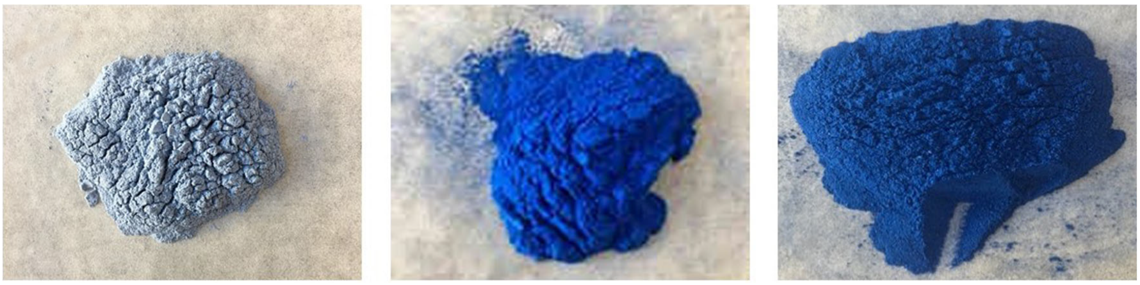

Figure 2.7: Different qualities of artificial ultramarine blue pigment obtained by changing the ratios of ingredients. Generally speaking, the greater the proportion of S, the deeper the blue. Taken from [21].

Shortly after the discovery of the synthesis of the ultramarine blue pigment, pink and green pigments having the same structure as ultramarine blue and also containing sulfur species were synthesized (figure 2.8a). In fact, by slightly changing the ratios of the ingredients, the temperature and duration of the firings pigments like ultramarine green or ultramarine red can be synthesized (see patent [22]) . The inclusion of other ingredients can significantly alter the color of the resulting pigment. For example, the inclusion of selenium salts can form the red pigment "red selenium ultramarine" (figure 2.8b) [23]. These ultramarine pigments are as stable as blue ultramarine but have rather poor tinting strength, which is why they seem not to have found a place in the artist's palette.

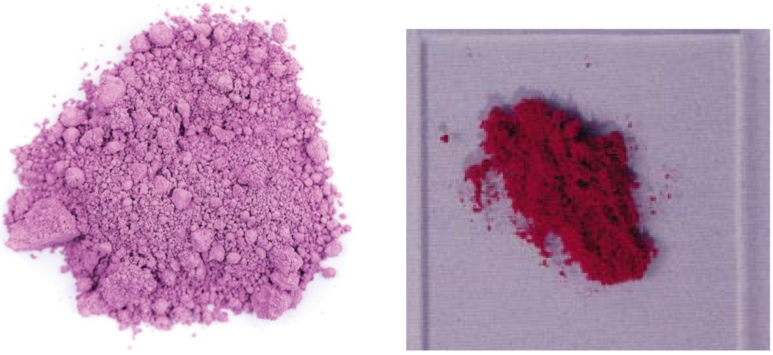

(a)

(b)

Figure 2.8: a) Ultramarine red, taken from the Kremer Pigmente online catalog. b) Red selenium ultramarine, taken from [23].

2.5. State of the art

The major quarries of lapis lazuli are located in Afghanistan, Siberia and Chile. Research has focused on the challenging task of identifying the provenance of lapis lazuli through the identification of distinguishable molecular markers in different natural lapis lazuli stones and pigments, as well as distinguishing between natural and synthetic origins [9, 11, 24–26].

Osticioli et al. [25] have proposed an analytical protocol for the differentiation between natural (lapis lazuli) and artificial ultramarine blue pigments building a setup that combines Laser Induced Breakdown Spectroscopy (LIBS) and micro-Raman spectroscopy. They managed to differentiate between the natural and artificial commercial pigments on the basis of peaks ascribed to calcium, which are attributed to the naturally occurring calcite in lapis lazuli.

Schimdt et al. [11] have employed both destructive and non-invasive techniques to distinguish between natural and artificial ultramarine blue. They used Raman microspectroscopy (with 785 nm excitation), Scanning Electron Microscopy Energy Dispersive X-Ray Spectroscopy (SEM–EDX), Electron Microprobe Analysis (EMPA), and Laser Ablation Inductively Coupled Plasma Mass Spectrometry (LA-ICPMS), and confirmed the presence of diopside as a naturally occurring mineral contaminant in lapis lazuli. Trace element analysis of the diopside inclusions revealed traces of transition metals like vanadium, chromium, nickel, manganese, iron, arsenic, and titanium. The authors noted that observation of trace metals required destructive analysis, which cannot be used for most works of art. They also noted that the nonlazurite features coming from the impurities were observable in non-destructive Raman analysis and that the way to correctly identify the provenance of different natural ultramarine pigments may lie in the interpretation of these features. Raman spectroscopy was therefore proposed as a the main technique to distinguish not only between artificial and natural ultramarine, but also between pigments with different geographical origin.

Favaro et al. [9] used Fourier Transformed Infrared spectroscopy (FT-IR), X-ray Diffractometry (XRD) and Energy Dispersive Spectroscopy (EDS) to study both artificial and natural ultramarine blue pigments. They found that FT-IR spectroscopy was not a suitable technique for distinguishing the provenance of lapis lazuli, but ir can help distinguish between synthetic and natural pigments thanks to the presence of a weak absorbance band at 2340 cm^{-1} . On the other hand, EDS elemental composition and XRD patterns showed the presence of specific mineral phases associated with specific lapis lazuli sources, and could be used to distinguish the provenance of the stones and possibly the corresponding blue pigments as well. The main distinctive mineral phases are sanidine and wollastonite in Afghan and Chilean lapis lazuli, respectively, while nepheline, phlogopite and sodalite were specific to both Afghan and Siberian samples. Diopside appeared to be an accessory phase of lazurite that is unrelated to the provenance of the material.

Re et al. [24] have studied trace elements in pyrite (FeS_2) crystals of lapis lazuli of known origin with micro-PIXE and found new markers in stones from known origins: Afghanistan, Pamir mountains (located just north-east of Badakshan, Afghanistan) Siberia and Chile. These markers allowed them to distinguish among the four provenances. Afghan samples showed high values of nickel concentration; Pamir samples generally presented a quantity of copper much higher than that in lapis lazuli of all the other origins; some of the Chilean samples were characterized by the presence of selenium inside pyrite crystals; Siberian samples also contained relatively high quantities of nickel, but what differentiated them was the presence of a sulfur-lacking iron mineral, not found in other samples.

Lo Giudice et al. [26] have proposed a protocol for determining the provenance of lapis lazuli rocks used for carved artifacts by analyzing elemental markers with micro-Proton-Induced X-ray Emission (µ-PIXE) and microionoluminescence (IL). The advantage of these techniques being that they are non-invasive and applicable in air, and do not require preparation of sample. Unfortunately no work has been done on lapis lazuli in pigment form.

In summary, almost every research group has employed Raman spectroscopy at some point, which has solidified its role as the main technique to study ultramarine blue pigments in works of art. Its main advantages are that it is a non-invasive technique and can also be portable, opening the possibility for in situ applications. In addition, during the years researchers have been able to extract more and more information out of the Raman spectra of lapis lazuli, in particular with reference to the detection of Raman peaks of lazurite - the main component of ultramarine - and diopside - a mineral commonly associated with lapis lazuli in nature [11].

This work is focused on techniques that exploit fluorescence: time resolved photoluminescence spectroscopy and imaging, which have shown great potential.

PL spectroscopy and imaging have been less used in cultural heritage analysis because of the complications in understanding the detected emission spectra. Indeed, the interpretation of the emission spectrum is not simple due to the superimposition of the emission from various species, the intrinsic similarities in the emission spectra of different fluorophores, and the effects of reabsorption or scattering attributed to paint composition

[27]. Moreover, when using steady-state excitation and detection schemes, only the most strongly emitting materials (typically protective varnish and organic compounds) can be detected, overshadowing weaker emissions.

Despite its shortcomings, PL is a very sensitive technique that allows to detect small amounts of luminescent compounds in a non-emitting background [28] and has found great success in the analysis of luminescent, semiconductor-based pigments such as zinc white and cadmium yellow and red [7]. Time-resolved PL measurements are a major improvement to steady-state systems because they can resolve the decay dynamics of the fluorescence and separate the emissions occurring at different timescales. A notable feature is that they can also be used in situ [29]. However, since the emission decay depends on de-excitation processes, both radiative and not, which are highly influenced by the microenvironment of fluorophore, one cannot identify an emitting material by looking at the emission lifetime alone. Nonetheless, by combining the temporal information with the spectral one it is possible to gain further insight in the PL process. This approach has proven particularly effective in the analysis of modern paintings that contain both modern inorganic pigments, with a microsecond fluorescence lifetime, and organic compounds with nanosecond lifetimes [7].

The aim of this work is to expand the reach of time resolved PL techniques by characterizing the PL emission of different variants of ultramarine blue pigments, to see if it would be possible to use these techniques to detect them in paintings and infer their provenance and nature.

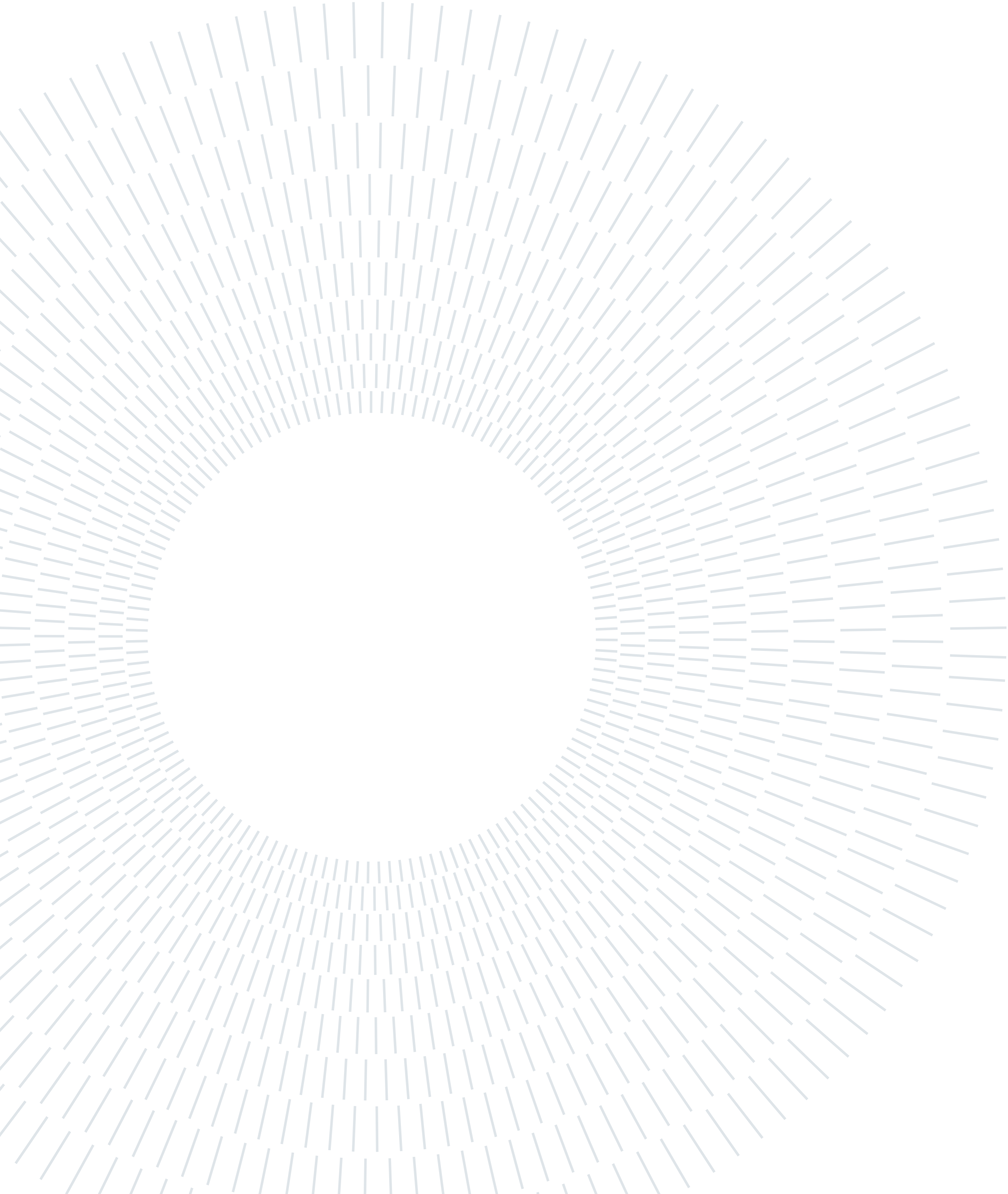

3 | Materials

3.1. The samples

In this work a total of 10 samples of ultramarine blue pigments in powder form have been analyzed, which will be referred to as "UB" accompanied by a number. Samples UB1 through UB9 are called “natural ultramarine" because they have been obtained by processing lapis lazuli stones. Samples UB1 to UB6 and UB9* all come from lapis lazuli mined in Badakshan, Afghanistan, whereas UB7 and UB8 are made from Chilean lapis lazuli. UB10 is the only synthetic ultramarine blue, obtained by the industrial method pioneered by Guimet.

Code	**Brand**	**Number**	**Name**
UB1	Kremer Pigmente	10500	Lapis Lazuli, grayish blue (natural)
UB2	Kremer Pigmente	10580	Ultramarine Ash, byproduct of 10530
UB3	Kremer Pigmente	10510	Lapis Lazuli, medium quality (natural)
UB4	Kremer Pigmente	10520	Lapis Lazuli, good quality (natural)
UB5	Kremer Pigmente	10530	Lapis Lazuli, purest ("Fra Angelico blue")
UB6	Kremer Pigmente	10540	Lapis Lazuli light (made from crystals)
UB7	Kremer Pigmente	1056045	Lapis Lazuli from Chile (particles 38-45 µm)
UB8	Kremer Pigmente	1056025	Lapis Lazuli from Chile (particles 20-25 µm)
UB9	Zecchi		Lapis Lazuli from Afghanistan
UB10	Kremer Pigmente	45000	Ultramarine Blue, very dark (synthetic)

Table 3.1: Table of all the studied samples.

In figure 3.2 a picture for each sample observed with an optical microscope at 10X magnification is shown.

---

*Since no information was provided about UB9 other than its provenance, it has been decided not to include it in this analysis.

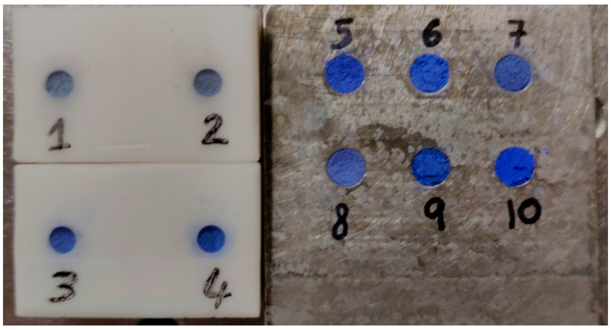
5
6
7
1
2
8
9
10
3
4

Figure 3.1: All samples in powder form.

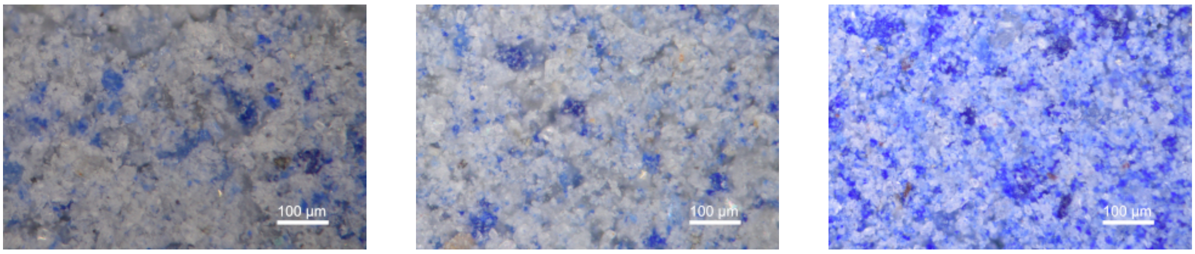
100 µm
100 µm
100 µm

(a) UB1. (b) UB2. (c) UB3.

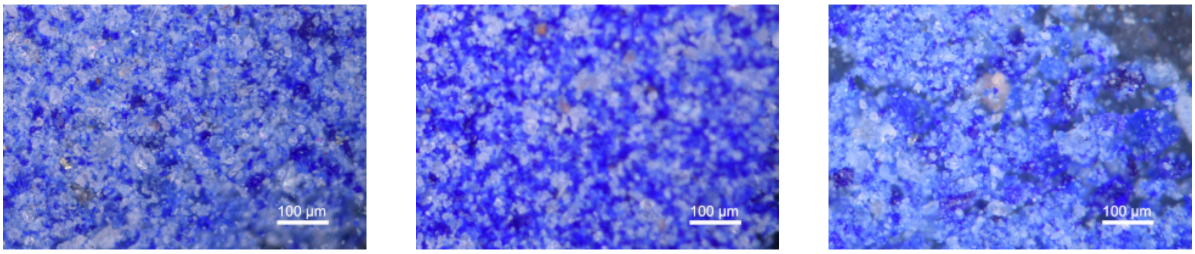
100 µm
100 µm
100 µm

(d) UB4. (e) UB5. (f) UB6.

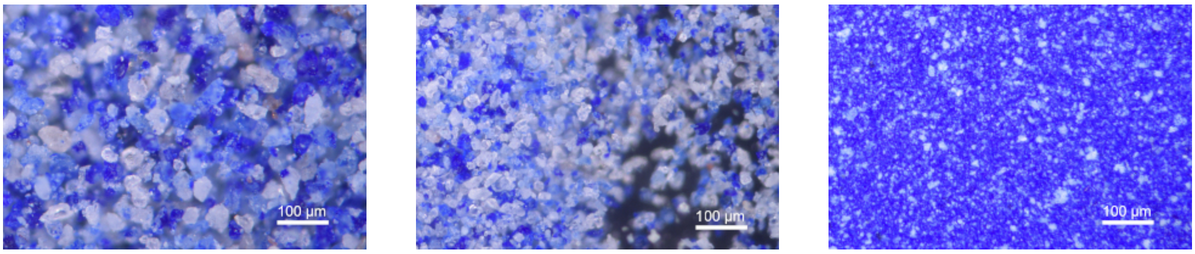
100 µm
100 µm
100 µm

(g) UB7. (h) UB8. (i) UB10.

Figure 3.2: All samples observed under a microscope at 10X zoom illuminated with visible light.

UB1 is good quality Afghan lapis lazuli milled, washed and sieved. It appears as a grayish blue powder.

UB2 is called "ultramarine ash" and is the byproduct of the extraction of UB5, the highest quality among natural pigments. It contains a high proportion of colorless material with only a few blue particles and is used as blue glazing pigment.

UB3 comes from selected Afghan lapis lazuli milled, washed and sieved. The density of blue particles is noticeably higher.

UB4 comes from even higher quality Afghan lapis lazuli which is milled, the pyrite is mostly removed, then washed and sieved.The resulting pigment has a deeper blue color than UB3.

UB5 is also known as "Fra Angelico blue" and is the highest quality natural ultramarine. It also comes from selected Afghan lapis lazuli that is milled, then pyrite is removed, then all is cleaned according to Cennino Cennini's method (presented in section 2.3).

UB6 comes from the processing of lapis lazuli minerals mined with explosives. The colored fragments are once again milled, washed and sieved.

UB7 and UB8 come from Chilean lapis lazuli and are extracted with modern machinery. They only differ in particle size (UB7 has particles dimensions of about 38-45 µm, while in UB8 their range is about 20-25 µm) and were studied to see if particle size impacted the photoluminescent properties in any way. They both present high density of blue particles.

UB10 is the synthetic ultramarine blue. It is obtained with Guimet's method. It has the highest density of blue particles and produces the most intense color when made into a paint.

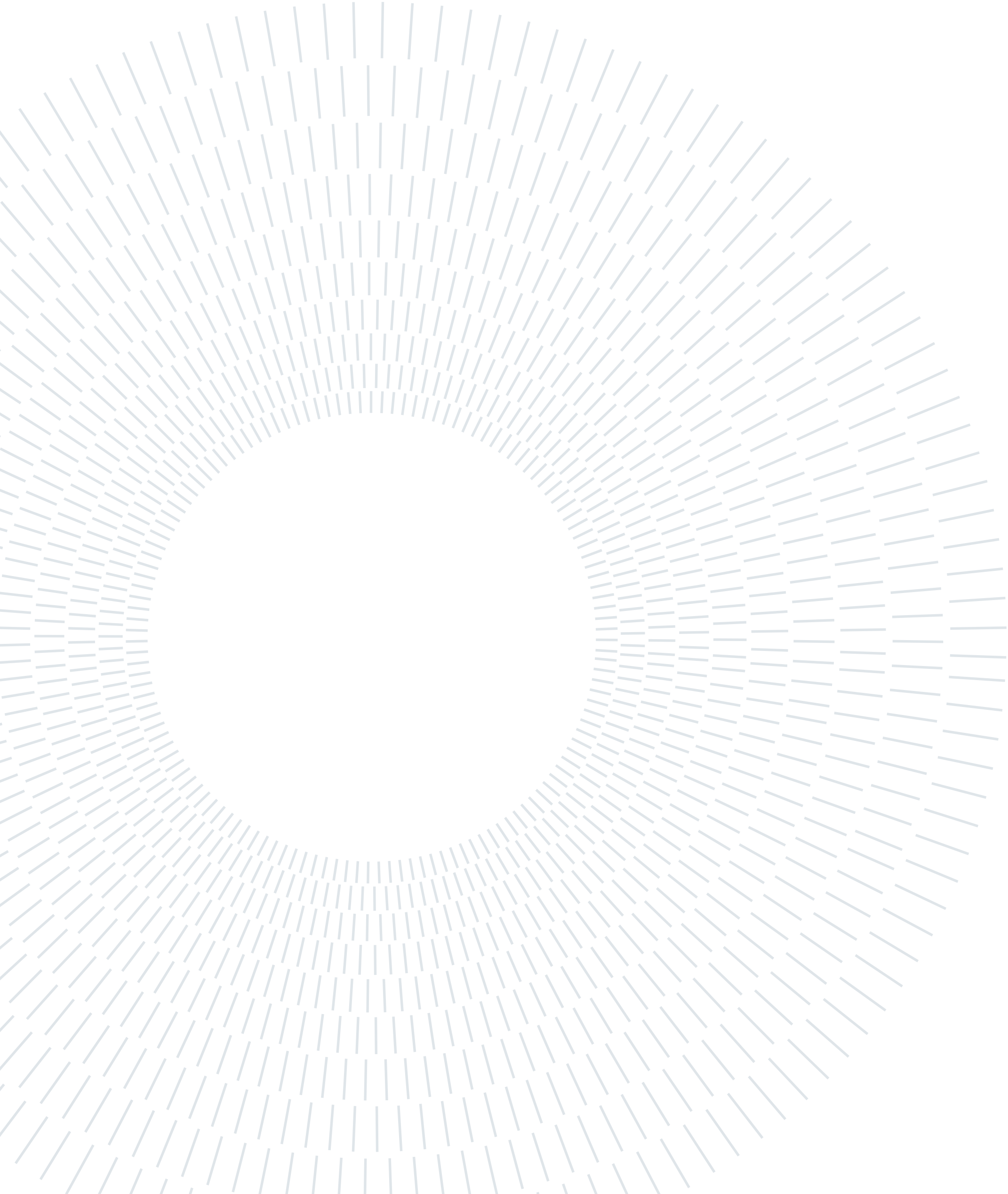

4 | Methods

In this research both continuous and time gated methods were employed to analyze the photoluminescent properties of ultramarine blue pigments. Details on the all setups are provided in the following paragraphs. Here we remark that all the three time gated setups (Time Resolved Photoluminescence spectroscopy, Fluorescence Lifetime Imaging and Time Gated Hyperspectral Imaging) employ:

- the same nanosecond pulsed laser source (third harmonic of Nd:YAG Q-switched laser, FTSS 355-50 CryLas GmbH, $\lambda = 355$ nm, 1.0 ns pulse, 100 Hz repetition rate, which is conveyed to the sample by the same multimode,silica, optical fiber with 600 µm diameter and appropriate optics) to excite photoluminescence from the samples;
- the same imaging sensor, which consists of a time-gated intensifier (C9546-03, Hamamatsu Photonics) optically coupled to a CCD imaging camera (Retiga R6, Qimaging, spectral range 300–1000 nm). The temporal gating allows detection of photons in a time window of any duration between 3 ns to 1 ms;
- the same precision delay generator (DG535, Stanford Research System), for the temporal sampling of the transient decay kinetic of the PL emissions, and a custom-built trigger unit. The whole system has an overall temporal jitter close to 500 ps.

4.1. Optical Microscopy

A Leica DM RE microscope equipped with multiple objectives (5X, 10X, 20X and 50X) and a color digital camera (Nikon D750) was used to observe the samples in darkfield and epifluorescence cofigurations. A sample of each of the pigments was taken and sandwiched in between two 22mm x 22mm x 0.2 mm silica coverslips. In the epifluroescence mode, optical emission of the samples was excited with the 365 nm line of a steady state mercury lamp. Detection in the visible range was performed with the adoption of a dichroic mirror (T365lpxt, Chroma Technology Corporation) and a transmission filter (FELH0400, Thorlabs Inc.). The samples were scanned for interesting landmarks, like a particularly bright fluorescent particle, or groups of fluorescent particles of different species (for clarity some examples of these images are reported, see figures 4.1 and 4.2). Although this step offered no quantitative information, it was useful to qualitatively characterize each sample.

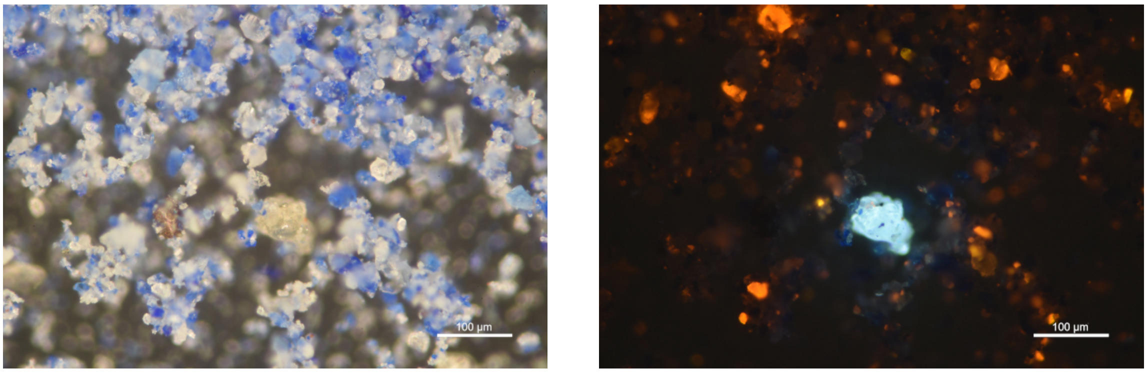

(a) (b)

Figure 4.1: Area of UB4 with blue fluorescent particle amidst orange fluorescent particles. a) Illuminated with normal light. b) Illuminated with UV light.

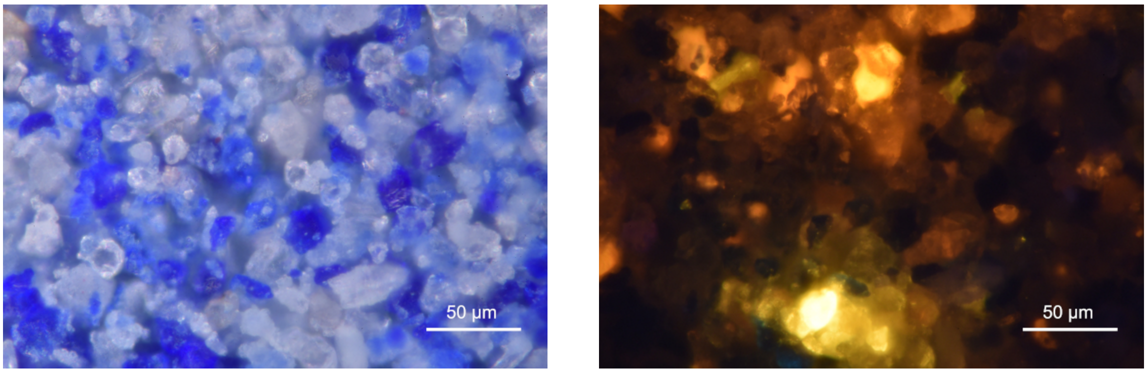

(a) (b)

Figure 4.2: Area of UB8 with orange and yellow fluorescent particles facing each other. a) Illuminated with normal light. b) Illuminated with UV light.

4.2. Time-Resolved Photoluminescence (TRPL) Spectroscopy

Time-resolved photoluminescence (TRPL) analysis involves studying the evolution of the photoluminescence (PL) spectrum during the emission decay of a single point of the sample.

4.2.1. TRPL Setup

The laser light is coupled to a multimode silica fiber (600 µm core) and, through a proper optical system, illuminates a spot on the sample surface of 1 mm diameter with an average power density of 1 mW/mm^2. The PL emission from sample is collected in a back-scattering geometry and focused into the entrance slit of an imaging spectrometer (Acton Research 2300i, focal length = 300 mm, f/4 aperture) coupled with the time-gated intensified camera. This spectrometer features a 150 lpmm grating and allows recording of PL spectra in the spectral range of 380–820 nm with a spectral resolution of 10 nm.

4.2.2. Measurement protocol

The measurement procedure involves detecting a sequence of PL gated spectra at different delays with respect to the laser pulses. We refer to the whole collection of time-gated spectra as "TRPL dataset". Once a TRPL dataset has been collected, it is possible to extract time-gated PL spectra in selected temporal windows (as shown in figure 4.3c). In addition, from the normalized TRPL datasets, which are datasets where the signal of each wavelength is normalized with respect to the value reading at t = 0 ns, one can observe the emission decay of selected bands (as shown in figure 4.3d).

In this work three different TRPL datasets have been collected for each sample, related to the nanoseconds, microseconds and tens of microseconds emissions*.

Kinetic	**Gate**	**Delay range after excitation**
nanoseconds	10 ns	0-70 ns
microseconds	1 µs	0.2-55 µs
tens of microseconds	10 µs	1-200 µs

Table 4.1: Parameters used for the three different decay kinetics.

---

*The tens of microseconds emission was measured only on samples that showed signs of a persistent emission when conducting measurements of the microseconds emission.

In figure 4.3a an example of TRPL dataset is given, while in (b) the same dataset is shown after intensity normalization at zero delay. In panels (c) and (d) examples of time-gated spectra and emission decay kinetics extracted from the dataset are given.

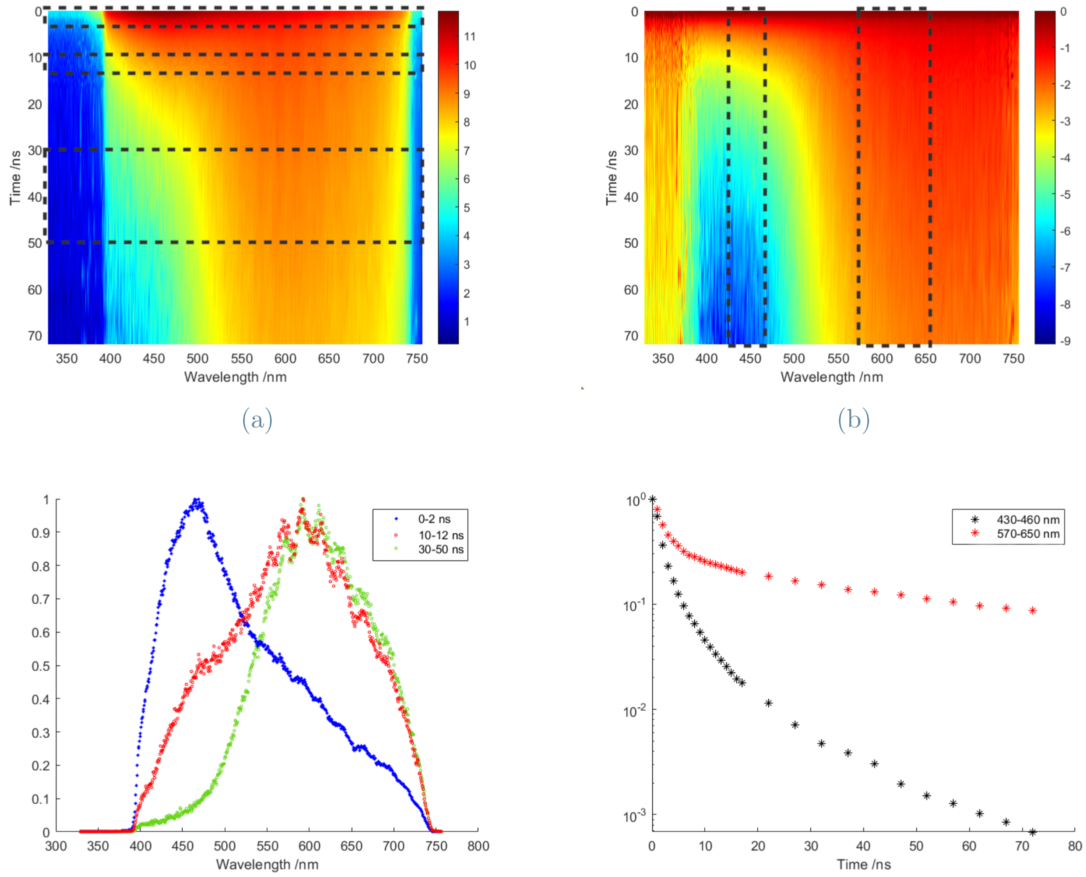

(a)

(b)

(c)

(d)

Figure 4.3: a) Gated spectra of the nanoseconds emission of UB3. b) Same measurement normalized with respect to the value observed for each wavelength at t=0 ns. c) Gated spectra integrated and normalized in the time windows represented by the black dashed rectangles in figure 4.3a . d) Decays of bands in the wavelength interval represented by the black dashed rectangles in figure 4.3b.

After proper preprocessing of the collected data points, which includes spectral calibration, correction for detector efficiency, glitch removal, Savitzky-Golay filtering with appropriate parameters and a final normalization (figure 4.4), the time-gated spectrum of the sample in the chosen time window can be calculated.

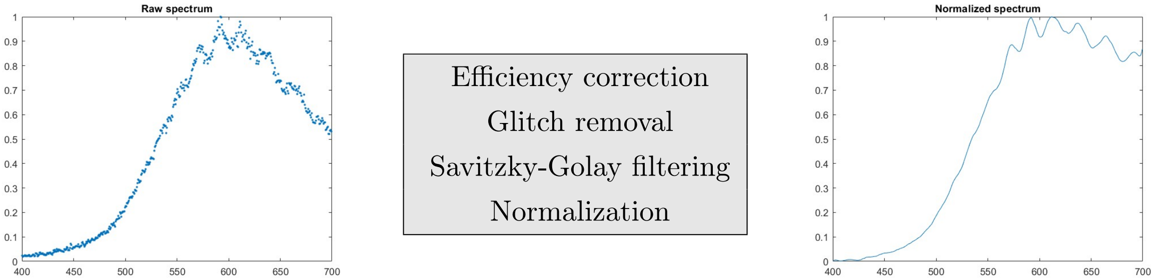

Figure 4.4: Illustration of preprocessing steps for the extraction of a spectrum from raw data points.

To observe the decay kinetics in a selected spectral window, a multiexponential decay with a maximum of three components is fitted to the kinetic data using nonlinear least-squares fitting methods applied to the model function $M(t)$:

$$M(t) = \sum_{i=1}^{3} A_i \tau_i (1 - e^{-w/\tau_i}) e^{-t/\tau_i} \tag{4.1}$$

where τ_i and A_i are the lifetime and the intensity of the i-th decay component, respectively, while w is the width of the experimental gate.

The effective lifetime τ_{eff} is calculated as the weighted average of each component τ_i,where the weight is $A_i\tau_i$[†].

$$\tau_{eff} = \frac{\sum_i A_i \tau_i^2}{\sum_i A_i \tau_i} \tag{4.2}$$

As an example, the fitting of the experimental data of the decay of the 430-460 nm band to the tri-exponential model of UB3 is shown below.

[†] This choice of weight can be understood by modelling the intensity of fluorescence emission after a pulsed excitation with a mono-exponential function, $f(t) = Ae^{-t/\tau}$, where A represents the initial intensity and τ the fluorescence lifetime. By integrating this expression from $t = 0$ to $t = \infty$ we obtain $A\tau$. $A_i\tau_i$ therefore essentially represents the number of photons emitted by the i-th decay component.

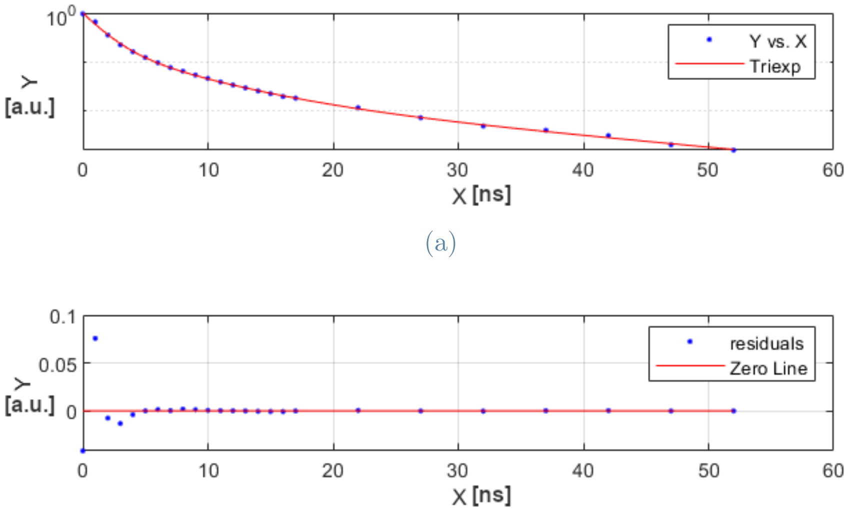

(a)

(b)

Figure 4.5: a) Fitting of the the tri-exponential model function to the experimental data of the decay of the 430-460 nm band. b) Plot of the residuals.

	τ **[ns]**	**A%**	**A*τ %**
1st component	5.2486	7.31	20.55
2nd component	1.4962	92.12	73.84
3rd component	18.3987	0.57	5.61
τ_{eff} **[ns]**	3.2154		
$\mathbf{R^2}$	0.9972		

Table 4.2: Table with the computed time constants of the three exponential components τ, their amplitudes expressed in percentages A and the weights $A\tau$ expressed in percentages. This table also includes the calculated effective lifetime τ_{eff} and the coefficient of determination R^2.

4.3. Fluorescence Lifetime Imaging (FLIM)

FLIM works by measuring the temporal properties of fluorescent emission at every point in a sample, which allows for the generation of a lifetime map of the analyzed region. This technique brings together the benefits of time-resolved spectroscopy and fluorescence imaging. The lifetime information effectively differentiates between various fluorophores, while the imaging capability of FLIM facilitates the localization of different fluorescent materials within the observed region. One of the limits of this technique is the fact that due to the high sensitivity of the lifetime to the fluorophore micro-environment, this parameter cannot be used for univocal material identification.

4.3.1. FLIM Setup

In the FLIM setup, the time-gated intensified camera is coupled to an optical microscope mounting a 15X reflective objective. The laser is conveyed to the sample through the optical fiber and via appropriate optics,including a dichroic mirror (Semrock, Brightline FF389-Di01). The field of view, also referred to as "region of interest" or "ROI", is a circular area of 1 mm in diameter.

The FLIM measurement is not spectrally resolved: the image detector, using a multialkali photocathode, can detect photons emitted across the 400-900 nm spectral range. To isolate emissions from specific spectral regions, one could apply a fitting band-pass optical filter in front of the image intensifier, although this was not necessary in this work.

Typically, the acquisition time for an entire luminescence lifetime imaging dataset is below 5 minutes. The lifetime map is calculated pixel-by-pixel by modelling the emission decays with a mono-exponential function and is then displayed as a map in a false color representation (as explained in [30] and as shown in figure 4.7). Notably, in general luminescence cannot be modelled as a mono-exponential decay due to the multiplicity of relaxation paths (both radiative and non-radiative) a fluorescent species can undergo. Nevertheless, the reconstruction of the effective lifetime map based on a simple mono-exponential decay provides sufficient contrast to distinguish between different emitting species and is also independent from the intensity of the emission.

4.3.2. Measurement protocol

The fluorescence decay is sampled over time by repeated measurements with different delays between the excitation pulses and the leading edge of the gate, resulting in a sequence of fluorescence images captured at various time instants (as shown in figure 4.6).

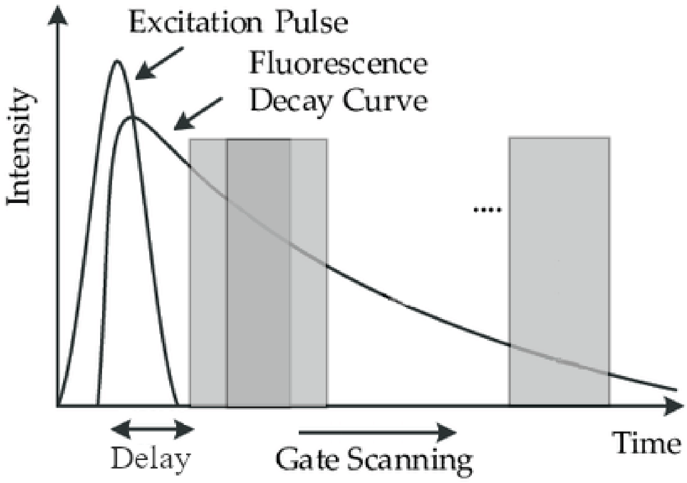

Figure 4.6: Representation of gate scanning method for the observation of the decay curve (adapted from [31]).

In this work, a 10 ns gate width has been used to detect nanosecond kinetics of emission. For decay kinetics in the microsecond range, the gate width has been increased to 1 µs to better capture the signal. The time intervals observed have also been appropriately adjusted for each sample, since the lifetimes of fluorescent particles varied greatly (see table 4.3).

Kinetic	**Gate**	**Delay range after excitation**
nanosecond	10 ns	0 - 100 ns
microsecond	1 µs	0.15 - 20 µs

Table 4.3: Parameters for the FLIM measurements of the different decay kinetics.

The result of the measurement are three maps of the sample:

- the intensity map, which displays the intensity of the fluorescence;
- the lifetime map, which is represents in false colors the mono-exponentially fitted lifetime of each pixel;
- the HSV map, which combines the previous two maps: the luminance of each pixel is correlated with the fluorescence amplitude, whereas the hue represents the lifetime of the pixel.

As an example, the FLIM measurement of UB5 is presented below.

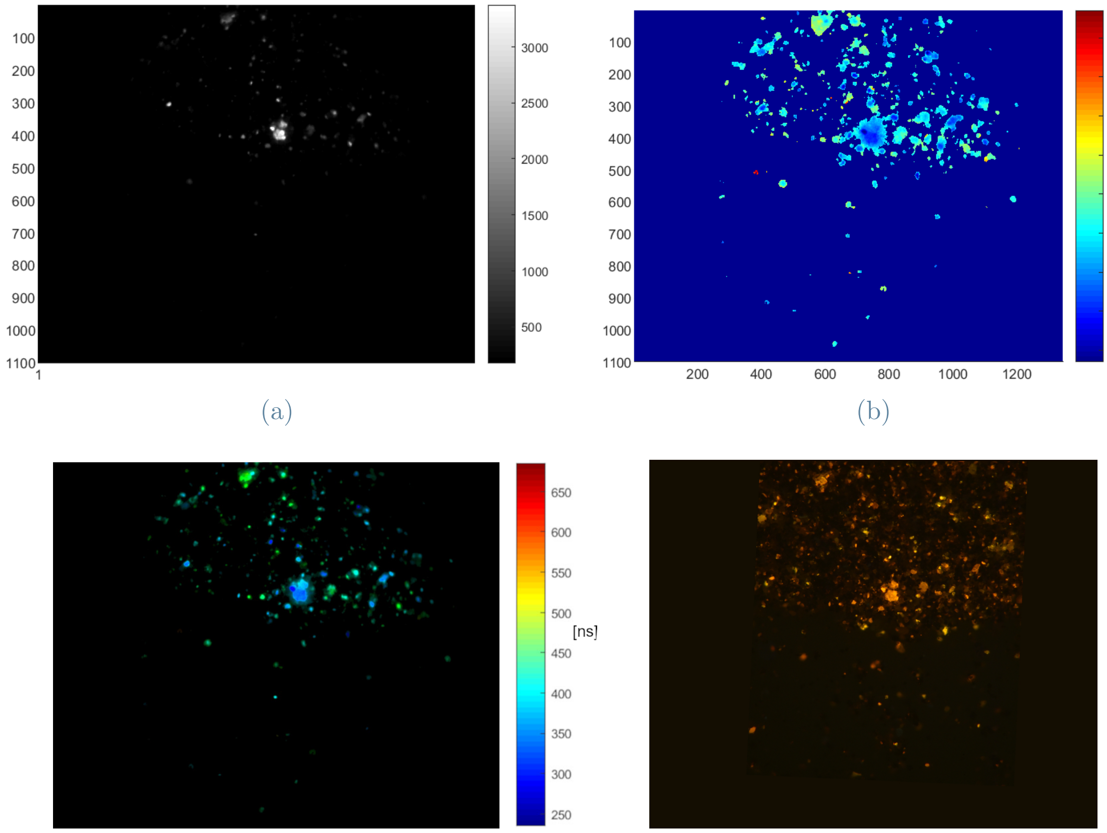

(a)

(b)

(c)

(d)

Figure 4.7: Example of a typical FLIM measurement. a) Intensity map of the ROI. b) Lifetime map of the ROI. c) HSV map of the ROI. The different colors of the pixels represent different lifetimes. d) Picture of the ROI of the sample taken with a microscope at 15X zoom, illuminated with UV light.

To better distinguish between emitting species, the pixels can be clustered into up to 4 clusters on the basis of similar lifetimes (as in figure 4.8a, where the pixels have been clustered into three). For each of these clusters, an average decay kinetic is calculated (as shown in figure 4.8b).

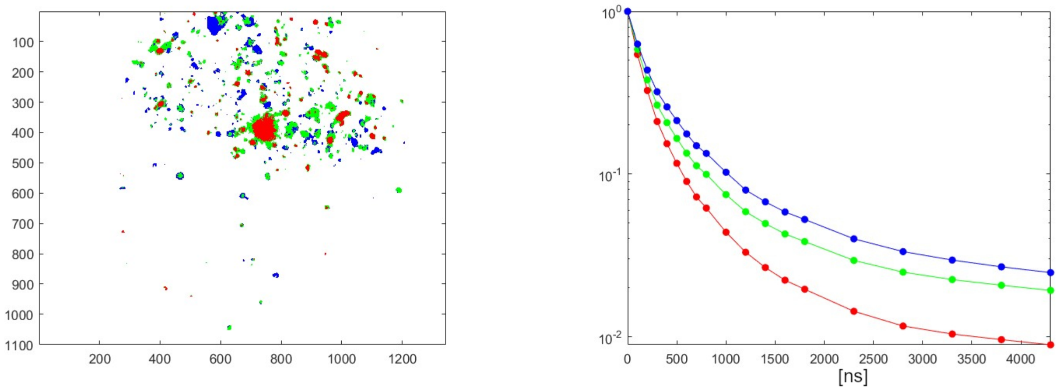

(a) (b)

Figure 4.8: a) Example of clusterization. The pixels with similar lifetimes are grouped together into 3 clusters. b) Average decay kinetic of the clusters.

4.4. Time Gated Hyperspectral Imaging (TG-HSI)

Hyperspectral imaging consists of capturing images in numerous narrow and contiguous bands across the electromagnetic spectrum. Unlike traditional RGB (Red-Green-Blue) imaging, which captures only three color bands, hyperspectral imaging can capture hundreds or even thousands of bands, where each band basically corresponds to a specific wavelength of light, providing detailed spectral information about the examined object.

In the cultural heritage conservation field, multispectral and hyperspectral imaging (MSI and HSI respectively) are typically employed to detect and study light diffusely reflected by the surface of an art piece [32] with the aim of revealing hidden details, like preparatory sketches, retrieving accurate color information and identifying and mapping the materials used (like pigments or varnishes) [33].

In this work, hyperspectral imaging has been employed together with photoluminescence measurements and the time gated approach to map different luminescent species on the basis of their different spectral and lifetime properties.

4.4.1. TG-HSI Setup

The TG-HSI setup is similar to the FLIM experimental setup previously described. The only difference is the inclusion of the TWINS interferometric system (fully described in the patent [34] and papers [35], [36], [37]), a common-path birefringent interferometer placed along the collection optical path that allows to obtain high-quality interferograms for each point of the field of view. By means of the Fourier transform, the interferograms are then converted to high-quality spectra. The spectral resolution of the device is set by the maximum scan delay introduced by the interferometer and can be as good as 4 nm at 600 nm wavelength. The full setup is schematized in figure 4.9. The field of view is once again a circular area of 1 mm in diameter, illuminated with an average power of 1 mW/mm^2.

4.4.2. Measurement protocol

The resulting measurements are maps of the field of view (also referred to as "region of interest" or "ROI") colorized according to the measured spectra in each pixel. Averaged PL spectra can be extracted from selected pixels on the map, which in this case are constituted by single fluorescent particles. With the time gated approach, the maps of the spectra were recorded at three different delays with respect to the exciting pulse, allowing us to observe the spectra of fluorescent particles at different time points.

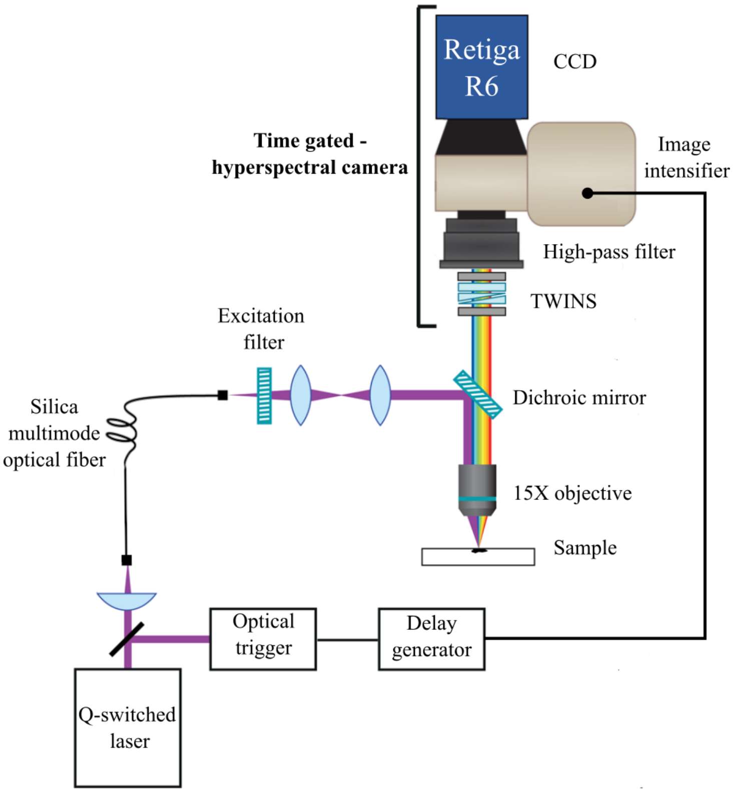
Retiga R6
CCD
Time gated - hyperspectral camera
Image intensifier
High-pass filter
TWINS
Excitation filter
Dichroic mirror
Silica multimode optical fiber
15X objective
Sample
Optical trigger
Delay generator
Q-switched laser

Figure 4.9: TG-HSI setup. Figure adapted from [38].

Kinetic	**Gate**	**Delay after excitation**
nanosecond	100 ns	0 ns
microsecond	1 µs	0.15 µs
tens of microseconds	10 µs	1 µs

Table 4.4: Parameters for the TG-HSI measurements of the three decay kinetics.

As an example, the TG-HSI measurements of UB6 are presented below.

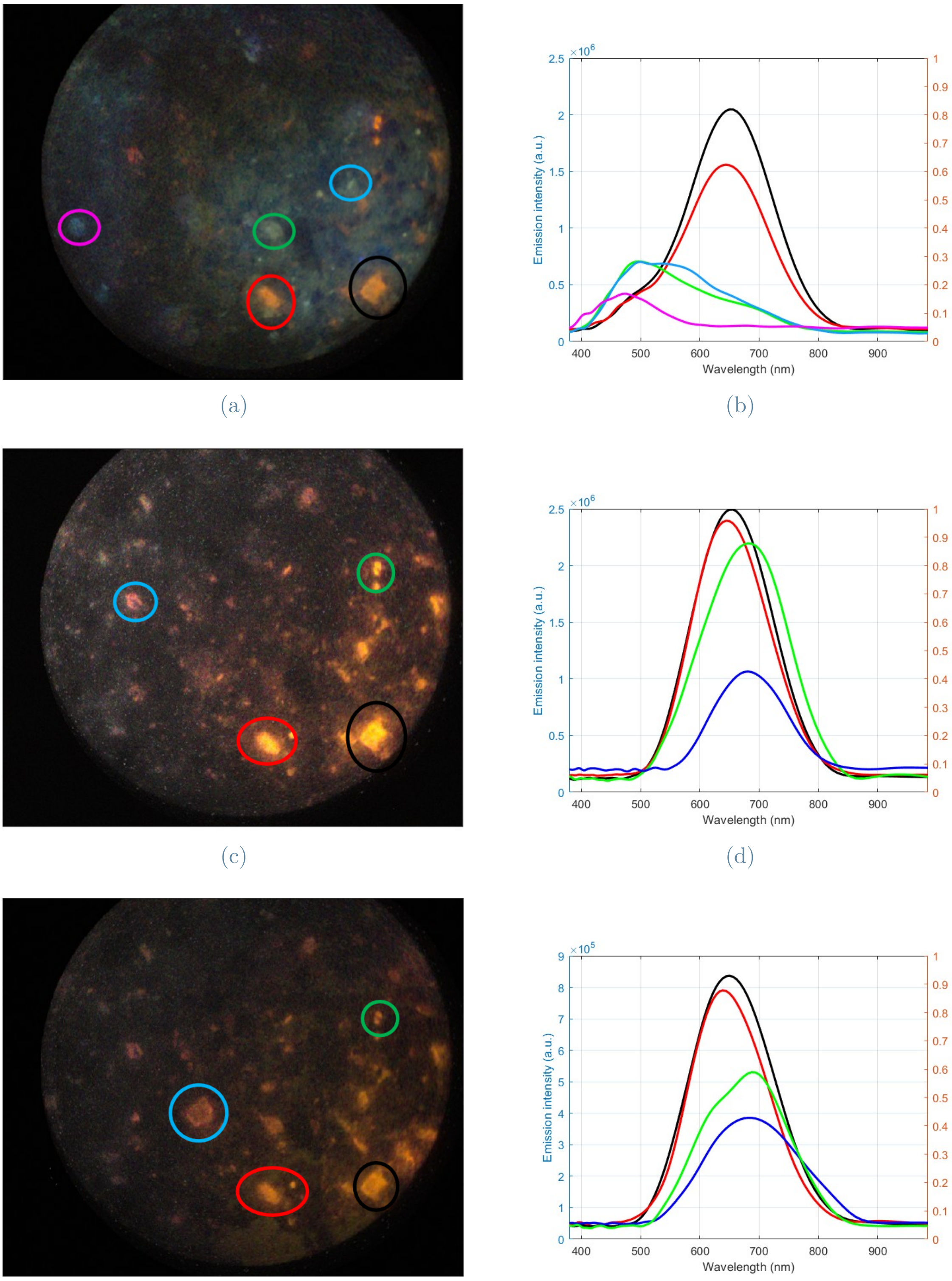

(a) (b)

(c) (d)

(e) (f)

Figure 4.10: (LEFT) Maps of the ROI of the sample colorized according to the measured spectra. The circled particles are the ones whose spectrum is being shown in the corresponding colors in the plots on the right. (RIGHT) Spectra of the circled particles in the corresponding color. a,b) Map and spectra of the nanoseconds emission (delay after excitation: 0 ns; gate: 100 ns). c,d) Map and spectra of the microseconds emission (delay after excitation: 0.15 µs; gate: 1 µs). e,f) Map and spectra of the tens of microseconds emission (delay after excitation: 1 µs; gate: 10 µs).

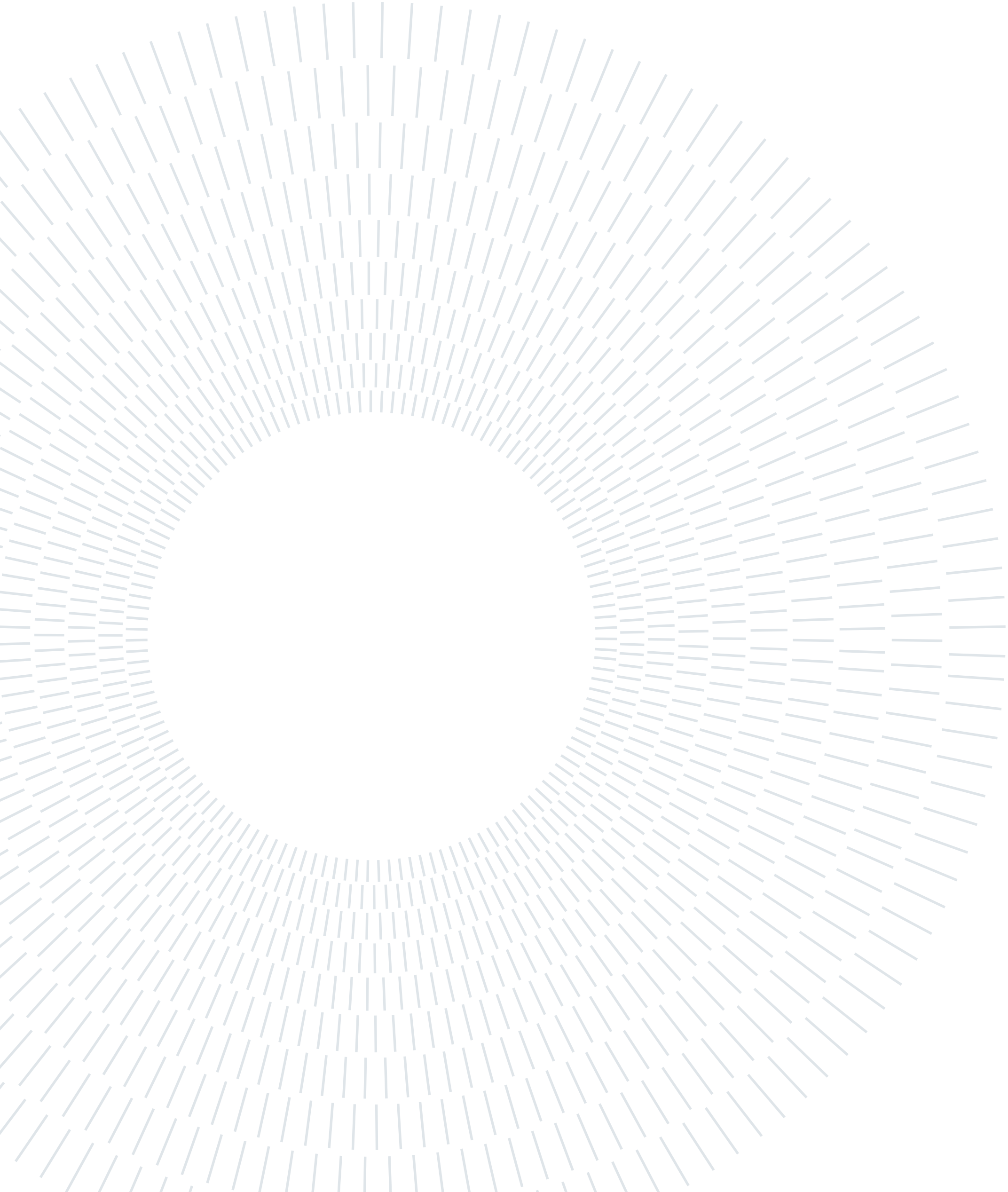

5 | Results

5.1. Optical Microscopy

In the following figures we show the samples under visible light (figure 5.1), their optical emission following UV excitation (figure 5.2) and the two digitally superimposed pictures for each sample (figure 5.3) respectively.

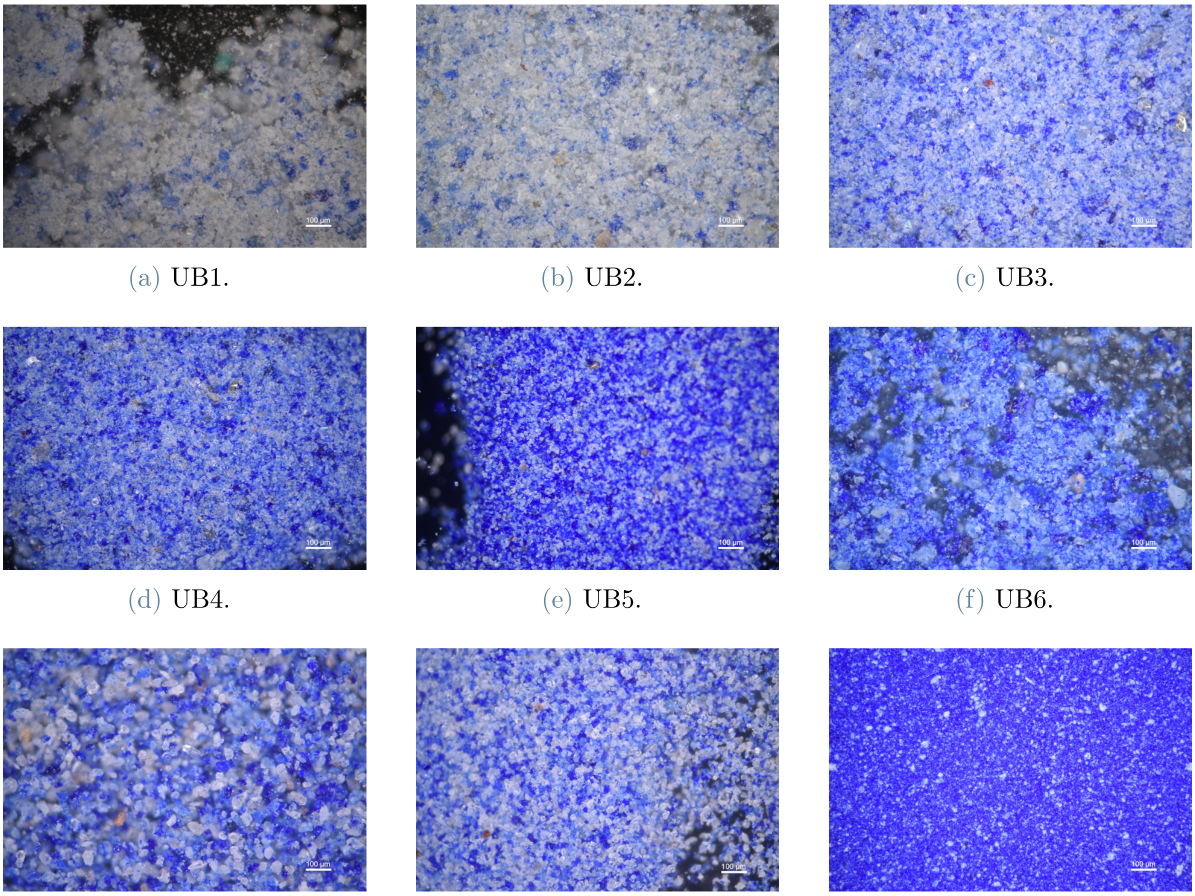

(a) UB1. (b) UB2. (c) UB3.

(d) UB4. (e) UB5. (f) UB6.

(g) UB7. (h) UB8. (i) UB10.

Figure 5.1: All samples observed under a microscope at 10X zoom illuminated with visible light. The scale bar in the bottom right corner of every picture represents 100 µm.

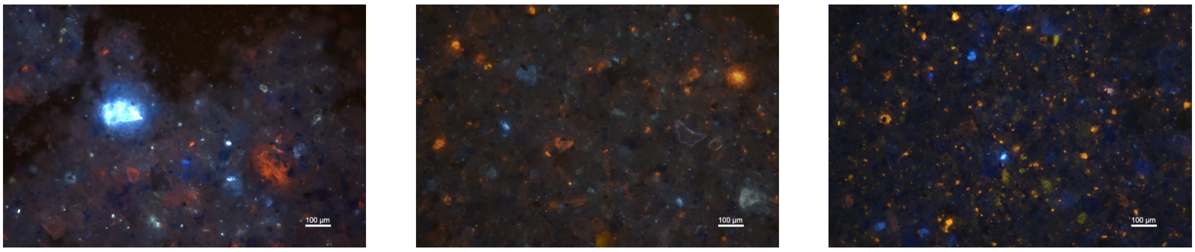
100 µm
100 µm
100 µm

(a) UB1. (b) UB2. (c) UB3.

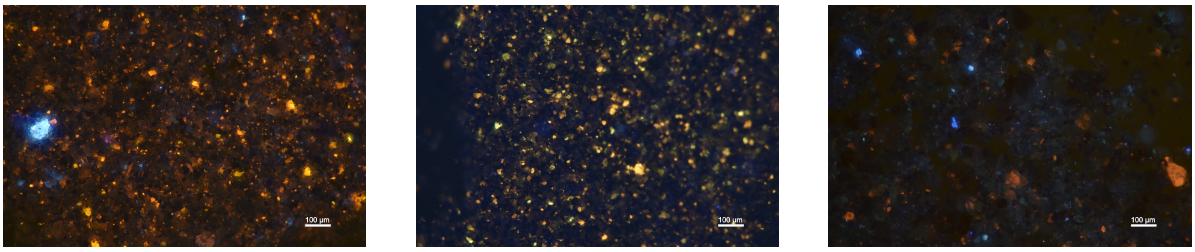
100 µm
100 µm
100 µm

(d) UB4. (e) UB5. (f) UB6.

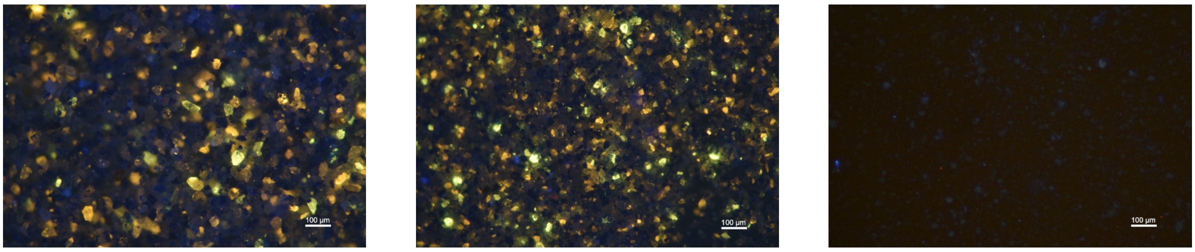
100 µm
100 µm
100 µm

(g) UB7. (h) UB8. (i) UB10.

Figure 5.2: All samples observed under a microscope at 10X zoom illuminated with UV light. The scale bar in the bottom right corner of every picture represents 100 µm.

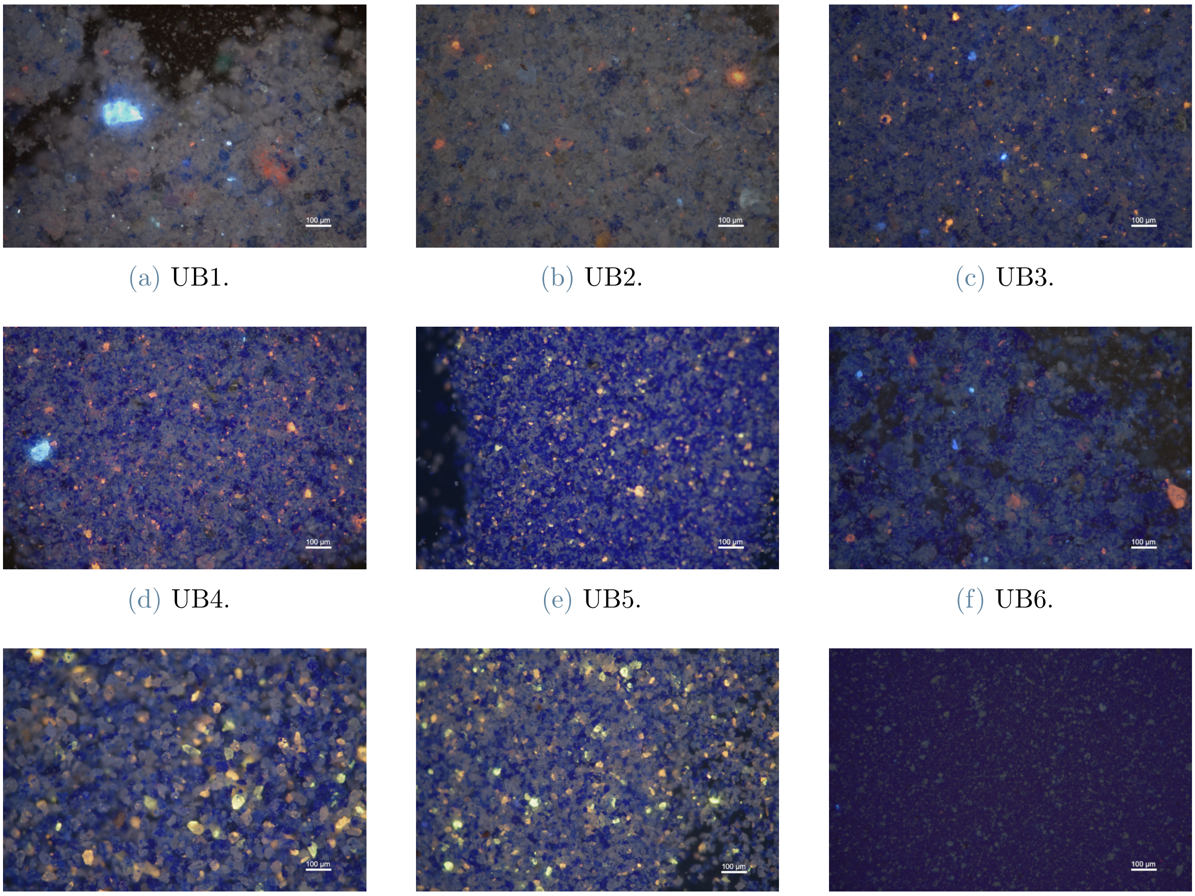

(a) UB1. (b) UB2. (c) UB3.

(d) UB4. (e) UB5. (f) UB6.

(g) UB7. (h) UB8. (i) UB10.

Figure 5.3: Superimposed pictures of all samples observed under a microscope at 10X zoom with visible and under UV light. The scale bar in the bottom right corner of every picture represents 100 µm.

UB1: When observed under UV light, one can notice a variety of fluorescent species glowing white, blue, orange and red.

UB2: Under UV light one can see white, blue, orange and yellow glowing particles.

UB3, UB4, UB5: When observed under UV light, another peculiarity is the decrease of blue-white fluorescent particles. The vast majority fluorescent particles seem to be of the yellow-orange glowing variety.

UB6: Under UV light some fluorescent particles of both the white/blue and yellow/orange variety are visible, although their concentrations seem lower than the other samples.

UB7, UB8: Under UV light they exhibit almost exclusively fluorescent particles of the yellow-orange variety. The lack of other fluorescent species may be attributed to the different geographical origin than the other samples, or to their quality.

UB10: the synthetic pigment presents no fluorescence whatsoever.

Through the analysis of these images it is possible to infer some observations.

- The lower the quality of the pigment, the greater the density of blue-white glowing particles. These appear more prominently in UB1 and UB2, but few can still be found in UB3, UB4 and UB6 as well.
- The higher the quality of the pigment, the greater the proportion of fluorescent particles of the yellow-orange kind. Notably, the Chilean pigments (UB7 and UB8) seemingly present fluorescent particles of this kind only.
- The fluorescence of the pigment doesn't come from the blue colored particles, but from the impurities found in the mineral, which under visible light appear as colorless particles. This consideration is confirmed by the fact that UB10, the artificial pigment, presents no fluorescence whatsoever since the impurities are not synthesized with Guimet's method. Notably, the absence of the impurities can be used to distinguish between natural and synthetic pigments [9, 25, 39].

The last point explains why TRPL, FLIM and TG-HSI measurements have not been performed on UB10.

5.2. TRPL Spectroscopy

5.2.1. Nanoseconds emission

In figures 5.4 and 5.5 the TRPL datasets collected for each sample at the nanosecond scale and after intensity normalization at zero delay are shown. The spectral range is 400-750 nm.

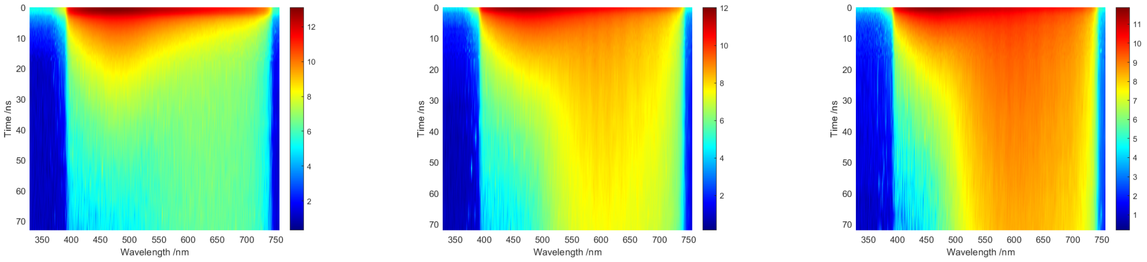

(a) UB1. (b) UB2. (c) UB3.

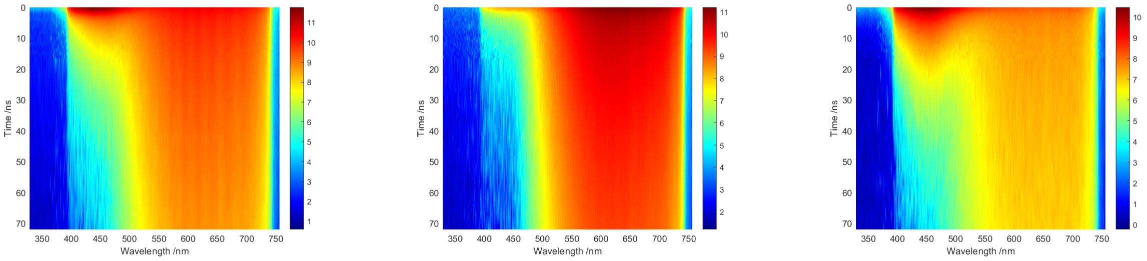

(d) UB4. (e) UB5. (f) UB6.

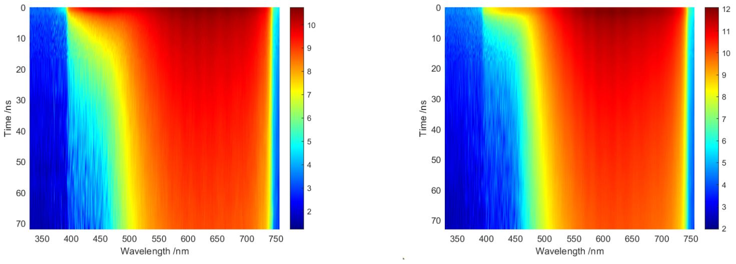

(g) UB7. (h) UB8.

Figure 5.4: TRPL datasets of the nanoseconds emission. Gate: 10 ns; delay range after excitation pulse: 0-70 ns; spectral range: 400-750 nm.

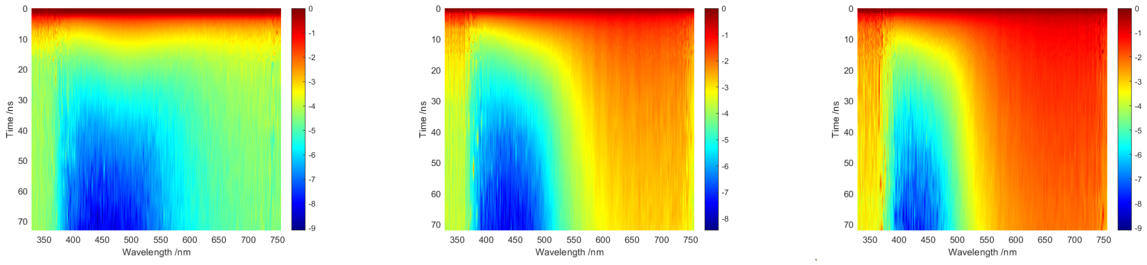

(a) UB1. (b) UB2. (c) UB3.

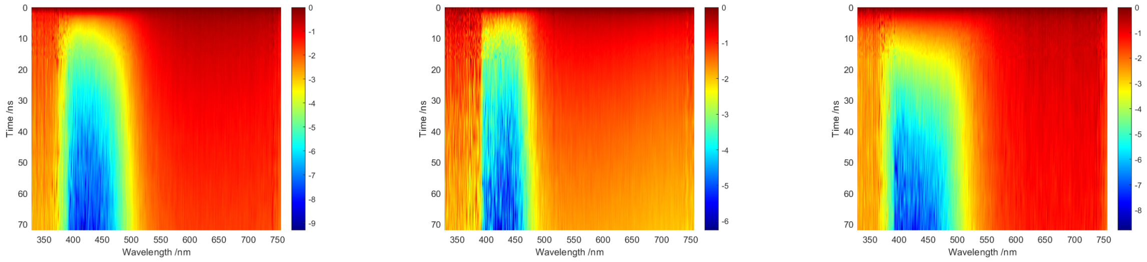

(d) UB4. (e) UB5. (f) UB6.

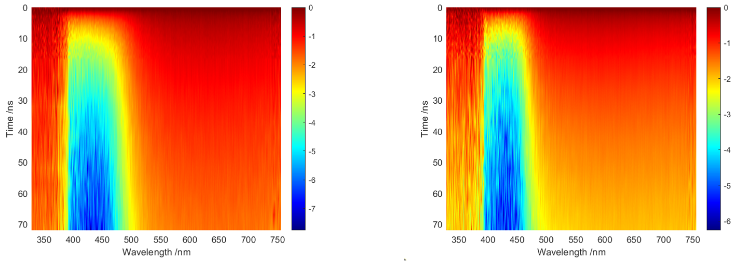

(g) UB7. (h) UB8.

Figure 5.5: TRPL dataset of the nanoseconds emission normalized at t=0 ns. Gate: 10 ns; delay range after excitation pulse: 0-70 ns; spectral range: 400-750 nm.

These TRPL datasets have allowed us to identify two main emission bands with different lifetimes: the 430-460 nm band, corresponding to the aforementioned blue fluorescent particles, which will be referred to as "blue-band" and which presents the shorter lifetime; and the 570-650 nm band, corresponding to the yellow-orange fluorescent particles, referred to as "y/o-band", with the longer lifetime. Depending on the quality of the UB pigment analysed the two emission band display different relative intensity, as detailed in the following. In the samples UB1 through UB4 and UB6, the blue-band is strongest right after the excitation, overshadowing the y/o-band, but it is also the first to fade as time goes on. In UB5, UB7 and UB8, the y/o-band is the strongest band already after excitation. In fact in these last samples, the density of blue emitting fluorescent particles is much lower than that of the yellow-orange emitting particles.

In figures 5.6 and 5.7 the gated emission spectra between 0 and 2 ns and between 30 and 50 ns respectively of all samples are presented. It is clear that, as time goes on, the blue-band (430-460 nm) gradually vanishes, leaving only the y/o-band (570-650 nm).

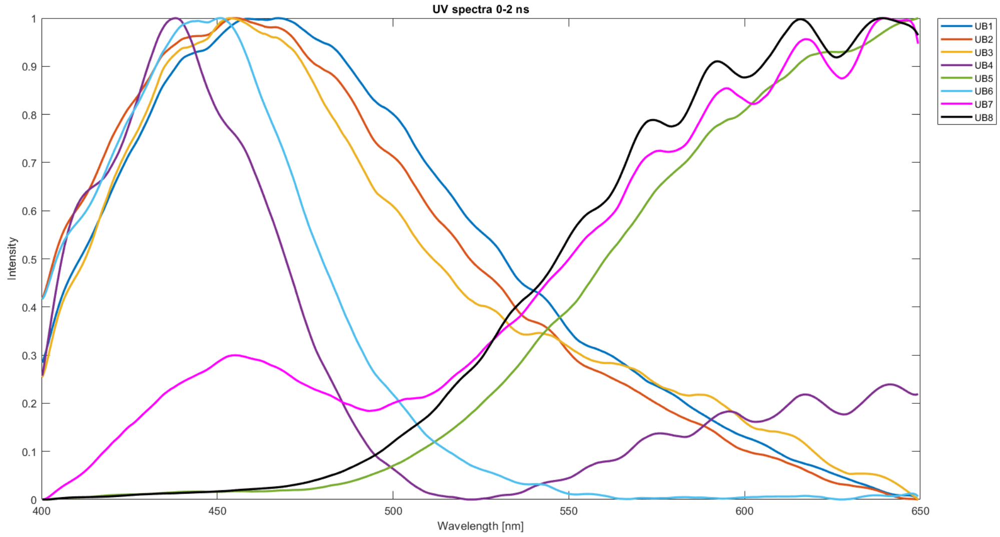

Figure 5.6: Gated spectra of all samples in the time interval 0-2 ns.

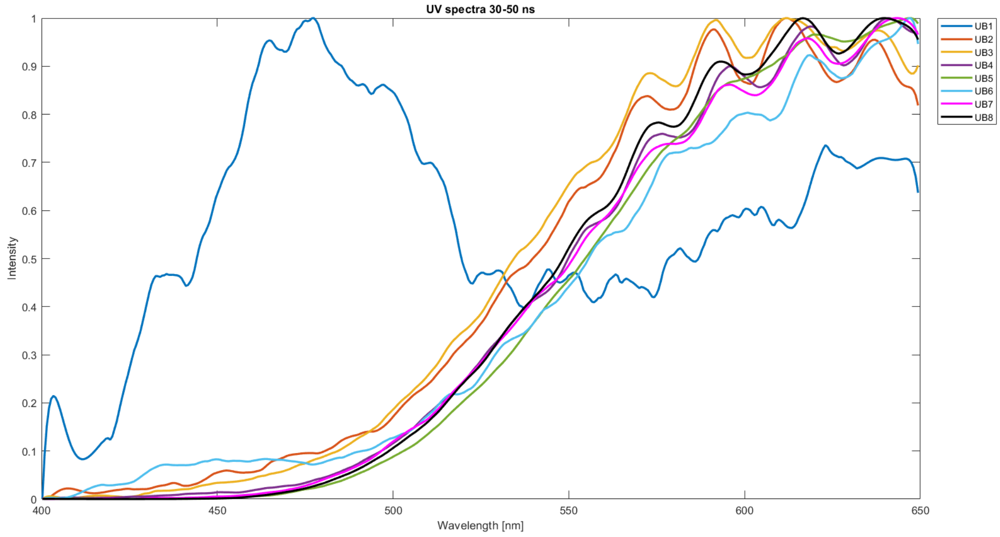

Figure 5.7: Gated spectra of all samples in the time interval 30-50 ns.

In figures 5.8 and 5.9 the measured decays of the blue-band (430-460 nm) and of the y/o-band (570-650 nm) respectively are shown.

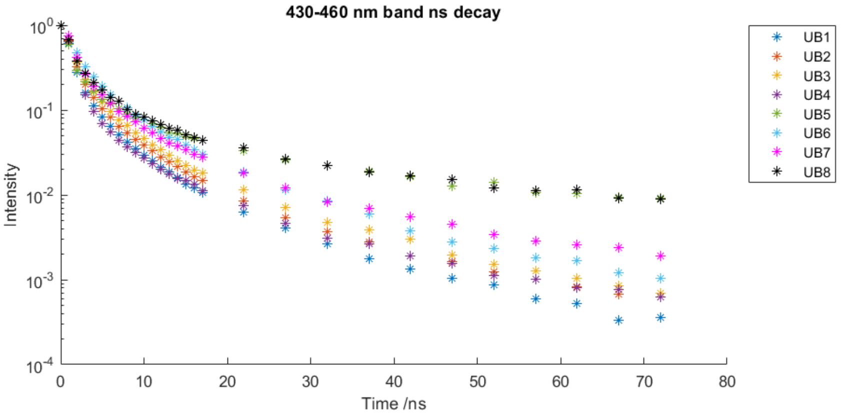

Figure 5.8: Emission decays of the blue-band in all samples.

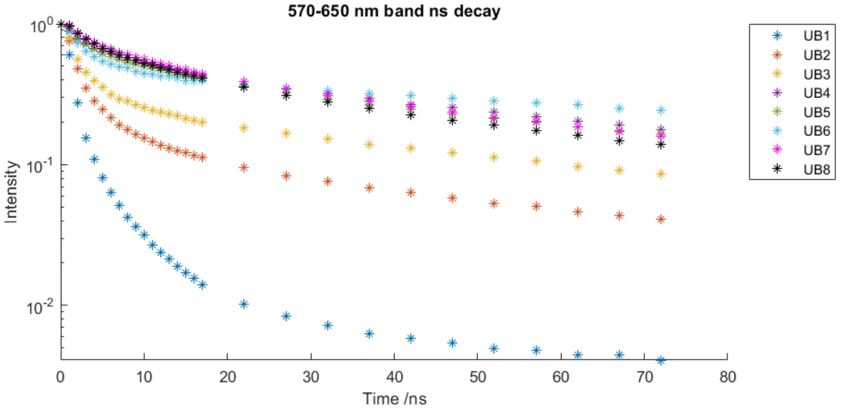

Figure 5.9: Emission decays of the y/o-band in all samples.

We observe that in all samples, 70 ns after excitation, the emission intensity of the blue-band, shown in figure 5.8, has decreased by two orders of magnitude and therefore it can be considered concluded. On the other hand, in all samples except for UB1, the emission intensity of the y/o-band, as shown in figure 5.9, has decreased by just roughly one order of magnitude, thus indicating that the decay kinetics of this band do not end at this timescale and are to be followed at longer delays, as will be done in the next section.

In table 5.1 we report the effective lifetimes τ_{eff} calculated by modelling the decay kinetic as a tri-exponential function. We underline that the emission lifetime reconstructed for the y/o-band is not indicative of the real emission lifetime of this band because it has been computed from an incomplete decay. This value is nonetheless useful to show that the y/o-band is characterized by a longer lifetime than the blue-band in all samples.

τ_{eff} **of the nanoseconds emission for each sample [ns]**								
	UB1	**UB2**	**UB3**	**UB4**	**UB5**	**UB6**	**UB7**	**UB8**
blue-band	2.39	2.88	3.22	2.38	9.04	4.36	4.13	8.62
y/o-band	6.31	35.75	37.42	74.39	45.72	91.64	44.66	40.30

Table 5.1: Table with the nanoseconds emission effective lifetime calculated for each band of all samples.

5.2.2. Microseconds emission

In figures 5.10 and 5.11 the TRPL datasets collected for each sample at the microseconds scale and after intensity normalization at zero delay respectively are shown. The spectral range has been changed from 400-750 nm to 500-800 nm.

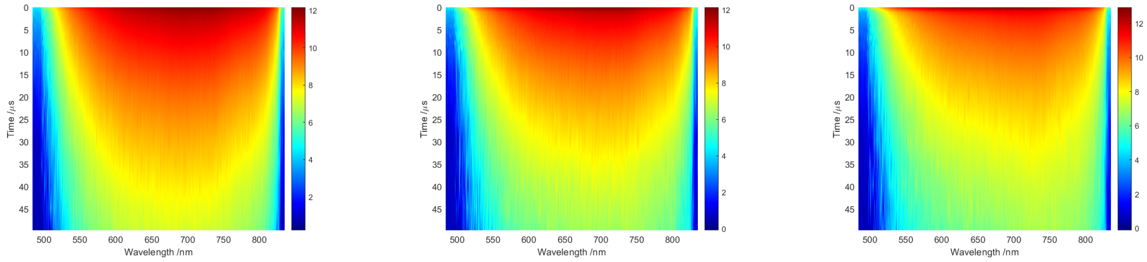

(a) UB1. (b) UB2. (c) UB3.

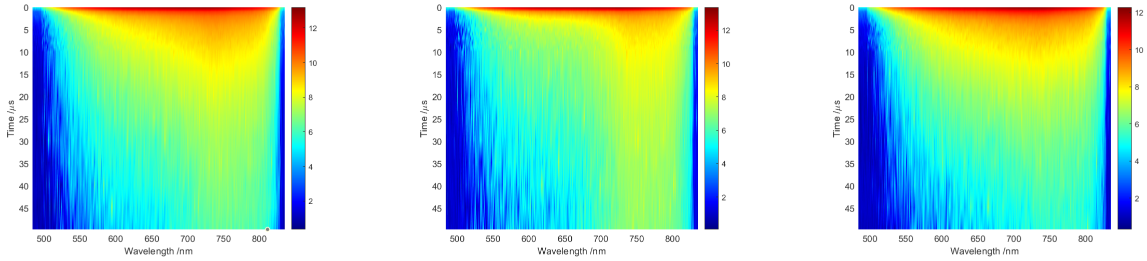

(d) UB4. (e) UB5. (f) UB6.

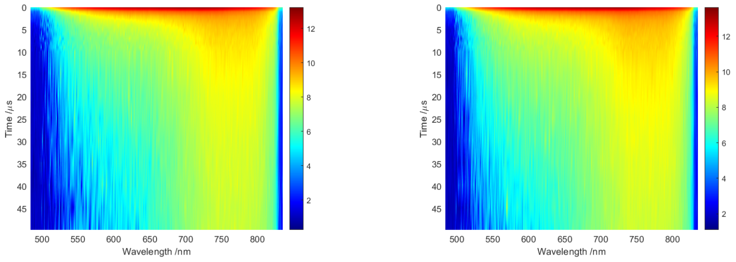

(g) UB7. (h) UB8.

Figure 5.10: TRPL dataset of the microseconds emission. Gate: 1 µs; delay range after excitation pulse: 0-50 µs; spectral range: 500-850 nm.

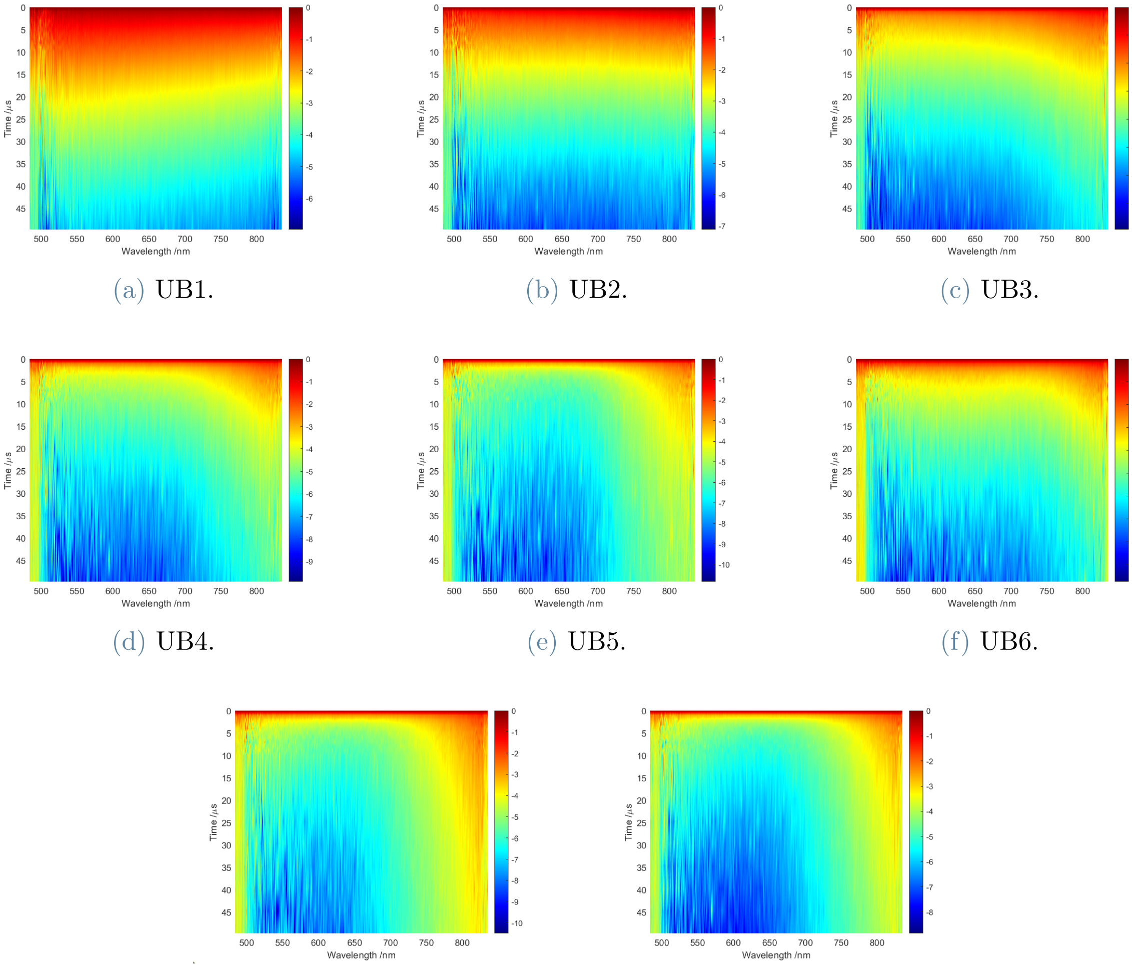

(a) UB1.

(b) UB2.

(c) UB3.

(d) UB4.

(e) UB5.

(f) UB6.

(g) UB7.

(h) UB8.

Figure 5.11: TRPL dataset of the microseconds emission normalized at t=0 µs. Gate: 1 µs; delay range after excitation pulse: 0-50 µs; spectral range: 500-850 nm.

These measurements were performed to better observe the temporal evolution of the y/o-band. In samples UB3 through UB8 we also noticed the emergence of a further band in the 720-800 nm spectral range, which will be referred to as "IR-band". In figures 5.12 and 5.13 the gated emission spectra between 0 and 2 µs and between 30 and 50 µs respectively of all samples are presented.

Figures 5.14 and 5.15 show the measured decay of the y/o-band and the IR-band respectively.

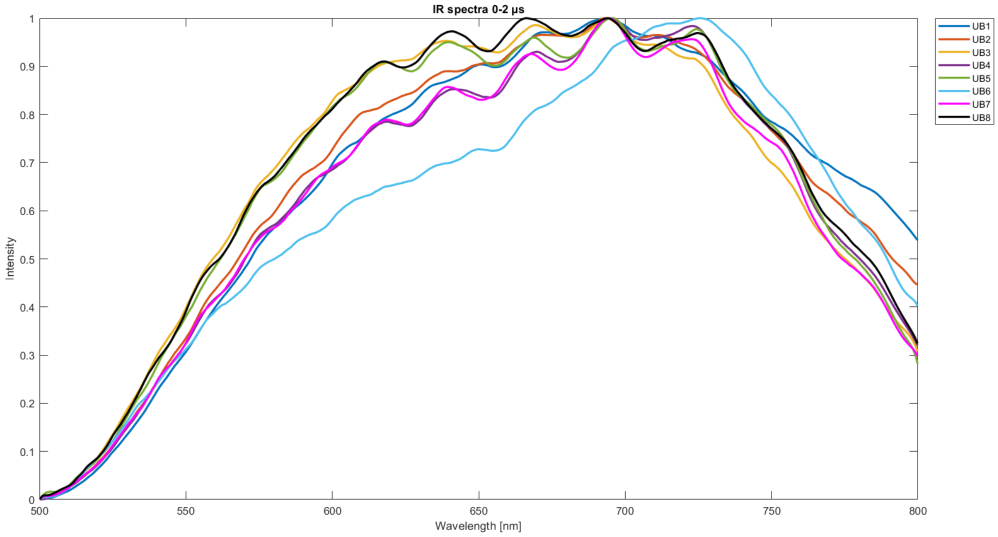

Figure 5.12: Gated spectra of all samples in the time interval 0-2 µs.

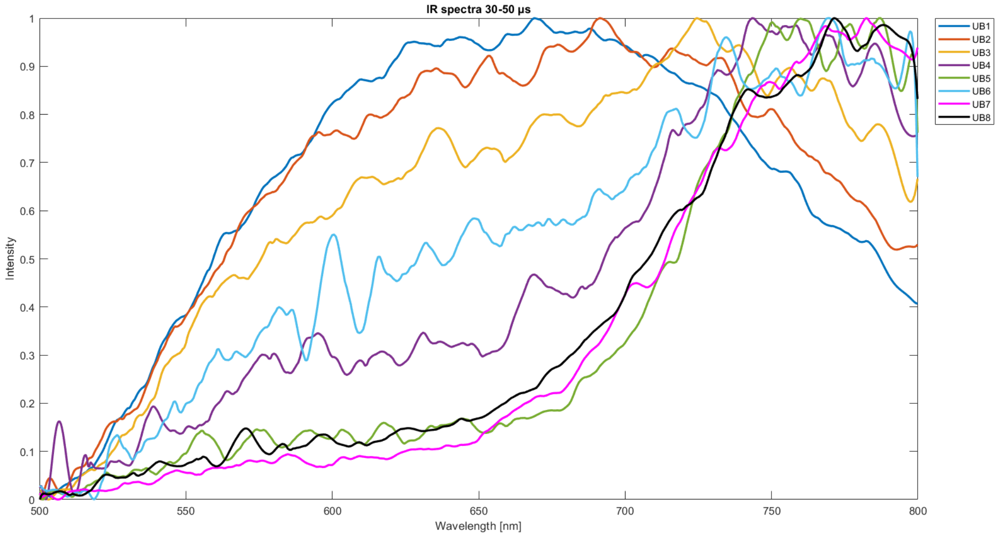

Figure 5.13: Gated spectra of all samples in the time interval 30-50 µs.

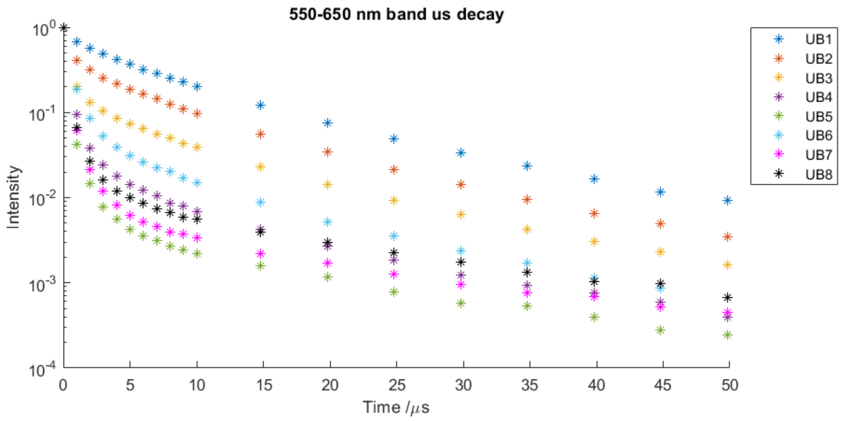

Figure 5.14: Emission decays of the y/o-band in all samples.

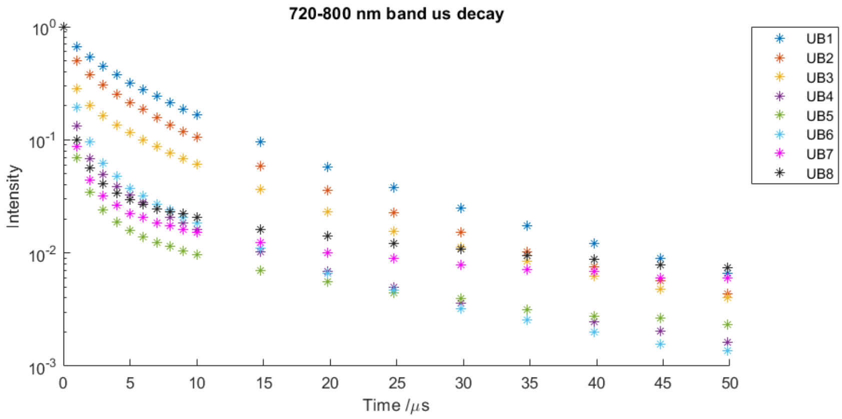

Figure 5.15: Emission decays of the IR-band in all samples.

In table 5.2 we report effective lifetimes of the y/o-band and IR-band in all samples calculated by fitting the emission decay with a bi-exponential function. Interestingly, except for UB1 and UB2, the IR-band shows significantly longer lifetime than the y/o-band. Moreover, the Chilean samples, UB7 and UB8, show the longest living IR-bands. To better study the features of the IR emission band, we have decided to perform another TRPL measurement at the tens of microseconds temporal scale on the higher quality pigments (therefore excluding UB1 and UB2).

τ_{eff} of the microseconds emission for each sample [µs]								
	UB1	**UB2**	**UB3**	**UB4**	**UB5**	**UB6**	**UB7**	**UB8**
y/o-band	9.61	7.47	5.91	2.08	1.23	3.24	1.75	2.42
IR-band	8.70	7.45	7.54	4.04	5.30	3.83	11.21	11.11

Table 5.2: Table with the microseconds emission effective lifetime calculated for each band of all samples.

To compare the relative intensity of different bands in the various samples, the total intensity of each band has been calculated by summing all the counts in a selected time window: 0-10 ns for the blue-band and 0-50 µs for both the y/o band. The results are reported below.

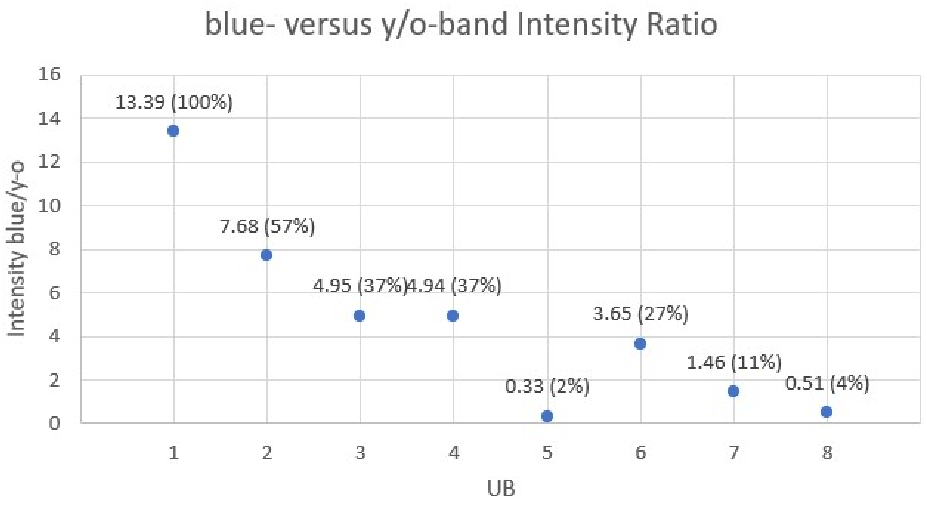

Figure 5.16: Relative intensity of the blue-band with respect to the y/o-band. The tag above each point reads the ratio computed by summing all counts in the chosen time window (0-10 ns for the blue-band and 0-50 µs for the y/o-band) and in parentheses the percentage of the relative intensity of the sample with respect to that of UB1.

Interestingly we see that the lower the quality of the pigment, the higher the relative intensity of the blue-band with respect to the y/o band.

5.2.3. Tens of microseconds emission

As mentioned in the previous section, samples UB3 through UB8 exhibit a persistent IR-band (720-800 nm) at delays of 50 µs after the excitation pulse. Here we further explore this emission from 0 to 200 µs after the excitation pulse, in the spectral range 500-850 nm.

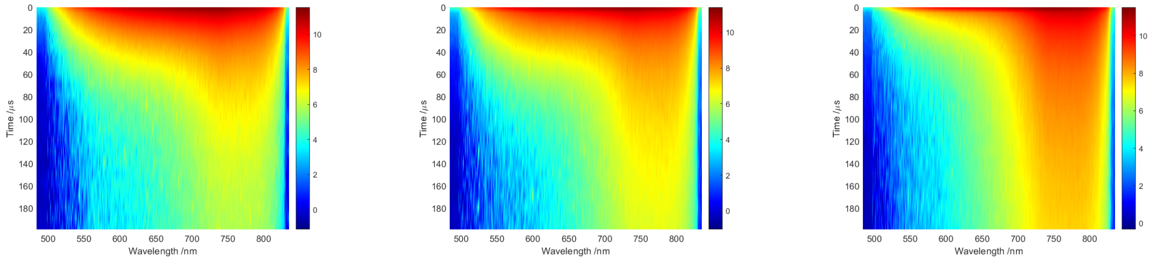

(a) UB3. (b) UB4. (c) UB5.

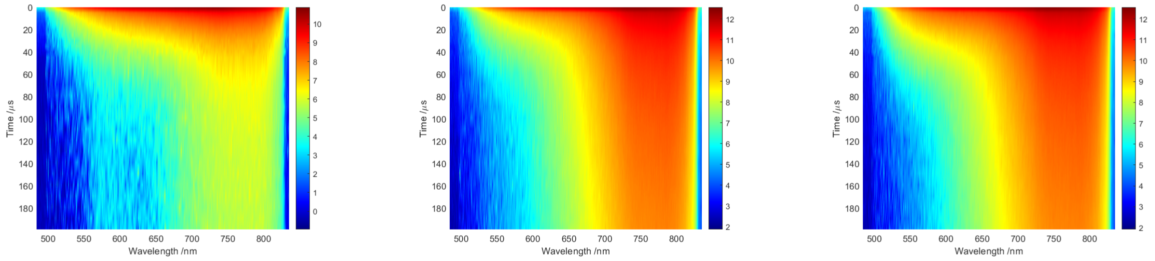

(d) UB6. (e) UB7. (f) UB8.

Figure 5.17: TRPL dataset of the tens of microseconds emission. Gate: 10 µs; delay range after excitation pulse: 0-200 µs; spectral range: 500-850 nm.

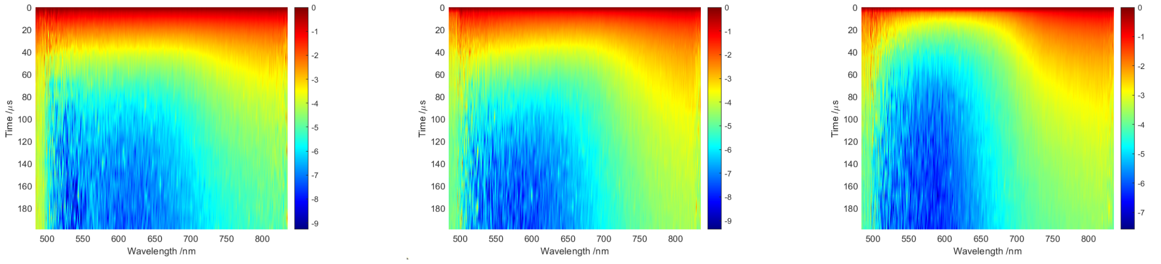

(a) UB3. (b) UB4. (c) UB5.

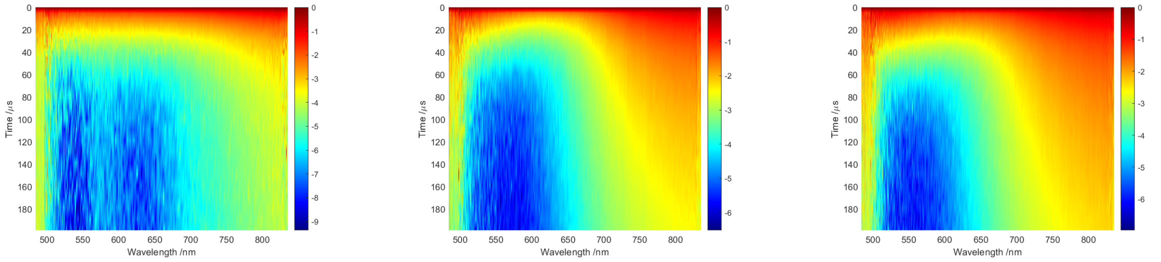

(d) UB6. (e) UB7. (f) UB8.

Figure 5.18: TRPL dataset of the tens of microseconds emission normalized at t=0 μs. Gate: 10 μs; delay range after excitation pulse: 0-200 μs; spectral range: 500-850 nm.

In figures 5.19 and 5.20 we show the gated spectra between 30 and 50 μs and between 110 and 140 μs. It is once again clear that as time goes on, the emission shifts towards longer wavelengths.

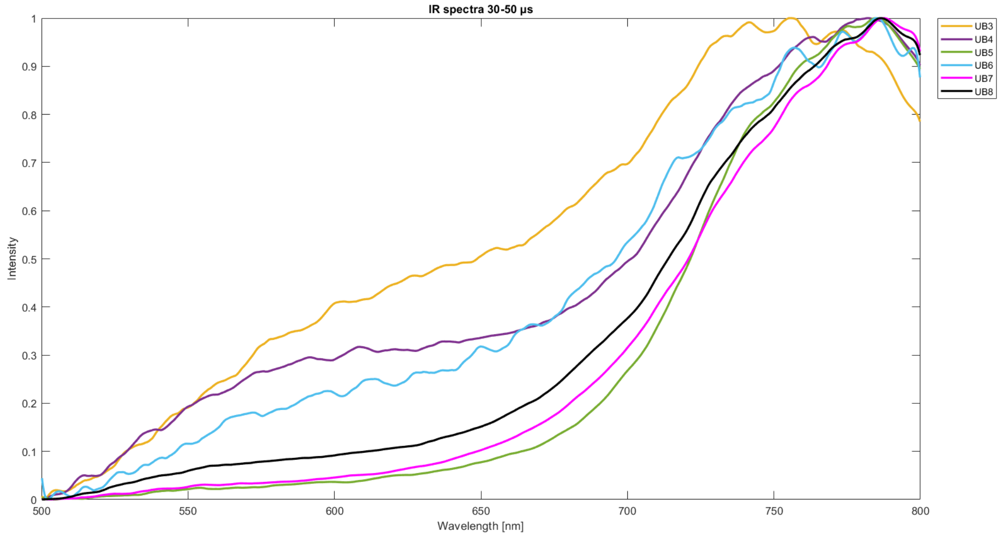

Figure 5.19: Gated spectra of all samples in the time interval 30-50 µs.

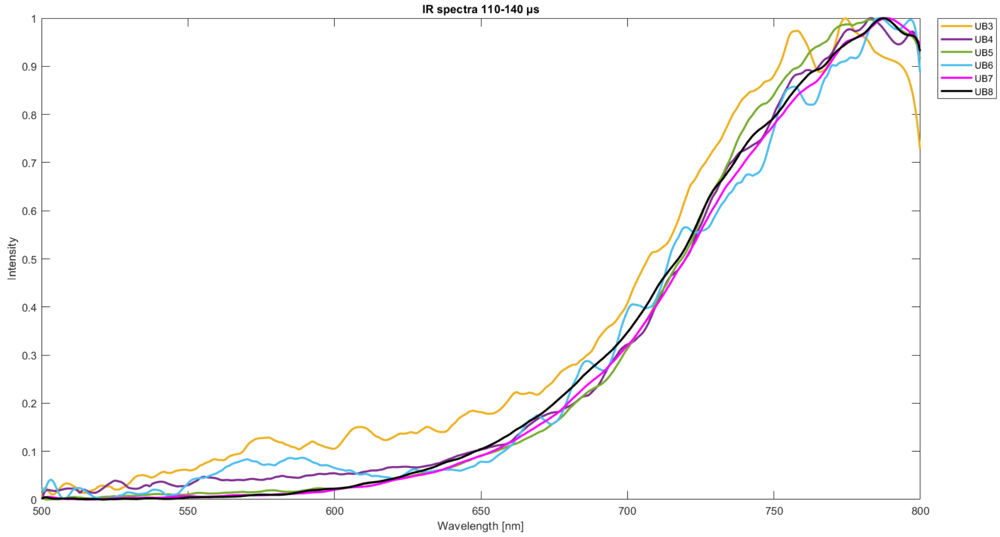

Figure 5.20: Gated spectra of all samples in the time interval 110-140 µs.

In figure 5.21 we report the measured decays of the IR-band and in table 5.3 the lifetime constants calculated by fitting the decay kinetics with a bi-exponential model.

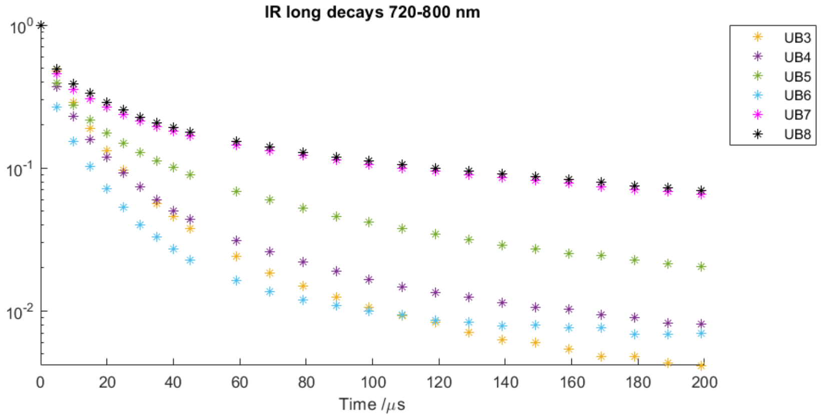

Figure 5.21: Emission decays of the IR-band in the tens of microseconds timescale.

τ_{eff} of the tens of microseconds emission [µs]						
	UB3	**UB4**	**UB5**	**UB6**	**UB7**	**UB8**
IR-band	20.40	26.57	44.23	20.75	91.55	91.55

Table 5.3: Table with the tens of microseconds emission effective lifetime calculated for the IR-band.

At this point we can calculate the relative intensity of the y/o-band with respect to the IR-band. The counts were summed for both bands from 0 to 50 µs and the resulting relative intensities are reported below.

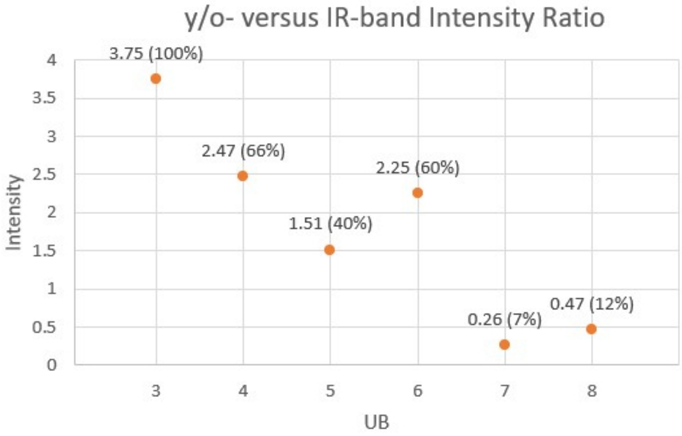

Figure 5.22: Relative intensity of the y/o-band with respect to the IR-band. The tag above each point reads the ratio computed by summing all counts in the chosen time window (0-50 µs for the both bands) and in parentheses the percentage of the relative intensity of the sample with respect to that of UB3.

Interestingly we see that the greater the quality of the pigment, the weaker the y/o-band gets. The Chilean pigments, UB7 and UB8, show that the IR band is more intense than the y/o band.

5.3. Time-Gated methods: TG-HSI and FLIM

In figures 5.23, 5.24 and 5.25 we show the TG-HSI pictures of the fluorescent emission of all samples* at the nanosecond, microsecond and tens of microseconds timescales respectively. The pictures are colorized according to the measured spectra.

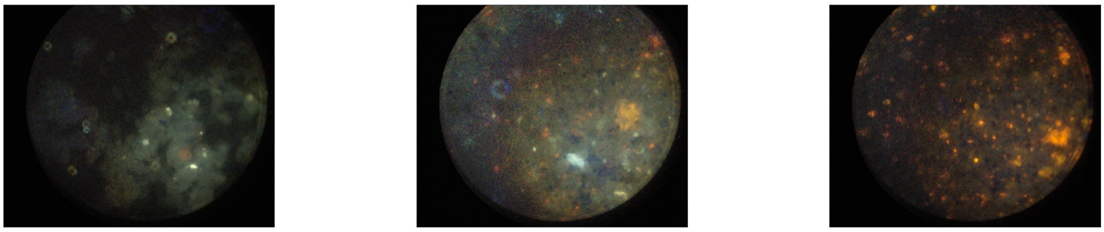

(a) UB1. (b) UB2. (c) UB3.

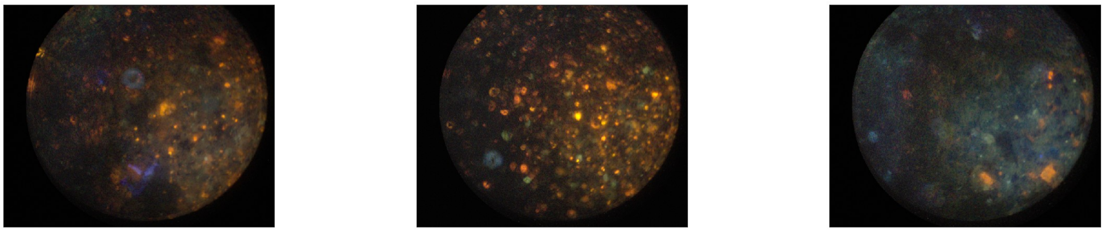

(d) UB4. (e) UB5. (f) UB6.

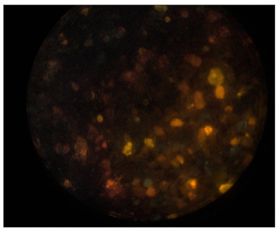

(g) UB7.

Figure 5.23: TG-HSI measurements of the nanoseconds emission. Gate: 100 ns; delay: 0 ns after excitation.

---

[*] We notify that UB8 has been excluded from the TG-HSI measurement since under any test conducted it showed the exact same behavior as UB7. We remind that they are in fact the same pigment, differing only in particle size.

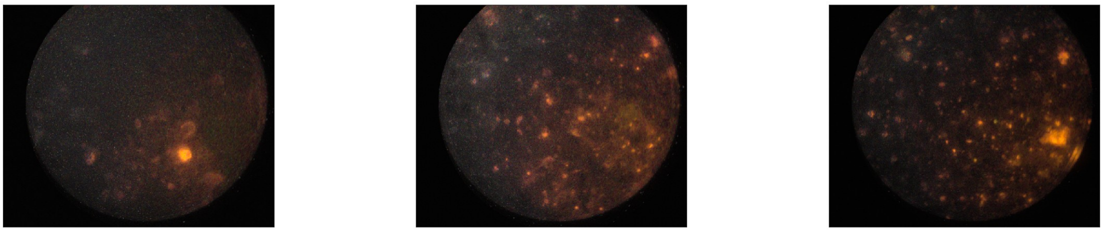

(a) UB1. (b) UB2. (c) UB3.

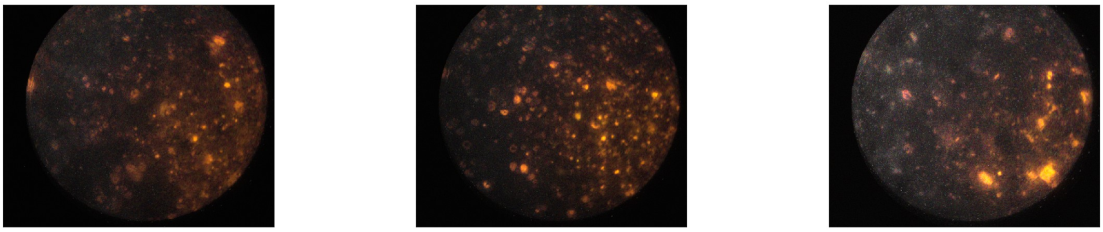

(d) UB4. (e) UB5. (f) UB6.

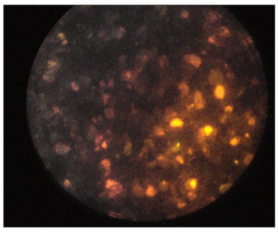

(g) UB7.

Figure 5.24: TG-HSI measurements of the microseconds emission. Gate: 1 µs; delay: 0.155 µs after excitation.

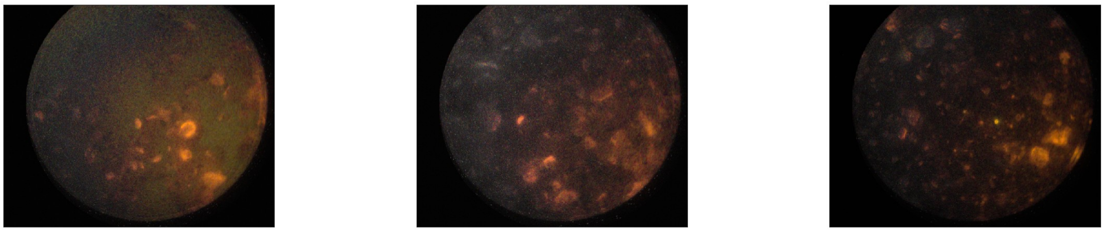

(a) UB1. (b) UB2. (c) UB3.

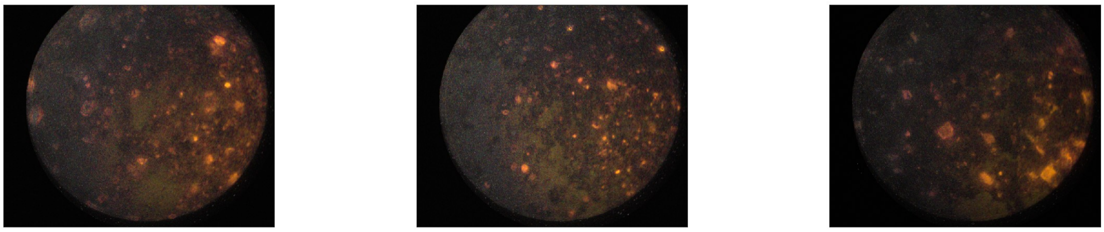

(d) UB4. (e) UB5. (f) UB6.

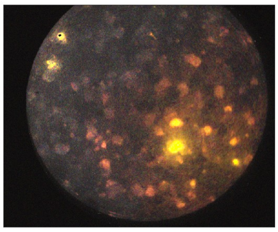

(g) UB7.

Figure 5.25: TG-HSI measurements of the tens of microseconds emission. Gate: 10 µs; delay: 1 µs after excitation.

Notably, with the TG-HSI and FLIM setups we have not been able to detect the IR-band emission. We know from TRPL measurements that this band has decay kinetics with lifetime in the order of tens of microseconds. With the employed imaging setups we have observed a background emission due to the optics in the excitation path, also occurring at the tens of microseconds timescale, which completely masks the IR emission.

In the following sections we will present the TG-HSI and FLIM measurements of a selection of the most emblematic samples: UB2, which is the byproduct of Cennini's method and should present the highest number of impurities; UB5, which is the highest quality among natural pigments; and UB7, the Chilean pigment with the greatest particle size.

5.3.1. UB2

UB2: TG-HSI.

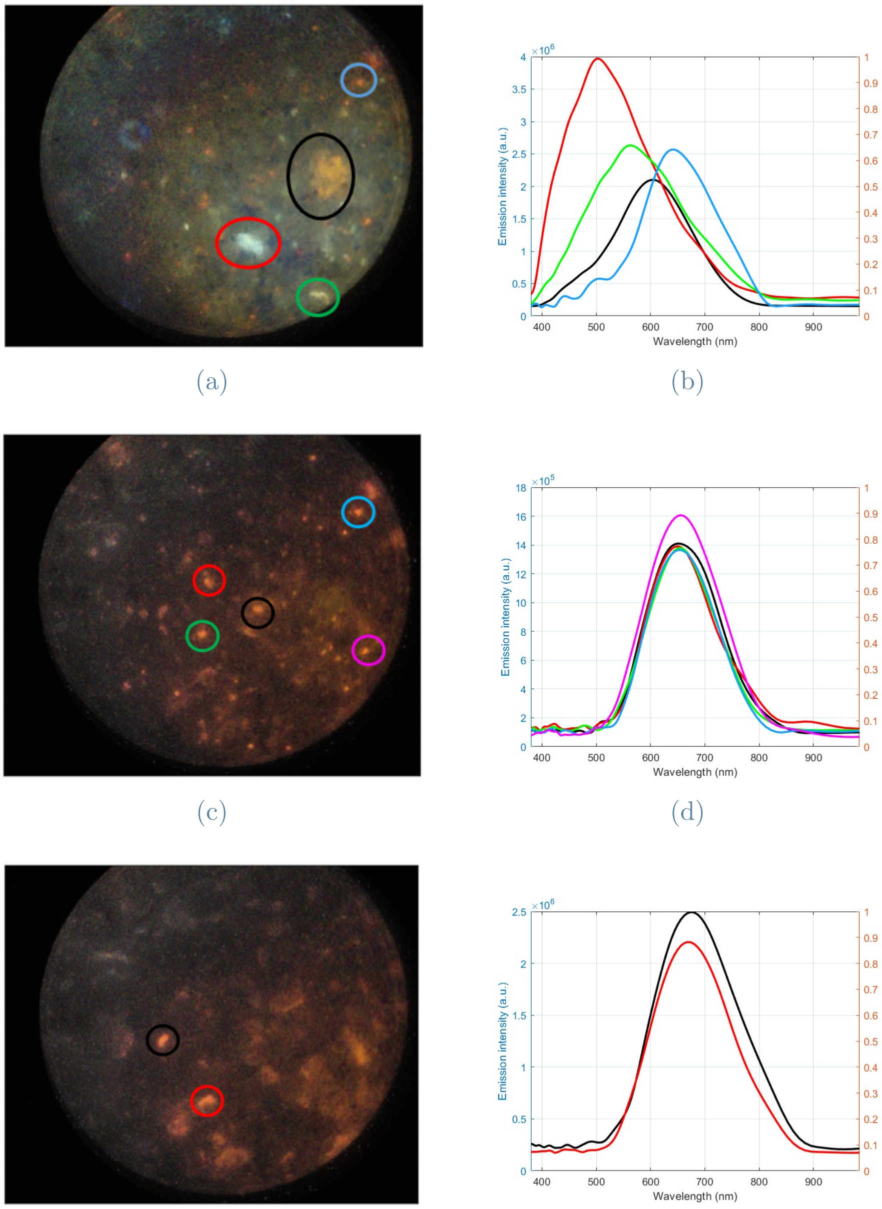

(a) (b)

(c) (d)

(e) (f)

Figure 5.26: (LEFT) Maps of the ROI of UB2 colorized according to the measured spectra. The circled particles are the ones whose spectrum is being shown in the corresponding colors in the plots on the right. (RIGHT) Spectra of the circled particles in the corresponding color. a,b) Map and spectra of the nanoseconds emission (gate: 100 ns; delay after excitation: 0 ns). c,d) Map and spectra of the microseconds emission (gate: 1 µs; delay after excitation: 0.15 µs). e,f) Map and spectra of the tens of microseconds emission (gate: 10 µs; delay after excitation: 1 µs).

UB2: FLIM, nanoseconds emission.

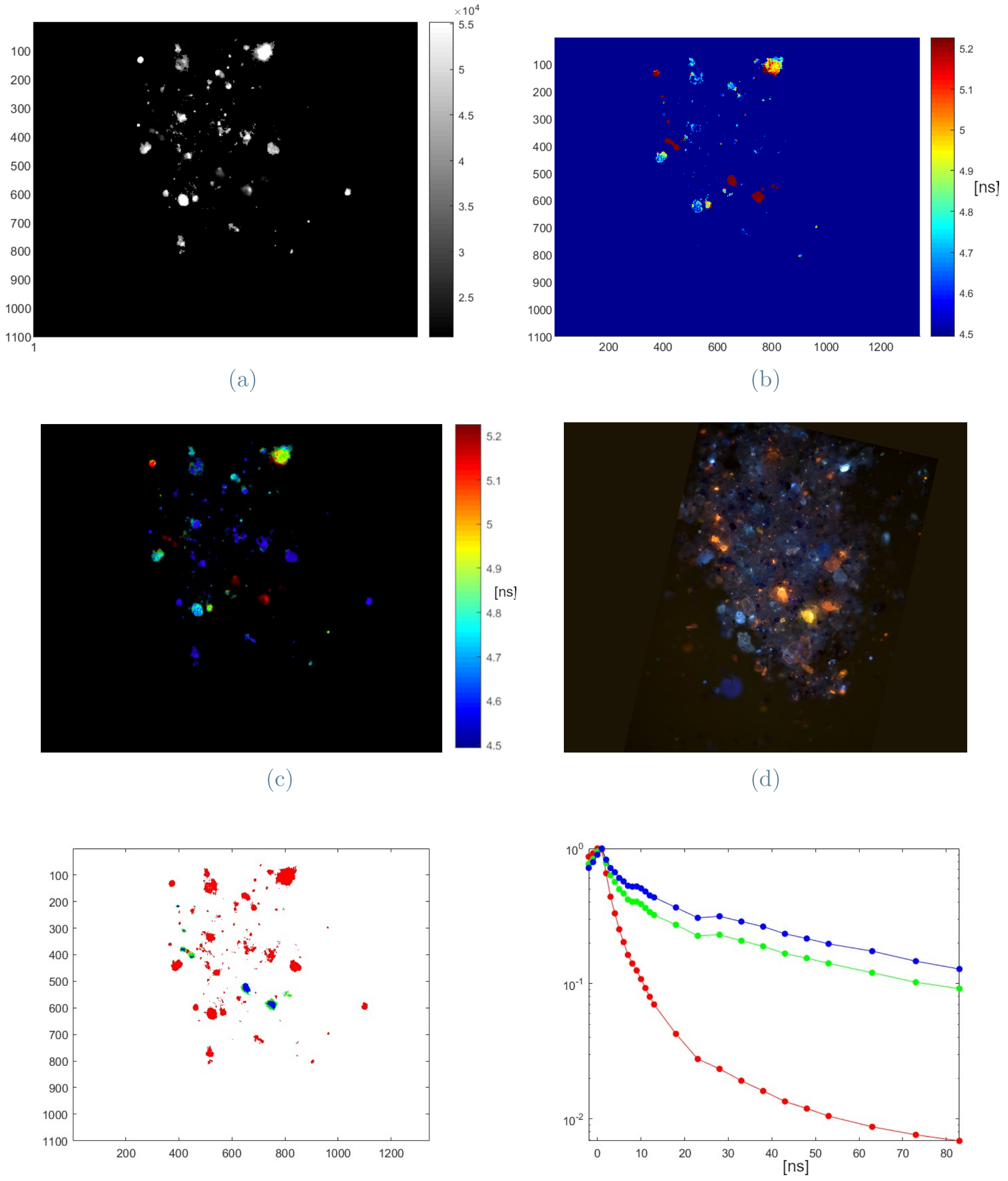

(a) (b)

(c) (d)

(e) (f)

Figure 5.27: FLIM measurement of UB2 at nanosecond timescale (gate: 10 ns; delay range after excitation: 0-100 ns). a) Intensity map of the ROI. b) Lifetime map of the ROI. c) HSV map of the ROI. The different colors of the pixels represent different lifetimes. d) Color picture of the ROI of the sample taken with a microscope at 15X zoom, illuminated with UV light. e) Clusters identified. f) Decay kinetics of the clusters.

UB2: FLIM, microseconds emission.

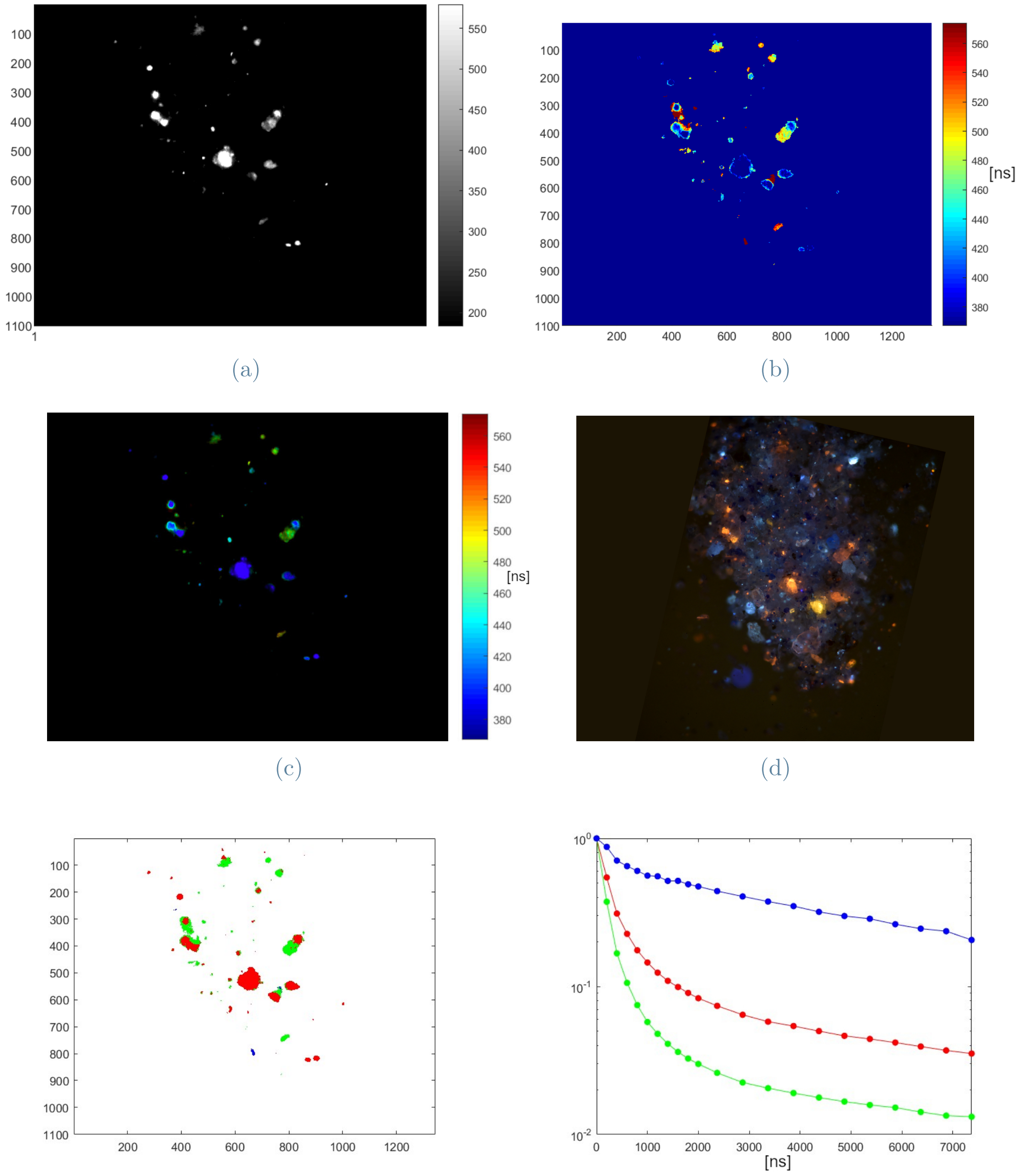

(a) (b)

(c) (d)

(e) (f)

Figure 5.28: FLIM measurement of UB2 at microseconds timescale (gate: 1 µs; delay range after excitation: 0.15-20 µs). a) Intensity map of the ROI. b) Lifetime map of the ROI. c) HSV map of the ROI. The different colors of the pixels represent different lifetimes. d) Color picture of the ROI of the sample taken with a microscope at 15X zoom, illuminated with UV light. e) Clusters identified. f) Decay kinetics of the clusters.

In the nanoseconds emission picture of the ROI in the TG-HSI measures (figure 5.26a) a multitude of both blue and yellow-orange fluorescent particles can be seen. The particle circled in red is the strongest emitter and its spectrum peaks at around 500 nm. As previously mentioned, the low intensity blue tone that pervades the field of view is probably due to out of focus blue emitters. In figure 5.26c, which refers to the microseconds emission, the short-living blue fluorescent particles have disappeared. Interestingly, the particle circled in black in the previously described figure, which belongs to the yellow-orange emitting kind, exhibits a greatly reduced emission that is almost indistinguishable from the background, suggesting that, although it belongs to the long lived emission group, it presents a lower lifetime than its peers. In this picture one can notice a multitude of smaller, relatively intense yellow-orange fluorescent particles, all emitting with a peak at around 650 nm. At the tens of microseconds timescale (figure 5.26e) almost all fluorescent emission has extinguished. There are few particles that stand out from the background and their spectra peak at around 670 nm, possibly indicating that the longer the lifetime of the particle, the longer the wavelength of its fluorescent emission.

The FLIM measurements correctly separates emitters with radically different lifetimes, which in our case are the blue fluorescent particles and the yellow or orange fluorescent particles. From the nanosecond measure we notice that the blue emission is much more intense than the yellow-orange emission. This means that only few particles of this last type emit strongly enough to be detected when they do, they show up as having the longest lifetimes. In the microsecond measure, on the other hand, only the yellow-orange fluorescent particles appear, as to be expected.

5.3.2. UB5

UB5: TG-HSI.

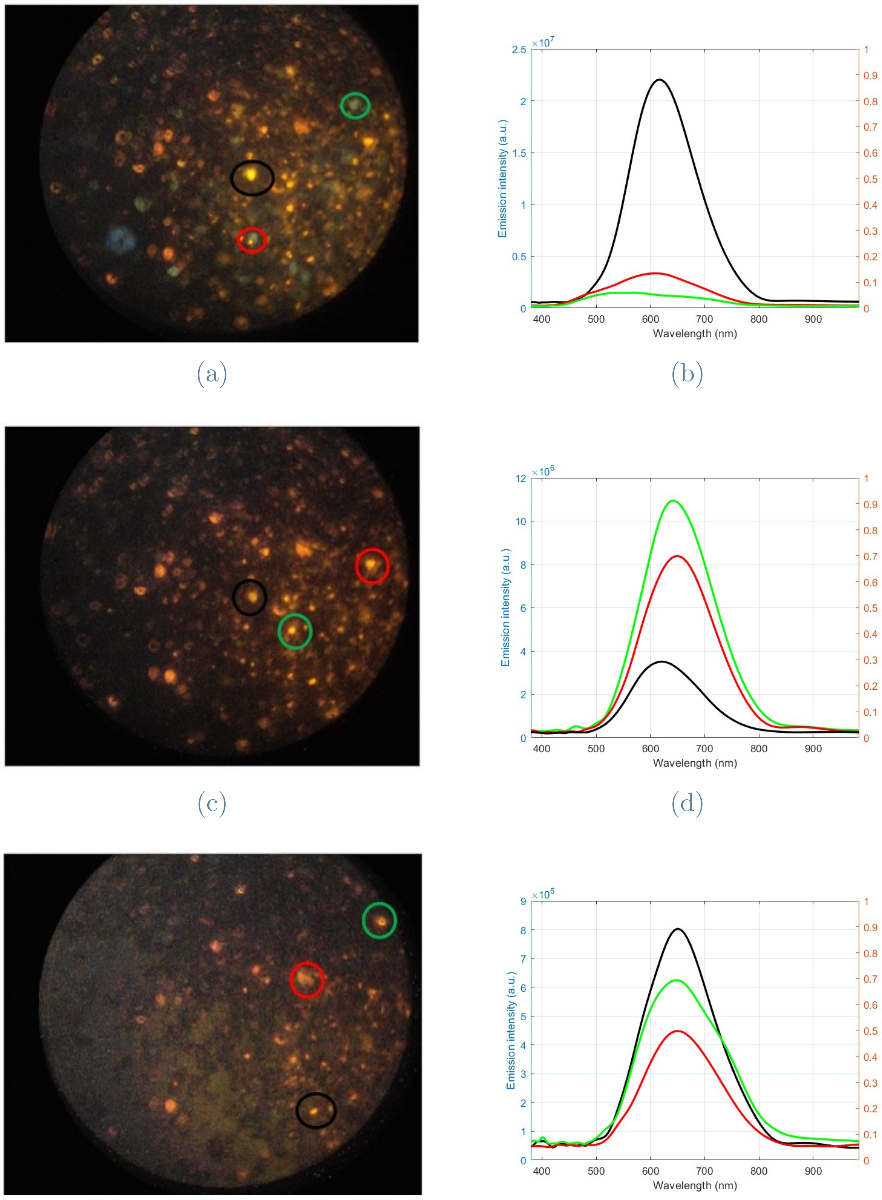

(a) (b)

(c) (d)

(e) (f)

Figure 5.29: (LEFT) Maps of the ROI of UB5 colorized according to the measured spectra. The circled particles are the ones whose spectrum is being shown in the corresponding colors in the plots on the right. (RIGHT) Spectra of the circled particles in the corresponding color. a,b) Map and spectra of the nanoseconds emission (gate: 100 ns; delay after excitation: 0 ns). c,d) Map and spectra of the microseconds emission (gate: 1 µs; delay after excitation: 0.15 µs). e,f) Map and spectra of the tens of microseconds emission (gate: 10 µs; delay after excitation: 1 µs).

UB5: FLIM, nanoseconds emission.

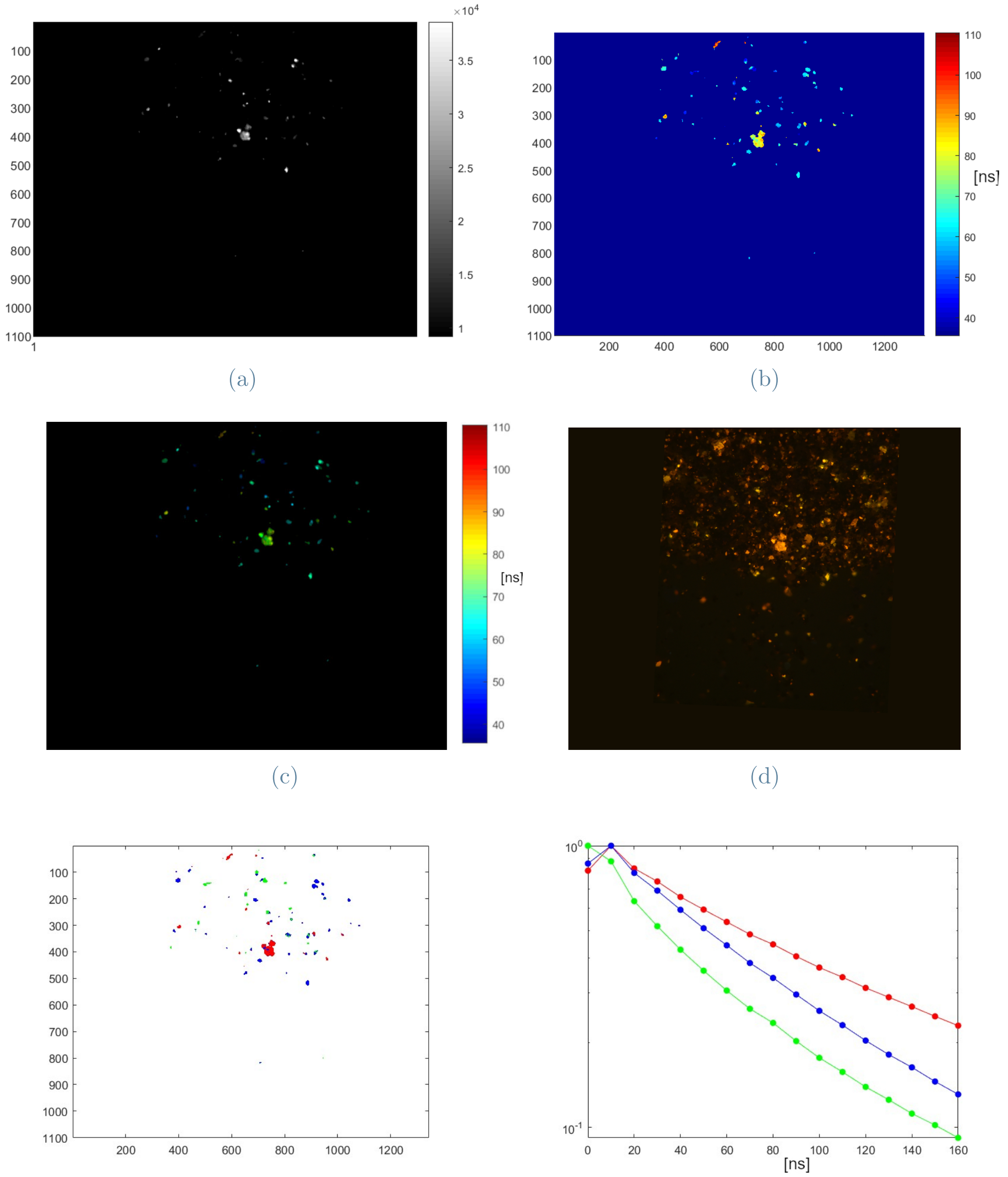

(a) (b) (c) (d) (e) (f)

Figure 5.30: FLIM measurement of UB5 at nanosecond timescale (gate: 10 ns; delay range after excitation: 0-100 ns). a) Intensity map of the ROI. b) Lifetime map of the ROI. c) HSV map of the ROI. The different colors of the pixels represent different lifetimes. d) Color picture of the ROI of the sample taken with a microscope at 15X zoom, illuminated with UV light. e) Clusters identified. f) Decay kinetics of the clusters.

UB5: FLIM, microseconds emission.

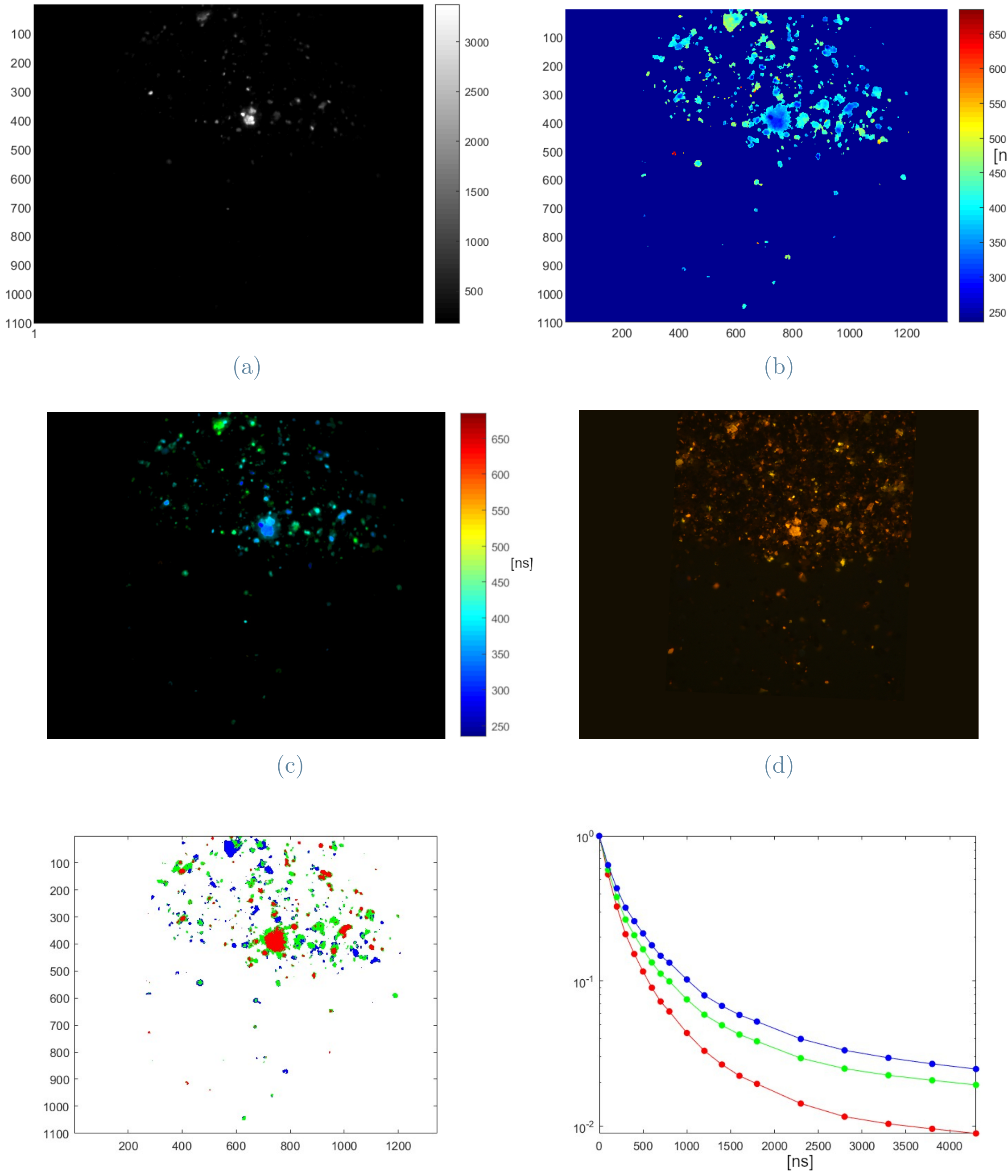

(a) (b) (c) (d) (e) (f)

Figure 5.31: FLIM measurement of UB5 at microseconds timescale (gate: 1 µs; delay range after excitation: 0.15-20 µs). a) Intensity map of the ROI. b) Lifetime map of the ROI. c) HSV map of the ROI. The different colors of the pixels represent different lifetimes. d) Color picture of the ROI of the sample taken with a microscope at 15X zoom, illuminated with UV light. e) Clusters identified. f) Decay kinetics of the clusters.

The fluorescent landscape of UB5 is dominated by small particles of the yellow-orange emitting kind. The nanosecond measure (figures 5.29a and 5.29b) reveals that there are some particles that show a peculiar spectrum, like the particle circled in green in figure 5.29a. This particle presents a weak and broad spectrum from 500 nm to 700 nm. This is probably due to there being at least two components: a shorter-wavelengths one, peaking at around 520 nm and a longer-wavelengths one, peaking at around 600 nm. One explanation could be that the first component would come from the actual spectrum of that particle, which would then be of the blue fluorescent kind, while the second component would come from out of focus yellow-orange emitters.

From the FLIM measurements we see that the emitting particles do not change much as we go from nano- to microseconds. These results confirm the previous TRPL measurements (as shown in figure 5.4e), in which we saw that in UB5 the yellow-orange fluorescent band was the most intense even right after the excitation pulse and that almost no trace of the blue band could be seen.

5.3.3. UB7

UB7: TG-HSI

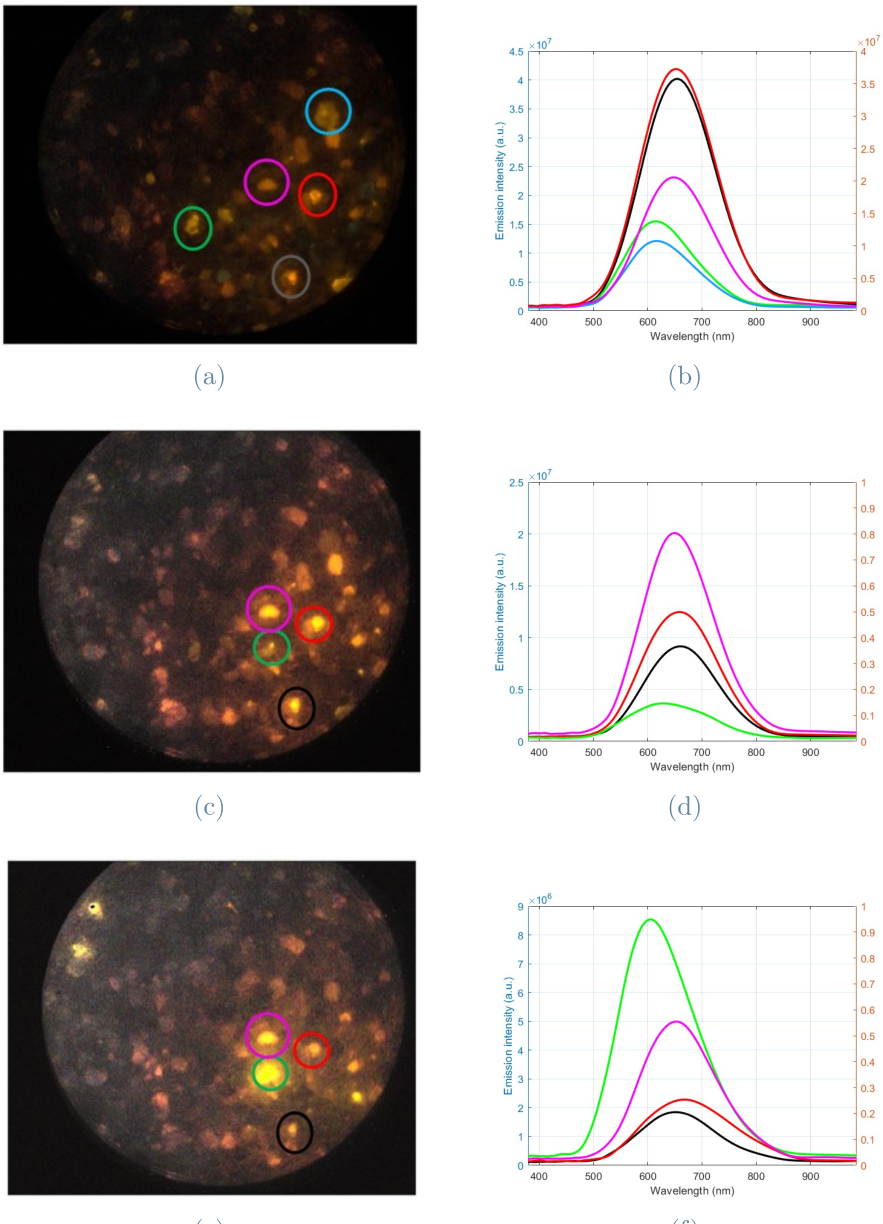

(a) (b)

(c) (d)

(e) (f)

Figure 5.32: (LEFT) Maps of the ROI of UB7 colorized according to the measured spectra. The circled particles are the ones whose spectrum is being shown in the corresponding colors in the plots on the right. (RIGHT) Spectra of the circled particles in the corresponding color. a,b) Map and spectra of the nanoseconds emission (gate: 100 ns; delay after excitation: 0 ns). c,d) Map and spectra of the microseconds emission (gate: 1 µs; delay after excitation: 0.15 µs). e,f) Map and spectra of the tens of microseconds emission (gate: 10 µs; delay after excitation: 1 µs).

UB7: FLIM, nanoseconds emission.

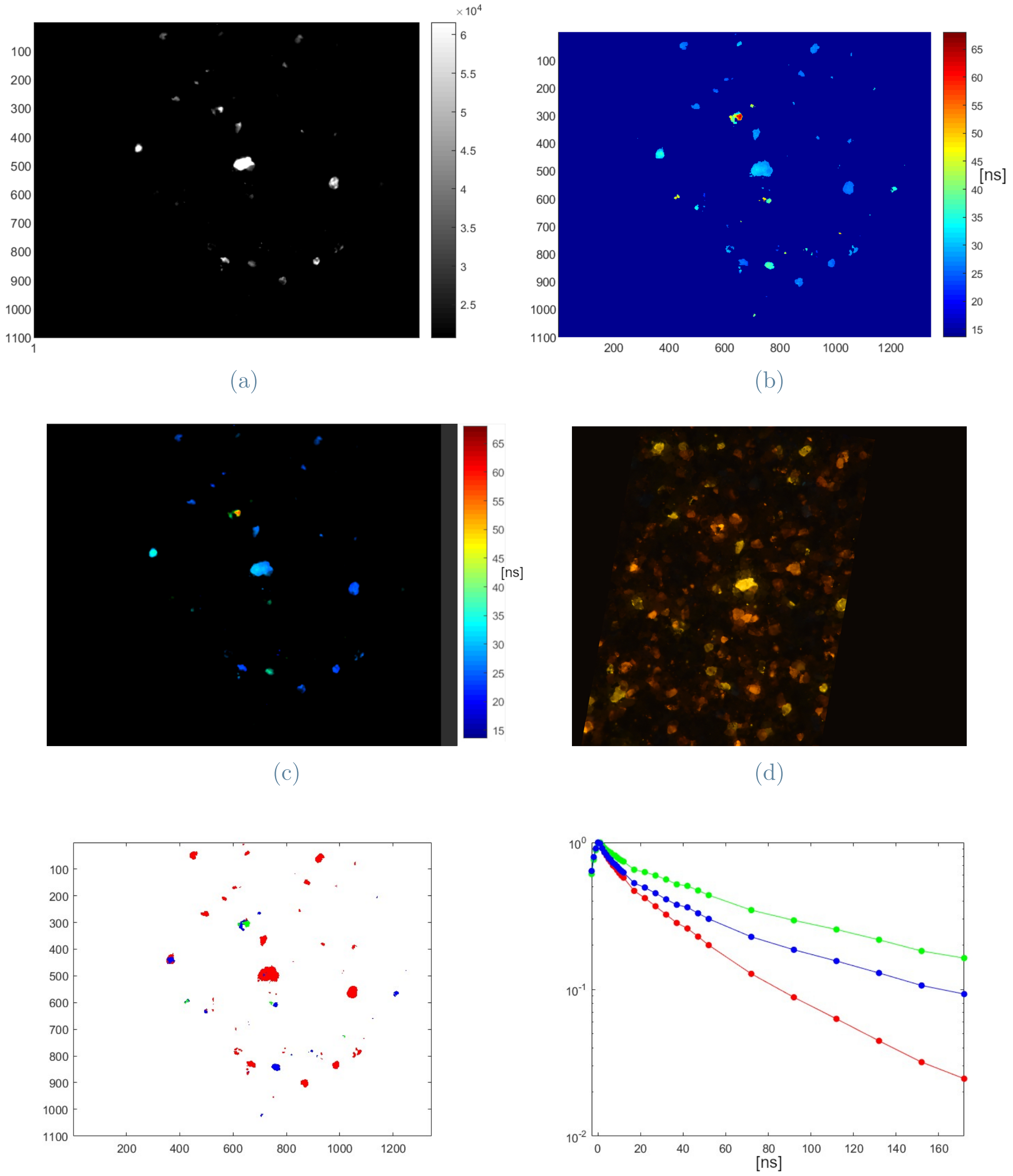

(a)

(b)

(c)

(d)

(e)

(f)

Figure 5.33: FLIM measurement of UB7 at nanosecond timescale (gate: 10 ns; delay range after excitation: 0-100 ns). a) Intensity map of the ROI. b) Lifetime map of the ROI. c) HSV map of the ROI. The different colors of the pixels represent different lifetimes. d) Color picture of the ROI of the sample taken with a microscope at 15X zoom, illuminated with UV light. e) Clusters identified. f) Decay kinetics of the clusters.

UB7: FLIM, microseconds emission.

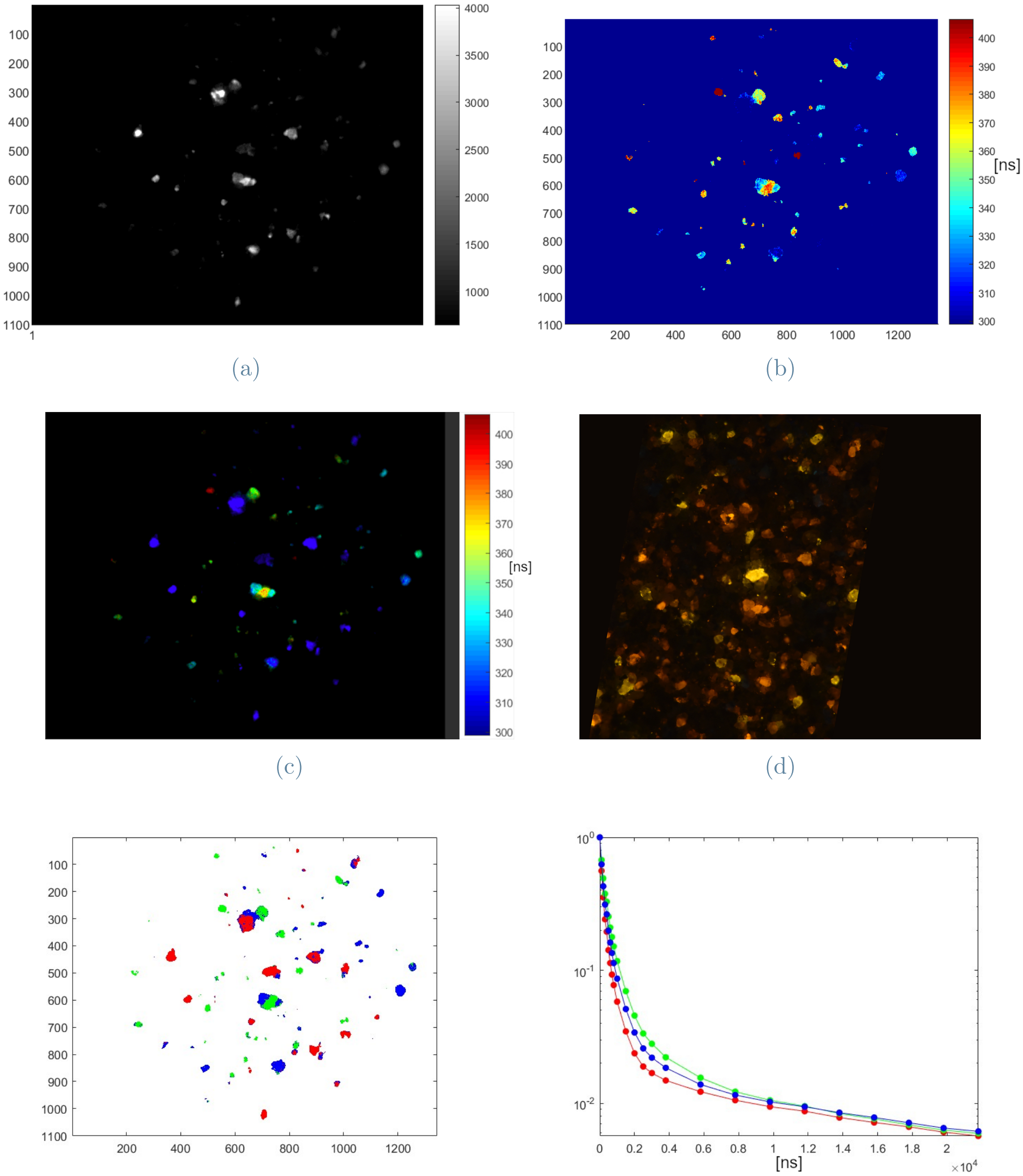

(a) (b)

(c) (d)

(e) (f)

Figure 5.34: FLIM measurement of UB7 at microseconds timescale (gate: 1 µs; delay range after excitation: 0.15-20 µs). a) Intensity map of the ROI. b) Lifetime map of the ROI. c) HSV map of the ROI. The different colors of the pixels represent different lifetimes. d) Color picture of the ROI of the sample taken with a microscope at 15X zoom, illuminated with UV light. e) Clusters identified. f) Decay kinetics of the clusters.

In UB7 the nanosecond, microsecond and tens of microseconds pictures of the ROI all look similar to each other. In fact, this sample seems to be comprised of mostly yellow-orange fluorescent particles which present a lifetime in the microseconds to tens of microseconds range. No trace of blue emitting particles during the nanosecond measure can be found, at least in the field of view. All the analyzed particles show spectra peaking between 600 nm and 660 nm. The tens of microsecond measure reveals that the particle circled in green in figures 5.32c and 5.32e (which is not visible in the nanosecond measure (figure 5.32a) due to it having too faint an emission with respect to the other emitters), whose spectrum peaks at 600 nm, is characterized by the longest lifetime. Id est, when the time gate is extended to 10 µs and at a 1 µs delay after excitation, it is emitting the strongest signal for longer.

The intensity map at the nanosecond scale mainly shows yellow particles, which means that at this timescale they are considerably more intense than their orange counterparts. The opposite is true at the microseconds timescale. This suggests that the yellow fluorescent particles and the orange fluorescent particles may be of different nature.

6 | Discussion

Optical microscopy with UV light illumination has allowed us to understand that ultramarine blue is indeed fluorescent and that it is not the blue lazurite particles, but rather the colorless impurities that fluoresce.

The TRPL measurements allowed us to identify two main emission bands in all ultramarine samples: the "blue-band", between 430 and 460 nm and the one with the shortest lifetime, and the yellow-orange band, or "y/o-band", between 550 and 650 nm and characterized by longer lifetimes. In samples UB3 through UB8, which are of greater quality than UB1 and UB2, we also identified a further band, the infrared band, or "IR-band", between 720 and 800 nm and with even longer lifetime than the y/o-band. The blue band is the strongest immediately after the excitation pulse, but rapidly vanishes, uncovering the y/o-band, which lasts for tens of microseconds. In the samples where it was detected, the IR-band outlasts the y/o-band with a duration in the hundreds of microseconds. It seems that the longer the wavelength of the emission, the longer it duration. Furthermore, we observed that the greater the quality of the pigment, the weaker the blue band, which implies that the impurities that high quality pigments lack should show a blue fluorescent spectrum. On the other hand, among the mineral phases that are present in high quality pigments and have

TG-HSI measurements have shown that how the emission of certain particles changes with the temporal scale. in the samples where they were detected (which are UB1, UB2 and UB6), in the nanoseconds emission the blue fluorescent particles are the strongest emitters. In these samples also a low intensity blue tone pervades the whole field of view, which is probably due to out of focus blue emitting species. It is clear how the blue fluorescent particles have a much lower lifetime than the yellow-orange ones, since no trace of blue emission persists in the microsecond, nor in the tens of microseconds timescales. Most of the yellow-orange emitting particles present a lifetime in the microseconds range, since they appear the brightest in the microsecond measure (with gate of 1 µs and delay of 0.155 µs after excitation), but much dimmer, if they don't disappear completely, in the tens of microseconds measure (with gate of 10 µs and delay of 1 µs after excitation), though UB7 presents a notable exception to this observation, showing particles with extremely long fluorescent lifetimes.

The FLIM technique is designed to distinguish emitters with notably different lifetimes. In the cases of the samples shown, FLIM measurements managed to separate the more intense, short-lived, blue-emitting particles from the less intense, longer-lived, yellow and orange emitting particles, confirming the results of the previously made TRPL measurements. In particular:

- in UB2, the most impure of the selected samples, we found the greatest density of blue emitters;
- in UB5, the purest of the natural ultramarines, we found basically no trace of blue emitters and the yellow-orange emitters were intense even at the nanosecond timescale;
- in UB7, the Chilean pigment, we didn't find any blue emitters, but we found that yellow emitters emitted more intensely in the nanosecond range, whereas orange emitters did so at the microseconds timescale. This noticeable difference in lifetimes may suggest that yellow and orange emitters belong to different chemical species.

7 | Conclusions and Future Developments

Thanks to the application of time-resolved photoluminescence based techniques we have managed to characterize the fluorescent emission of different variants of ultramarine blue pigments. We have found that the source of the fluorescence of this pigment is not to be attributed to the blue lazurite particles, which are responsible for its color, but instead to some of the naturally occurring impurities in lapis lazuli, which appear as colorless particles when observed with a microscope. This has immediately allowed us to achieve one of the objectives of this work: distinguishing between natural pigments, which fluoresce, and artificial pigments, which do not. We have characterized multiple kinds of fluorescent impurities depending on their emission spectra and lifetimes. In particular we have found:

- blue-fluorescent impurities, which feature an emission band in the 430-460 nm spectral range and which present the lowest lifetime in the order of few nanoseconds;
- the yellow-orange impurities, which emit in the 550-650 nm range and have lifetimes in the order of the microseconds. In some cases we have managed to separate the yellow-fluorescent impurities from the orange-fluorescent impurities thanks to differences in lifetimes;
- infrared-fluorescent impurities (only in higher quality samples), which emit in the 720-800 nm range and are characterized by the longest lifetime, in the order of tens of microseconds.

We have also observed that the higher the quality of the pigment, the stronger the yellow-orange and IR component of fluorescence.

We have not managed to link specific fluorescent features to the geographical origin of the lapis lazuli from which the pigment is extracted. More samples from Chilean and Siberian sources should be characterized before attempting to answer the provenance question. Judging by the results of this work, it is reasonable to assume that with time resolved PL alone we would be capable of distinguishing between higher quality pigments and lesser quality ones, by the density of blue fluorescent impurities. The next step would be to pair PL techniques with non-invasive molecular analysis methods, like Raman spectroscopy, to identify the fluorescent impurities, which up to now have only been called by the color of their fluorescence spectrum, and see if they can be linked somehow to the provenance of the sample.

Finally, the results of this work indeed show that there is fertile ground for the employment of time resolved PL techniques for the study of ultramarine blue pigments in paintings.

Bibliography

[1] J. R. Lakowicz. *Principles of Fluorescence Spectroscopy.* Springer, 1983.

[2] E. R. de la Rie. Fluorescence of paint and varnish layers (part 1). *Studies in Conservation*, 27(1):1–7, 1982.

[3] E. R. de la Rie. Fluorescence of paint and varnish layers (part 2). *Studies in Conservation*, 27(2):65–69, 1982.

[4] E. R. de la Rie. Fluorescence of paint and varnish layers (part 3). *Studies in Conservation*, 27(3):102–108, 1982.

[5] A. Nevin, G. Spoto, and D. Anglos. Laser spectroscopies for elemental and molecular analysis in art and archaeology. *Applied Physics A*, 106(2):339–361, 2011.

[6] K. Dowling, M. J. Dayel, M. J. Lever, P. M. W. French, J. D. Hares, and A. K. L. Dymoke-Bradshaw. Fluorescence lifetime imaging with picosecond resolution for biomedical applications. *Optics Letters*, 23(10):810, 1998.

[7] M. Ghirardello, G. Valentini, L. Toniolo, R. Alberti, M. Gironda, and D. Comelli. Photoluminescence imaging of modern paintings: there is plenty of information at the microsecond timescale. *Microchemical Journal*, 154:104618, 2020.

[8] J. Plesters. Ultramarine blue, natural and artificial. *Studies in Conservation*, 11(2):62–75, 1966.

[9] M. Favaro, A. Guastoni, F. Marini, S. Bianchin, and A. Gambirasi. Characterization of lapis lazuli and corresponding purified pigments for a provenance study of ultramarine pigments used in works of art. *Analytical and Bioanalytical Chemistry*, 402(6):2195–2208, 2011.

[10] A. R. De Torres, S. Ruiz-Moreno, A. López-Gil, P. Ferrer, and M. C. Chillón. Differentiation with raman spectroscopy among several natural ultramarine blues and the synthetic ultramarine blue used by the catalonian modernist painter ramon casas i carbó. *Journal of Raman Spectroscopy*, 45(11-12):1279–1284, 2014.

[11] C. M. Schmidt, M. S. Walton, and K. Trentelman. Characterization of lapis lazuli pigments using a multitechnique analytical approach: Implications for identification and geological provenancing. *Analytical Chemistry*, 81(20):8513–8518, 2009.

[12] E. Cato, A. Rossi, N. C. Scherrer, and E. S. B. Ferreira. An xps study into sulphur speciation in blue and green ultramarine. *Journal of Cultural Heritage*, 29:30–35, 2018.

[13] N. Gobeltz, A. Demortier, J. P. Lelieur, and C. Duhayon. Correlation between epr, raman and colorimetric characteristics of the blue ultramarine pigments. *Journal of the Chemical Society, Faraday Transactions*, 94(5):677–681, 1998.

[14] E. R. de la Rie, A. Michelin, M. Ngako, E. Del Federico, and C. Del Grosso. Photocatalytic degradation of binding media of ultramarine blue containing paint layers: A new perspective on the phenomenon of "ultramarine disease" in paintings. *Polymer Degradation and Stability*, 144:43–52, 2017.

[15] J. Chaptal. Notice sur quelques couleurs trouvées à pompeïa. *Mémoires de la Classe des Sciences Mathématiques et Physiques de l'Institut de France Année 1808*, pages 229–235, 1809.

[16] H. Davy. Some experiments and observations on the colours used in painting by the ancients. *Philosophical Transactions of the Royal Society of London*, (105):97–124, 1815.

[17] F. Brunello. *Marco Polo e le merci dell'Oriente*. Neri Pozza, 1996.

[18] C. Cennini and F. Frezzato. *Il libro dell'arte, a cura d Fabio Frezzato*. Neri Pozza, 2009.

[19] F. Delamare. *Bleus en poudres. De l'art à l'Industrie, 5000 ans d'innovations*. Presses de l'École des mines de Paris, 2007.

[20] R. G. Woodbridge. Ultramarine - an inorganic preparation. *Journal of Chemical Education*, 1949.

[21] H. Wang, S. Zhang, S. Hu, Z. Zhen, M. A. Gomez, and S. Yao. A systematic study of the synthesis conditions of blue and green ultramarine pigments via the reclamation of the industrial zeolite wastes and agricultural rice husks. *Environmental Science and Pollution Research*, 27(10):10910–10924, 2020.

[22] J. V. Lelieur, C. L. Duhayon, N. S. Hautecoeur, A. M. Demortier, B. J. Lede, P. J.

Coopman, and P. Leghie. Ultramarine pigment synthesis process. *Patent number US 7632347 B2*, 2009.

[23] D. Reinen and G. Lindner. The nature of the chalcogen colour centres in ultramarine-type solids. *Chemical Society Reviews*, 28(2):75–84, 1999.

[24] A. Re, D. Angelici, A. Lo Giudice, E. Maupas, L. Giuntini, S. Calusi, N. Gelli, M. Massi, A. Borghi, L. M. Gallo, G. Pratesi, and P. A. Mandò. New markers to identify the provenance of lapis lazuli: trace elements in pyrite by means of micro-pixe. *Applied Physics A*, 111(1):69–74, 2013.

[25] I. Osticioli, N.F.C. Mendes, A. Nevin, Francisco P.S.C. Gil, M. Becucci, and E. Castellucci. Analysis of natural and artificial ultramarine blue pigments using laser induced breakdown and pulsed raman spectroscopy, statistical analysis and light microscopy. *Spectrochimica Acta Part A: Molecular and Biomolecular Spectroscopy*, 73(3):525–531, 2009.

[26] A. Lo Giudice, D. Angelici, A. Re, G. Gariani, A. Borghi, S. Calusi, L. Giuntini, M. Massi, L. Castelli, F. Taccetti, T. Calligaro, C. Pacheco, Q. Lemasson, L. Pichon, B. Moignard, G. Pratesi, and M. C. Guidotti. Protocol for lapis lazuli provenance determination: evidence for an afghan origin of the stones used for ancient carved artefacts kept at the egyptian museum of florence (italy). *Archaeological and Anthropological Sciences*, 9(4):637–651, 2016.

[27] A. Romani, C. Clementi, C. Miliani, and G. Favaro. Fluorescence spectroscopy: A powerful technique for the noninvasive characterization of artwork. *Accounts of Chemical Research*, 43(6):837–846, 2010.

[28] K. A. Dooley, A. Chieli, A. Romani, S. Legrand, C. Miliani, K. Janssens, and J. K. Delaney. Molecular fluorescence imaging spectroscopy for mapping low concentrations of red lake pigments: Van gogh's painting "the orchard". *Angewandte Chemie International Edition*, 59(15):6046–6053, 2020.

[29] A. Romani, C. Clementi, C. Miliani, B. G. Brunetti, A. Sgamellotti, and G. Favaro. Portable equipment for luminescence lifetime measurements on surfaces. *Applied Spectroscopy*, 62(12):1395–1399, 2008.

[30] D. Comelli, C. D'Andrea, G. Valentini, R. Cubeddu, C. Colombo, and L. Toniolo. Fluorescence lifetime imaging and spectroscopy as tools for nondestructive analysis of works of art. *Applied Optics*, 43(10):2175, 2004.

[31] L. Wei, W. Yan, and D. Ho. Recent advances in fluorescence lifetime analyti-

cal microsystems: Contact optics and CMOS time-resolved electronics. *Sensors*, 17(12):2800, 2017.

[32] C. Cucci, J. K. Delaney, and M. Picollo. Reflectance hyperspectral imaging for investigation of works of art: Old master paintings and illuminated manuscripts. *Accounts of Chemical Research*, 49(10):2070–2079, 2016.

[33] P. Ricciardi, J. K. Delaney, L. Glinsman, M. Thoury, M. Facini, and E. R. de la Rie. Use of visible and infrared reflectance and luminescence imaging spectroscopy to study illuminated manuscripts: pigment identification and visualization of underdrawings. In Luca Pezzati and Renzo Salimbeni, editors, *SPIE Proceedings*. SPIE, 2009.

[34] C. Manzoni, D. Brida, and G. Cerullo. Phase-locked delay device including an optical wedge pair. *Patent number US 9182284 B2*, 2015.

[35] D. Brida, C. Manzoni, and G. Cerullo. Phase-locked pulse pair for two-dimensional spectroscopy by a birefringent delay line. In *CLEO: 2013*. OSA, 2013.

[36] A. Perri, B. E. Nogueira de Faria, D. C. Teles Ferreira, D. Comelli, G. Valentini, F. Preda, D. Polli, A. M. de Paula, G. Cerullo, and C. Manzoni. Hyperspectral imaging with a TWINS birefringent interferometer. *Optics Express*, 27(11):15956, 2019.

[37] A. Candeo, B. E. Nogueira de Faria, M. Erreni, G. Valentini, A. Bassi, A. M. de Paula, G. Cerullo, and C. Manzoni. A hyperspectral microscope based on an ultrastable common-path interferometer. *APL Photonics*, 4(12), 2019.

[38] M. Ghirardello, C. Manzoni, M. Gironda, R. Alberti, R. Lenz, J. Zöldföldi, S. Behrendt, B. Paz, G. Valentini, and D. Comelli. A novel photoluminescence hyperspectral camera for the study of artworks. *The European Physical Journal Plus*, 136(10), 2021.

[39] R. Nöller, I. Feldmann, Z. Kasztovszky, Z. Szőkefalvi-Nagy, and I. Kovács. Characteristic features of lapis lazuli from different provenances, revised by μXRF, ESEM, PGAA and PIXE. *Journal of Geological Resource and Engineering*, 7(2), 2019.

List of Figures

1.1 Difference between the excited singlet and excited triplet states. 1
1.2 Example of Jablonski diagram. 2
1.3 Jablonski diagram of radiative and non-radiative relaxation processes. . . . 3
1.4 Examples of defects in the structure of a semiconductor. 5
1.5 Portrait of Casper Barlaeus under normal and ultraviolet light. 7
1.6 Example of time gated imaging. 8

2.1 Lapis lazuli stone with pyrite inclusion in calcite matrix. 9
2.2 Sodalite cage. 10
2.3 Wall paintings in the cave temples of Bamiyan. 11
2.4 Cappella degli Scrovegni, vault. 12
2.5 The last judgement, Michelangelo 13
2.6 Deposition, Rogier van der Weyden. 13
2.7 Different qualities of artificial ultramarine blue pigment. 16
2.8 Other ultramarine colors 16

3.1 All samples in powder form. 22
3.2 All samples observed under a microscope at 10X zoom illuminated with visible light. 22

4.1 Area of UB4 with blue fluorescent particle amidst orange fluorescent particles. 26
4.2 Area of UB8 with orange and yellow fluorescent particles facing each other. 26
4.3 Example of TRPL measurement of UB3. 28
4.4 Illustration of preprocessing steps for the extraction of a spectrum from raw data points. 29
4.5 Fitting of the multi-exponential model to experimental data. 30
4.6 Representation of gate scanning method for the observation of the decay curve. 32
4.7 Example of FLIM measurement of UB5. 33
4.8 Example of clusterization of UB5. 34
4.9 TG-HSI setup. 36

4.10 Example of TG-HSI measurement of UB6. 37

5.1 All samples observed under a microscope at 10X zoom illuminated with visible light. 39
5.2 All samples observed under a microscope at 10X zoom illuminated with UV light. 40
5.3 Superimposed pictures of all samples observed under a microscope at 10X zoom. 41
5.4 TRPL datasets of the nanoseconds emission. 43
5.5 TRPL dataset of the nanoseconds emission normalized at t=0 ns. 44
5.6 Gated spectra of all samples in the time interval 0-2 ns. 45
5.7 Gated spectra of all samples in the time interval 30-50 ns. 45
5.8 Emission decays of the blue-band in all samples. 46
5.9 Emission decays of the y/o-band in all samples. 46
5.10 TRPL dataset of the microseconds emission. 48
5.11 TRPL dataset of the microseconds emission normalized at t=0 µs. 49
5.12 Gated spectra of all samples in the time interval 0-2 µs. 50
5.13 Gated spectra of all samples in the time interval 30-50 µs. 50
5.14 Emission decays of the y/o-band in all samples. 51
5.15 Emission decays of the IR-band in all samples. 51
5.16 Relative intensity of the blue-band with respect to the y/o band. 52
5.17 TRPL dataset of the tens of microseconds emission. 53
5.18 TRPL dataset of the tens of microseconds emission normalized at t=0 µs. . 54
5.19 Gated spectra of all samples in the time interval 30-50 µs (tens of microseconds emission). 55
5.20 Gated spectra of all samples in the time interval 110-140 µs (tens of microseconds emission). 55
5.21 Emission decays of the IR-band in the tens of microseconds timescale. . . . 56
5.22 Relative intensity of the y/o-band with respect to the IR-band. 56
5.23 TG-HSI measurements of the nanoseconds emission. 58
5.24 TG-HSI measurements of the microseconds emission. 59
5.25 TG-HSI measurements of the tens of microseconds emission. 60
5.26 TG-HSI measurement of UB2. 61
5.27 FLIM measurement of UB2 at nanosecond timescale. 62
5.28 FLIM measurement of UB2 at microseconds timescale. 63
5.29 TG-HSI measurement of UB5. 65
5.30 FLIM measurement of UB5 at nanosecond timescale. 66

5.31 FLIM measurement of UB5 at microseconds timescale. 67
5.32 TG-HSI measurement of UB7. 69
5.33 FLIM measurement of UB7 at nanosecond timescale. 70
5.34 FLIM measurement of UB7 at microseconds timescale. 71

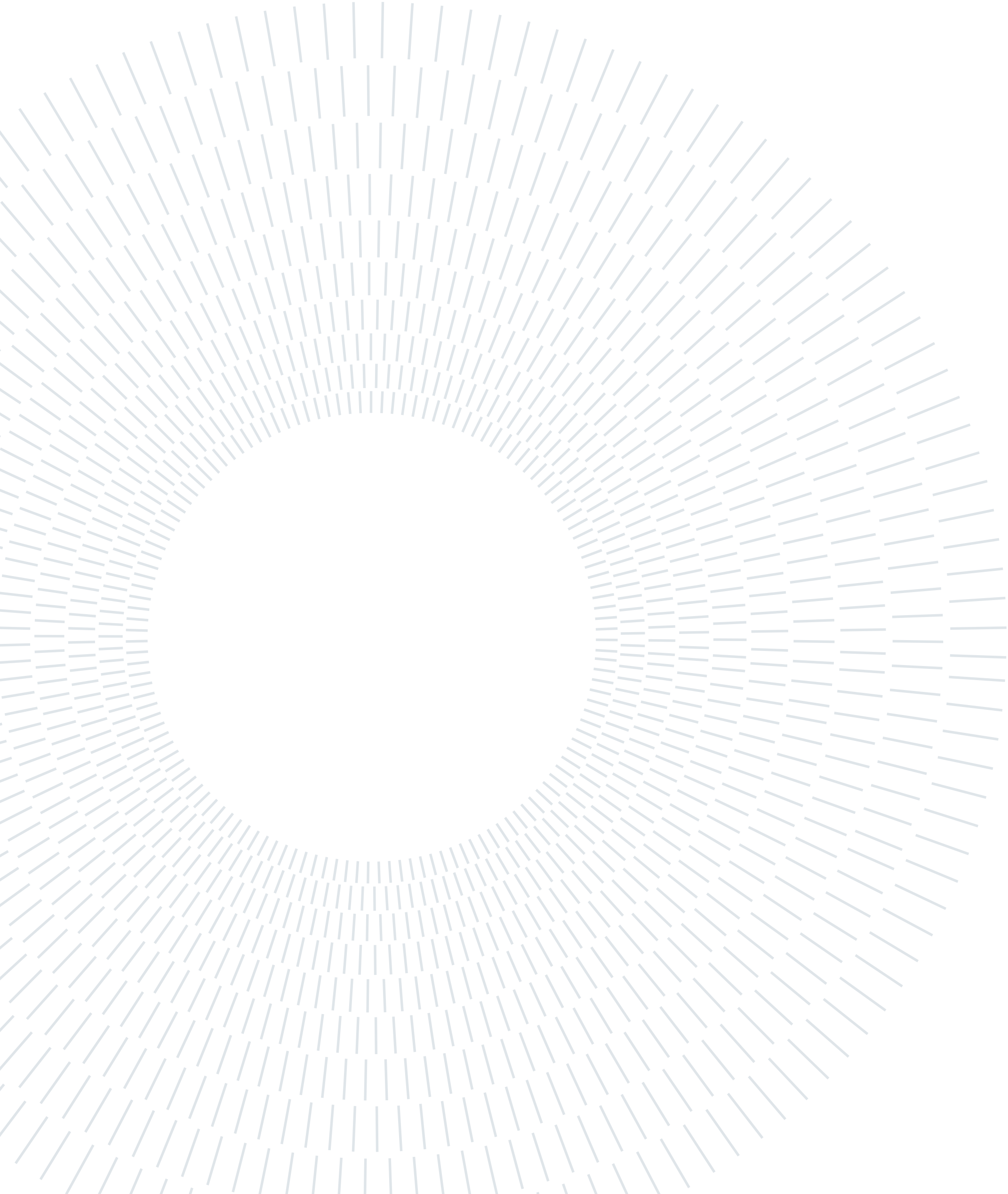

List of Tables

3.1 Table of all the studied samples. 21

4.1 Parameters used for the three different decay kinetics. 27
4.2 Table with calculated parameters of the multi-exponential model. 30
4.3 Parameters for the FLIM measurements of the different decay kinetics. . . 32
4.4 Parameters for the TG-HSI measurements of the three decay kinetics. . . . 36

5.1 Nanoseconds emission effective lifetime calculated for each band of all samples. 47
5.2 Microseconds emission effective lifetime calculated for each band of all samples. 52
5.3 Tens of microseconds emission effective lifetime calculated for the IR-band. 56

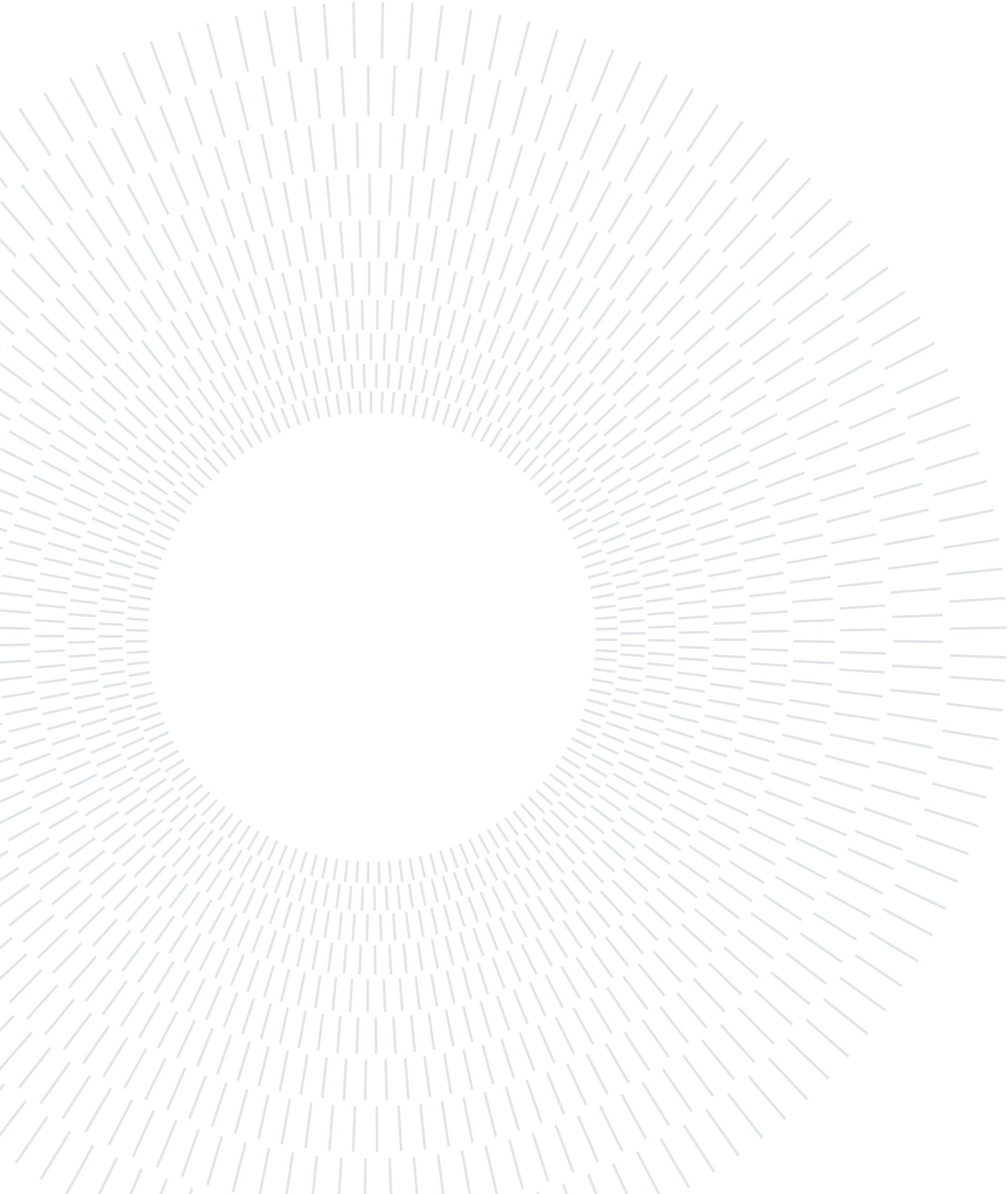

Acknowledgements

I would like to express my heartfelt gratitude to my advisor, prof. Daniela Comelli. Under her invaluable guidance I have learned so much in so little time and working with her has been a true pleasure and privilege.

I also want to thank my co-advisor, dr. Alessia Di Benedetto, for her unlimited patience and kindness in teaching, guiding, correcting and helping me during my stay at Artis.

I would also like to thank my family and friends for their love and support during my years at PoliMi. I couldn't have achieved this goal without you. Also, thank you, Jolie, for keeping me company during the entire writing of this thesis.

Thank you to Riccardo d. C., for the invaluable conversations about art conservation and for providing me some of the books I consulted for for this thesis.

Thank you to Flavia P., for the support during difficult times and for always being there, ready to listen to me and offer encouraging words.

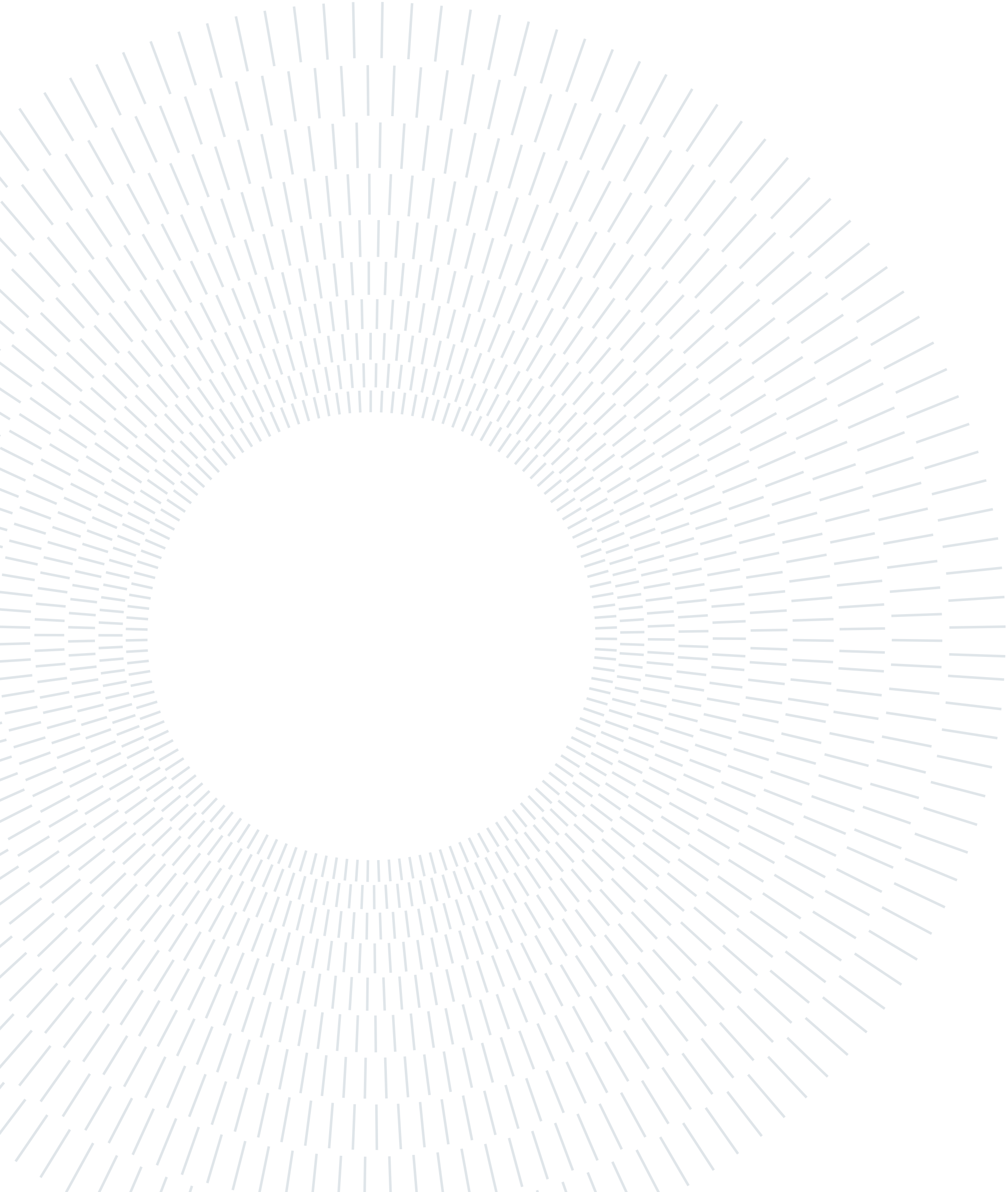Finally, thank you Paola. You have been my greatest ally and have given me the strength to persevere through the most challenging moments. I am profoundly grateful and feel unbelievably lucky for your presence in my life and throughout this journey.